ADVANCED MATERIALS AND FABRICATION METHODS FOR FLAME RETARDANT APPLICATIONS

ADVANCED MATERIALS AND FABRICATION METHODS FOR FLAME RETARDANT APPLICATIONS

By

PATRICK WOJTAL, B.ENG

A Thesis

Submitted to the School of Graduate Studies

in Partial Fulfilment of the Requirements

for the Degree of:

Master of Science

McMaster University

MASTERS OF SCIENCE (2016) McMaster University
(Materials Science and Engineering) Hamilton, Ontario

TITLE: Advanced Materials and Fabrication Methods for Flame Retardant Applications

AUTHOR: Patrick Wojtal, B.ENG. (McMaster University)

SUPERVISOR: Professor I. Zhitomirsky

NUMBER OF PAGES: xiv, 117

LAY ABSTRACT

Technology is expanding, as is our understanding of the environmental and health impacts of chemicals. New flame retardant materials (FRM) must be developed to help protect against fire hazards in increasingly complex products, but care must be taken to avoid implementing dangerous chemicals. This work identifies new FRM which can be efficient replacements for widely used, but toxic FRM. FRM can be applied as a coating cheaply, quickly, and evenly onto substrates of even a complex shape. Techniques and additive chemicals are suggested to create advanced FRM coatings

ABSTRACT

Investigation of flame retardant materials (FRM) identified materials as effective substitutes for halogenated FRM. Many promising materials were tested such as hydrotalcite-type Al–Mg–Zr complex hydroxide, huntite, aluminum hydroxide, hydrotalcite**,** magnesium carbonate hydroxide pentahydrate, magnesium sulfate heptahydrate, magnesium phosphate hydrate, magnesium chloride hexahydrate, sodium metasilicate pentahydrate**,** XZO 2022 (Mg_3Al) and halloysite. Electrophoretic deposition (EPD) manufacturing technique has been developed for the fabrication of coatings containing the most promising FRM candidates. Identifying charging and dispersion agents, such as poly(4-vinylpyridine-co-butyl methacrylate), humic acid, 2,2′-biquinoline-4,4′-dicarboxylic acid, quaternized hydroxyethylcellulose ethoxylate, 3-phosphonopropionic acid, 16-phosphonohexadecanoic acid*,* octadecylphosphonic acid, celestine blue, chitosan, to facilitate EPD was of great importance for successful deposition of composite FRM films. The films were investigated using scanning electron microscopy, transmission electron microscopy, X-ray diffraction analysis, thermogravimetric and differential thermal analysis, as well as Fourier Transform Infrared and Ultraviolet-Visible spectroscopy.

ACKNOWLEDGEMENTS

First and foremost I would like to extend my sincerest gratitude to my supervisor Dr. I. Zhitomirsky for the strong support provided to this research. Your patience, guidance, tremendous knowledge and motivation were monumental in the completion of this work and my development as a student, researcher, and engineer.

I would like to thank also thank Ritch Matthews and Advanced Ceramics for their financial and intellectual support for this work.

Thank you to all my lab mates for your moral and experimental support.

Finally I would like to thank the following individuals for their help in acquiring results for this work.

Chris Butcher, McMaster University

Victoria Jarvis, McMaster University

Frank Gibbs, McMaster University

Steve Kornic, McMaster University

Patrick Wojtal

McMaster University

April 2016

TABLE OF CONTENTS

TABLE OF FIGURES

CHAPTER 1 INTRODUCTION

North American private and public sectors have a strong desire for efficient and non-toxic flame retardant materials (FRM). FRM are used in a wide range of products:

-Furnishing products such as: upholstery, curtains, blinds, carpets, foam and filling materials.

-Electrical devices: televisions, laptops, monitors, keyboards, speakers, vacuum cleaners, cell phones, batteries, household appliances such as panini press' and toasters, circuit boards, chargers, sockets, power strips, washing and drying machines, and refrigerators.

-Building and construction materials such as: electrical wires and cables, composite panels, decorative fixtures, roof components, paints and coatings, insulations, as well as structural and decorative wood products.

-Components of airplanes, automobiles, and trains such as: overhead compartments, dashboards, armrests, headrest and seat coverings/fillings, instrument panels, bumpers, as well as sidewall and ceiling panels. FRM are added to a variety of consumer goods such as clothing, baby products (depends on manufacturer), toy, costumes and wigs(Camino & Costa, 1988; Chen & Wang, 2010; Green, 1996; Horrocks, Kandola, Davies, Zhang, & Padbury, 2005; Lu & Hamerton, 2002; Morgan & Worku, 2015; Porter, Metcalfe, & Thomas, 2000; Weil, 2011; Wojtal, Luo, Chen, & Zhitomirsky, 2015; Zhang, 2009).

Over the years concern about the types of chemicals which are used as FRM and incorporated into products has grown. Of specific concern are brominated and chlorinated

FRM. Polychlorinated biphenyls (PCBs) were a widely used FRM additive but were discovered to be toxic and banned in 1977 in the United States. In response industries turned to brominated FRM which were discovered to be toxic as well. Between 2004 and 2008 the European Union began banning poly brominated diphenyl ethers (PBDEs). In 2009 the U.S. National Oceanic and Atmospheric Administration published a report which revealed that PBDEs are being deposited into our ecosystems at an alarming rate. In 2010 more than 200 scientists from 30 countries brought more attention to the dangers of PBDEs by signing the San Antonio Statement to increase awareness of the dangers in widespread use of these compounds in the world. Although PBDE usage has been greatly reduced in Canada and the United states, unfortunately as other nations' economies and infrastructures develop, the use of these chemicals increases heavily as it is an abundant and effective FRM (Darnerud, 2003; Morgan & Worku, 2015).

Addition of these FRM can sometimes have a deadly effect, where there is an increase in carbon monoxide, toxic gas, and soot which will kill someone before the fire will. This occurs in almost 90% of fire related deaths. These chemicals release dioxin and furan when burned and they have been detected in human milk food and dust. PBDE have been linked to birth defects, cancer, allergies, and respiratory problems. They have an adverse effect on the environment as the chemical is exposed to marine life, plants, and begins accumulating within the ecosystems (Darnerud, 2003; Troitzsch, 1997). Development of new FRM which do not make use of these toxic additives, but are still effective at fighting flames, is a task that is important because it will reduce the impact on the health of humans, plant, animals, and ecosystems.

CHAPTER 2 LITERATURE REVIEW

2.1 FLAME RETARDANT MATERIALS

The use of FRM dates back to before 1 AD where acetic acid and hydrated potassium aluminum sulphate were incorporated into wood to fire retard structures. Although, it was Gay-Lussac's use of chemical salts to fire proof stage curtains in 19th century Paris (Levan, 1984) which marked the beginning of the expansion of FRM technology and its applications. According to the National Fire Protection Association (NFPA), fire damage accounts for $11.6 billion dollars of property loss, 3275 deaths, and 15775 fire injuries in the United States in 2014. In comparison to 2013, there was an increase of 0.7% in the cost of fire damage, 4.7% increase in amount of fires and, 1.1% increase in deaths. Residential buildings account for 85.3% of fire related civilian deaths, 84.4% of all fire damage ($9.8 billion) per year, and there is a structure fire every 64 seconds. Highway vehicles come in at a distant second, responsible for 9.5% ($1.1 billion) in property damage and 9.5% of civilian deaths per year (DiGangi, 2012; Haynes, 2015). A country's fire losses will increase rapidly as its economy and infrastructure begins to develop. Fire losses eventually stabilize and begin to decrease as efforts are made by the developing nation to introduce FRM and other fire safety measures. As new policies or technologies are introduced this trend may be disrupted because new fire hazards are introduced or FRM are banned(The Geneva Association Staff, 2014).

2.1.1 Fire Science

To protect against fire loss, fire protection engineers employ a variety of engineering techniques. Fires can be extinguished (passively or actively), controlled, suppressed, or prevented altogether by intelligent storage or construction. The use of sprinklers, extinguishers, or flame retardants can be used to help prevent these fire losses. It is important to note that it is not always the goal to completely prevent a fire, especially if the risk is low. This would be impossible or too uneconomical to implement. The primary goal is to allow extra time for individuals to move to safety; secondary goal is to protect from fire loss, or slow the flame spread until help arrives. Traditional fire protection techniques are not always useful. For example a sprinkler system will not be effective in situations such as: a) electrical fires because as conductive water accumulates it will be creating an additional electrocution hazards b) areas containing valuable products which are water sensitive, or c) areas where installation of a sprinkler system would be difficult. Techniques such as flooding with inert gases are not a safe option for areas holding people who may asphyxiate. Isolation of fuel sources from potential points of ignition is not always a dependable strategy. Sparks or embers may be introduced by being carried by the wind or an individual. Using FRM either in place of, or along with, the above strategies will help reach the fire protection goals of the particular project (Morgan & Worku, 2015).

The Fire triangle (Figure 1) is a very important concept to aid one in understanding how a fire starts and is able to maintain itself. To complete the triangle the

host must have exposure to heat that will make the fuel burn, an oxidizer to sustain the chemical reaction, and a fuel source that will feed the burn. Fire protection technologies are able to prevent or slow fires by removing one or more points of the fire triangle(DiNenno, 2008).

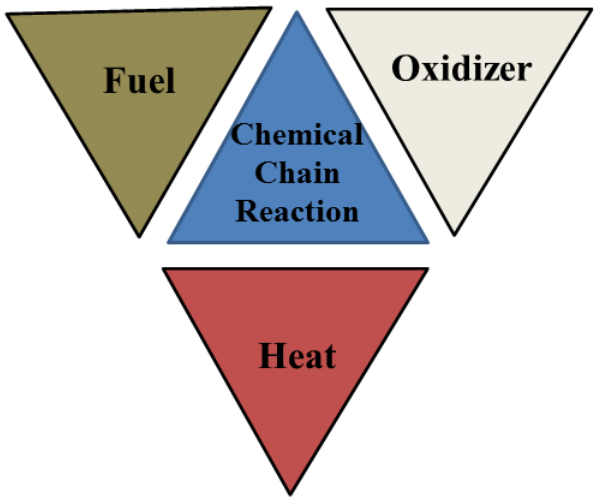

Figure 1: Fire triangle

A fire proceeds through four stages (Figure 2). Ignition is the first step where in the three components of the triangle (fuel, oxygen, and heat) combine and experience a sustained chemical reaction. Basic methods of fire control can be effective here, such as a fire extinguisher or an FRM. Next step is marked by heat being provided from the flame of the initiation fire. More heat is available to ignite more fuel and is termed the Growth step. In an enclosed area the temperature of the room will increase exponentially as more

surfaces, not in contact with the fire, reach their ignition temperatures. An event called the flashover represents the transition into the final step, a fully developed fire. The flashover occurs in a room where multiple surfaces have reached their ignition temperature and catch fire simultaneously. The final step is burnout (decay), where the majority of the fuel is used up and fires begin to dissipate (Morgan & Worku, 2015).

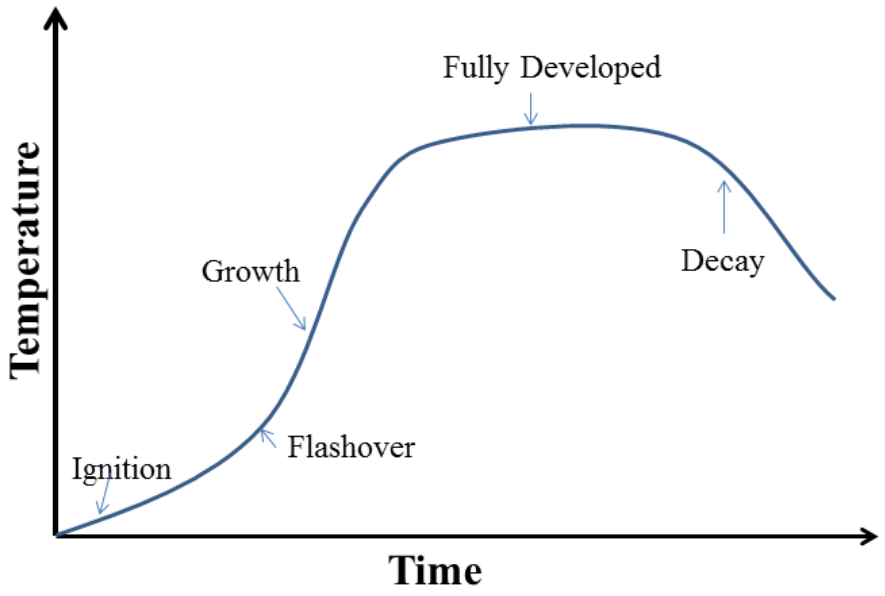

Figure 2: Four stages of a fire

The movement of heat and flames occurs through conduction, convection, and radiation. Conduction is the transfer of heat through direct contact. Convection is the movement of heat through the atmosphere, hot gas moves towards cold; hot gases are less dense, therefore will rise. Radiation is the transfer of heat through electromagnetic waves;

the heat is transferred upon colliding or absorbing onto an object. The primary methods of disrupting a fire is to reduce the temperature of the material, isolate the fire from the fuel or oxygen, dilute the fuel, or break the chemical reaction (Morgan & Worku, 2015).

2.1.2 Flame Retardants Theory

The FRM's primary goal is to slow down the spread of a flame or increase the ignition temperature. Under specific conditions some FRM are able to even completely snuff out a small active flame. FRM can be found in all kinds of states, be it solid, gas, or liquid, their goal remains the same. These materials or chemicals are added into a host product that is flammable or needs an improvement to its fire retardancy. The FRM can be bonded chemically to the host or used as a standalone additive in a heterogeneous mixture. A flame retardant can be organic or inorganic; it can be attributed to a molecule type, the structure, or polymer. An effective FRM functions by reacting with its surroundings, or decomposing, as its temperature increases. Once the FRM is triggered, it will function by one or more of the following mechanisms (Morgan & Worku, 2015).

Inhibition of the vapor-phase combustion chemical reaction occurs by the FRM breaking down and releasing active free radical species that react with the free radicals within the flame. This has the effect of suppressing further chemical reactions as opposed to spreading it further. This occurs due to fire chemical reactions being attributed to one-electron free radical reactions, impeding the free radical prevents it from interacting with subsequent molecules and effectively breaking the chain. FRM released free radicals are

known to form species that are less exothermic, therefore reducing the heat available in the vapor phase (Morgan & Worku, 2015). A major detractor from this FRM form is that due to an incomplete combustion there are is an excess of dangerous reaction products released such as carbon monoxide and smoke. This becomes a visibility, toxicity and asphyxiation problem when FRM is applied in enclosed areas or places with poor air circulation. The molecules that are attributed with the property of inhibiting the vapor phase combustion are mainly halogens and phosphorous (Weil & Levchik, 2009; Wilkie & Morgan, 2010).

FRM can also form a stable and protective char by reacting with the fuel source. This is termed a condensed phase char formation. The FRM is activated before pyrolysis of the fuel occurs. The fuel is able to react with the FRM, creating stronger bonds that are more thermally stable. This slows the pyrolysis or increases the temperature required to undergo pyrolysis. This protective char can take on properties such as improved insulating behavior by having a lower thermal transfer coefficient. Another benefit of this thermally stable char is it acts as an impermeable barrier that restricts the exposure of the fuel to the oxidizer. FRM that work via the char formation protection method include molecules containing phosphorus and nitrogen. Intumescent systems and polymer nanocomposites are effective thermal barrier creators as well (Morgan & Worku, 2015).

FRM can also endothermically decompose upon heating. This creates a cooling effect on the surroundings, reducing the heat available to be applied to the fuel. Less heat being absorbed by the fuel means that the pyrolysis temperature is not being hit. The

additional benefit is that FRM which endothermically decompose, such as metal hydroxides/carbonates, release a respectable amount of carbon dioxide and/or water. This has the effect of diluting the fuel and concentration of oxidizer in the flame front. The oxide left behind after decomposition has already achieved its highest oxidation state, and therefore it is not flammable (Morgan & Worku, 2015).

2.1.3 Flame Retardant Material Types

There are seven major classes of flame retardants which utilize the fire retarding mechanisms of chapter 2.2.2. These include halogen, phosphorus, mineral, nitrogen, intumescent, inorganic (nonmineral), and nanocomposite based FRM.

Halogenated FRM contain atoms of I, Br, Cl, and F and are used primarily to protect polymers. These are produced in structures that are polymeric, aromatic, or aliphatic (Morgan & Wilkie, 2014; Wilkie & Morgan, 2010). Organochlorine and organoiodine are passed over in FRM applications due to the difficulty of forming stable bonds within a host. Organofluorine has a strong carbon fluorine bond requiring high temperatures to allow the fluorine to break off. This is not desirable because the FRM must be able to react before the fuel ignites or flashover occurs. Organofluoride FRM will usually be used separately from the bulk material. They come in the forms of PVDF (poly-vinylidene difluoride), PTFE (poly(tetrafluorethelyne)), and ETFE (poly(ethylene-co-tetrafluoroethylene)). Organobromide additives are one of the most popular for halogenated FRM(Morgan & Worku, 2015).

Bromine is favored above the other halogens because it's easier to synthesize, has the potential to have more active bromine atoms per polymer chain, and has a favorable carbon bromine bond which activates in an ideal temperature range of 200-300^{o}C. Examples of common bromine FRM can be observed in Figure 3.

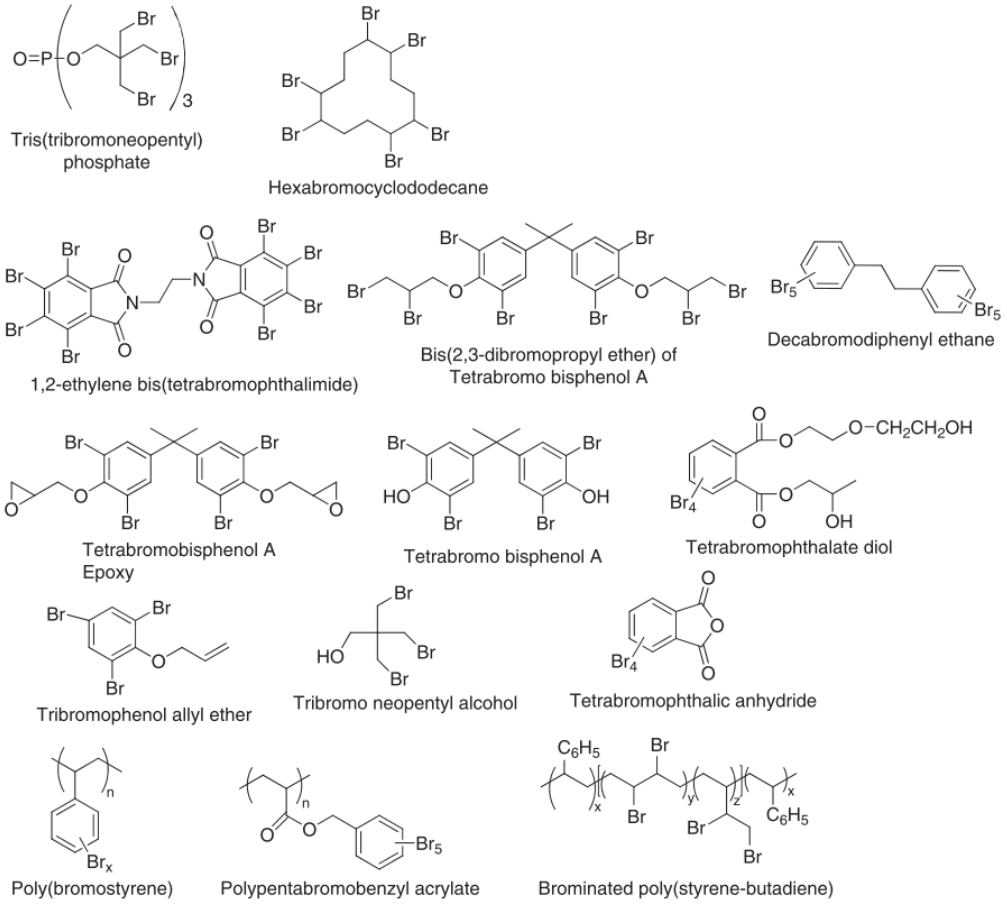

Figure 3: Examples of brominated FRM(Morgan & Worku, 2015)

FRM which are brominated have proven benefits when combined with synergists such antimony oxides, boron, or phosphorous containing compounds (Morgan & Wilkie, 2014; Morgan & Worku, 2015; Wilkie & Morgan, 2010). If synergists are introduced then lower levels of flame retardant can be used and the host will still receive the same,

or better, fire protection. A lower amount of flame retardant material is also beneficial because it reduces the impact that this material will have on the properties of the host material it is being added to. Bromine FRM have been around since 1930 but there is a large concern over the hazards of its use. Having a vapor phase inhibiting reaction, there is a great deal of smoke and carbon monoxide release. Another big concern is the leaching out of the FRM from the bulk materials. These hazardous organic pollutants are widely used and pose a threat to the health of people and the environment. The search for a replacement is ongoing, The Dow Chemical Company has found some success in replacing hexabromocyclododecane (expanded polystyrene foams) with a variety of products such as Green Crest™, Emerald Innovation™, etc. (Morgan & Worku, 2015).

Phosphorus containing FRM (Figure 4) is more versatile than halogens. It can be incorporated into structures which are organic, but inorganic as well. Phosphorus atoms in FRM tend to have an inter-aromatic ring presence; they are able to be used simultaneously with other FRM such as halogens or nitrogen, which tend to combine onto carbons of aromatic rings.

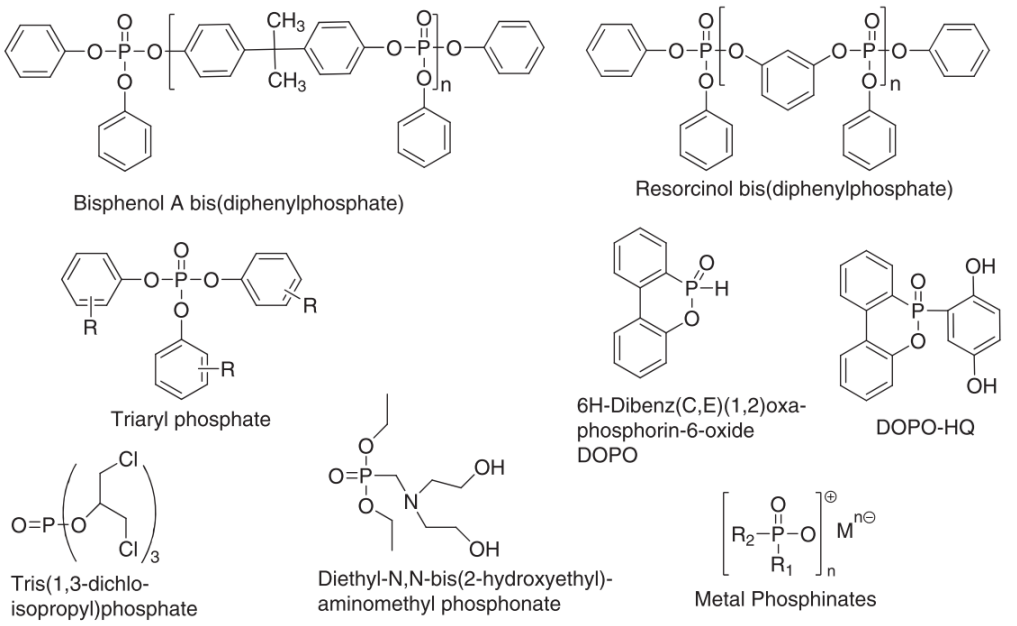

Figure 4: Examples of phosphorus containing FRM(Morgan & Worku, 2015)

Sustaining its versatile trait, phosphorus containing flame retardants are able to display multiple fire protection mechanisms. Depending on the structure, chemistry, and the method of incorporation into host, phosphorus flame retardants can take advantage of both vapor phase combustion inhibition and/or create a protective char(Wu et al., 2014). Fire protecting using phosphorus started being used commercially around 1950 but suffered from similar drawbacks as its halogen counterpart. When heated the FRM would release harmful gasses, such as carbon monoxide, that would not be safe to apply in closed areas like airplanes. As the concern of the dangers of halogens was brought to light, industries turned to this new flame retardant as the next best alternative. Studies have revealed that phosphorus based FRM are also prone to have hazardous effects on people and the environment(Salamova, Hermanson, & Hites, 2014). Steps have been

taken by FRX Polymers to produce safer phosphorus FRM. NOFIA is an FRM based on polyphosphates and polyphosphate-*co*-polycarbonates and successfully passed regulations partly due to its high molecular weight and stability(Morgan & Worku, 2015).

Nitrogen FRM tends to bond to either carbon or hydrogen atoms. Some examples of nitrogen based flame retardants are shown in Figure 5. Great care must be taken in developing nitrogen based FRM because only a small hand of formulations will have the desired effect. Many nitrogen containing molecules will act as an oxidizer instead. Use of nitrogen based FRM is not very common, majority of usage comes in conjunction with other types of FRM.

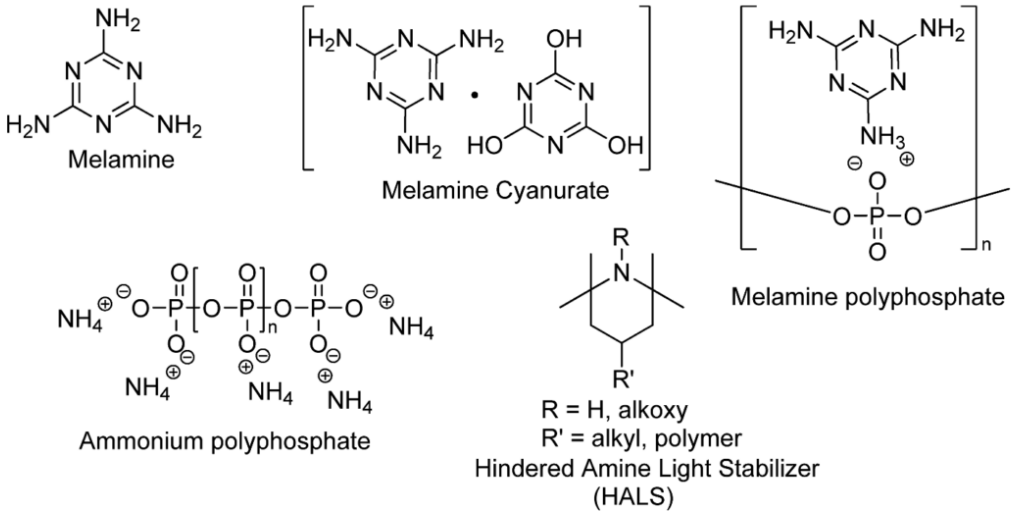

Figure 5: Examples of nitrogen containing FRM(Morgan & Worku, 2015)

One example of this FRM is melamine cyanurate, which protects polyamides through a unique fire protection mechanism. Melamine allows its host to depolymerize at a high rate when exposed to increasing temperatures. This decreases the viscosity of the host as its molecular weight plummets, and the polymer is able to drip away before it undergoes pyrolysis and becoms used as fuel for the fire. This technique is useful when there is a localized fire near a melamine-containing material raised away from the ground. As the material is heated it will begin to drip and fall away from the heat source before its pyrolysis temperature is reached (Morgan & Wilkie, 2014). This technique is only effective if the melamine containing material drips to an area that is not exposed to heat as well. Nitrogen based FRM have started gaining attention with the growing concern of the ever popular halogens. Nitrogen FRM can be safer for the environment with the correct chemistry and applications but still require a great deal of research to expand the pool of candidates and their applications.

Intumescent flame retardants refer to a FRM that is capable of growing a protective shield over its host upon exposure to heat. This char acts as a physical barrier preventing the oxidizer from mixing with the fuel, even if the polymer pyrolyzes. It is also able to act as a thermal barrier, vastly reducing the heat transfer coefficient on the surface of the material. Char formation requires three primary ingredients; source of carbon, source of acid, and a foaming agent. Visual aid is provided in Figure 6. The acid and carbon react together to form the char with physical barrier properties. The foaming agent then inflates this char outward imparting the thermal barrier quality. A big

challenge of creating effective intumescent FRM is being able to formulate the chemistry well enough that the foaming agent releases after the char is formed.

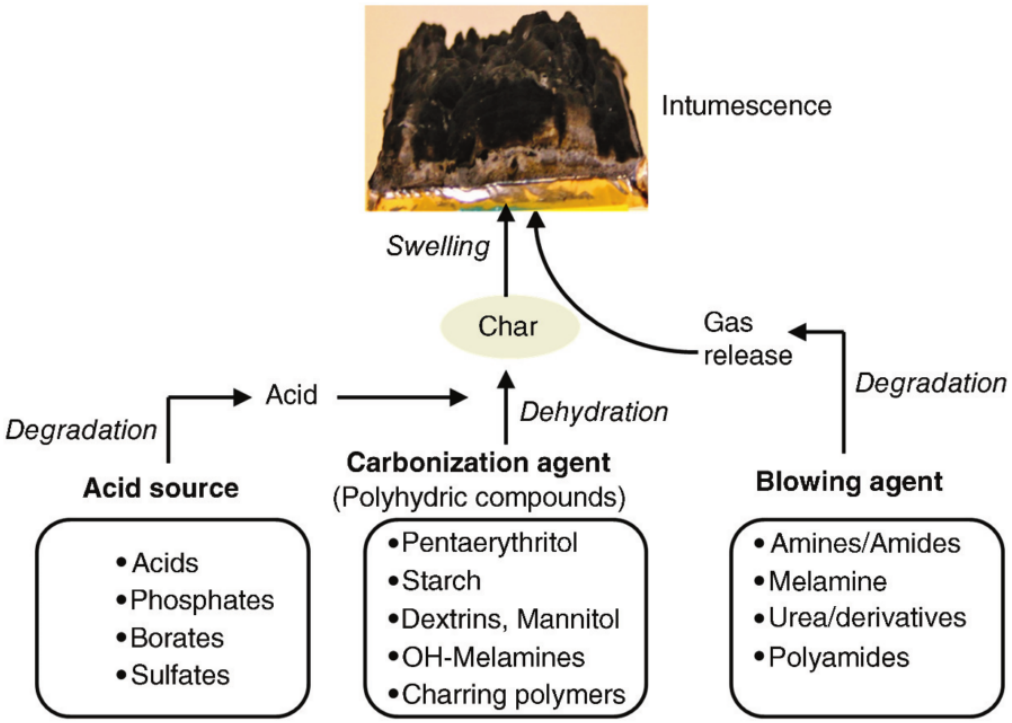

Figure 6: Requirements for a char formation (Morgan & Worku, 2015)

Intumescent FRM can be reacted into the bulk of the host like the previous FRM candidates, but an added benefit of this class of FRM is that it may be applied as a coating without the risk of altering the properties of the material it protects. The drawback of intumescent FRM is that their thermal range of activity is low, in the 160-240^{o}C range (Morgan & Wilkie, 2014; Weil & Levchik, 2009; Wilkie & Morgan, 2010). This forces such FRM to be only viable for polymers with lower processing temperatures where it will not activate prematurely.

Non-mineral inorganic FRM refers to compounds that display fire protective properties but do not contain carbon. The category is quite wide and they are used mostly as synergists, but the protective techniques employed by these FRM are both char formations and vapor phase combustion inhibitions. Silicon based FRM develop a silicon oxide protective shield under heat exposure. They are commonly used in wrapping wires and cables as calcium silicon carbonate (Morgan & Wilkie, 2014; Salamova et al., 2014). Stannates found their popularity in the form of tin oxides or hydroxides. They are used primarily to suppress the smoke released by halogen FRM. Zinc borate is an ideal synergist when used sparingly (large loadings increase flammability) with halogen, mineral, and even phosphorus based FRM (Morgan & Wilkie, 2014). Other good synergists are sulfonates and molybdates. They improve smoke suppression and char formations in conjunction with more effective FRM on polymers (Morgan & Worku, 2015).

Nanocomposite FRM refer to polymer chains equipped with nanoscale plates, spheres, or rods. These specialized chains not only improve fire protection properties but also enhance electrical and mechanical properties. Nanocomposites are able to combine with the host and create a network structure when exposed to a fire. This interaction strengthens the bonds in the fuel and prevents decomposition of the polymer host providing less fuel to the fire. This behavior also allows the polymer to stay intact longer and drip less. This property is useful for certain applications where a pool of leaked polymer could add a potential fuel source to other surfaces. A large hindrance to the usage of nanocomposites is the uncertainty of the environmental and biological effects of

nanomaterials. Another hindrance is found in the difficulty of synthesizing these nanocomposites on a commercial scale, at a competitive price. This category of FRM finds its place as a synergist; with small amounts of nanocomposite FRM, there can be a reduction of the total loading of FRM (Morgan & Wilkie, 2007; Morgan & Worku, 2015; Porter et al., 2000).

Mineral FRM consists mainly of metal hydroxides and metal carbonates. These may be mined and extracted from mineral deposits, or synthesized using appropriate reactants. Mineral FRM are relatively cheap but require larger loadings to match the effectiveness of some of the other popular FRM types. Mineral FRM have a dual pronged reaction when heated. There is an endothermic decomposition which absorbs heat from the flame front. The decomposition releases products such as carbon dioxide or water which are nonflammable substances that help dilute the fuel concentration at the flame front. The residue left over after decomposing acts as a heat shield. Mineral FRM are excellent smoke reducers due to this release of gas, they sometimes get incorporated into FRM cocktails for this sole purpose. Mineral FRM are one of the more understood and safe FRM. No harmful gases are released and may be used in closed quarters which contain human occupants. The products left over after decomposition are naturally occurring minerals, therefore stable and environmentally safe. The only concern arises in the inhalation of FRM if particle size is very small (Green, 1996; Morgan & Worku, 2015; Troitzsch, 1997; Wojtal, Luo, et al., 2015).

Common mineral FRM of interest in this study are aluminum hydroxide ($Al(OH)_3$), huntite($Mg_3Ca(CO_3)_4$), and magnesium hydroxide($Mg(OH)_2$). Method of judging the effectiveness of mineral FRM is through the analysis of the DTA/TGA data. DTA measures the magnitude of the exothermic and endothermic reactions occurring in the mineral as temperature is increased. TGA measures the magnitude of mass loss experienced by the mineral with increasing temperature. Mass loss may be attributed to the release of gases such as water or carbon dioxide. Therefore ideal candidates will display large mass losses which will give good smoke suppression and fuel dilutions. Candidates will also display endothermic peaks which will be associated with potential to absorb heat and cripple a pillar of the fire triangle (Morgan & Worku, 2015; Wojtal, Chen, Shi, Mathews, & Zhitomirsky, 2015).

The TGA/DTA data for aluminum hydroxide, $Al(OH)_3$ is provided in

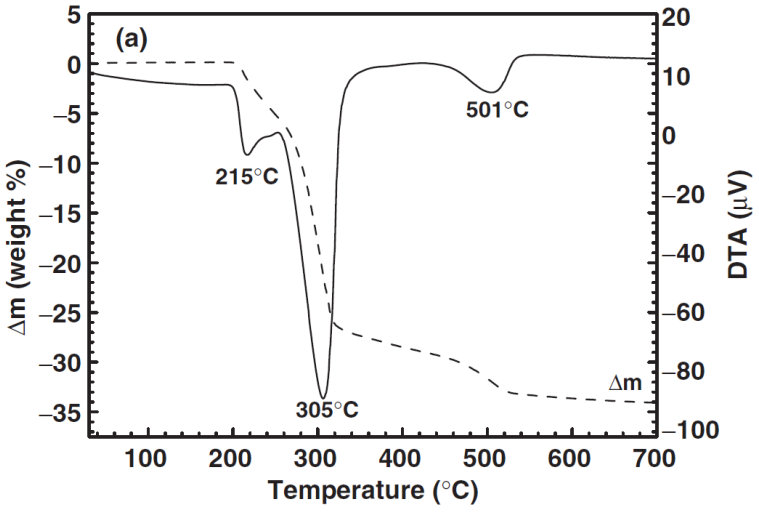

Figure 7. Decomposition of aluminum hydroxide begins at about 200°C and completes at 520°C, with a total mass loss of 34%. The mass loss is attributed to the

release of adsorbed surface water followed by release of stoichiometric OH groups as a result of decomposition of $Al(OH)_3$. The decomposition reaction is given by equation 2-1 (Strekopytov & Exley, 2006).

$$\mathbf{2Al(OH)_3 \rightarrow 2AlO(OH) + 2H_2O \rightarrow Al_2O_3 + 3H_2O,\ \Delta H^o = +139{,}150 \text{ at } 305\,^oC} \quad \text{Eq. 2-1}$$

The intermediate step occurs under a high partial pressure of water which may occur if aluminum hydroxide molecules are captured within a polymer film. When decomposition occurs, a pocket of localized high H_2O concentration will occur, creating a favorable environment for AlO(OH) to form before the final decomposition into Al_2O_3.

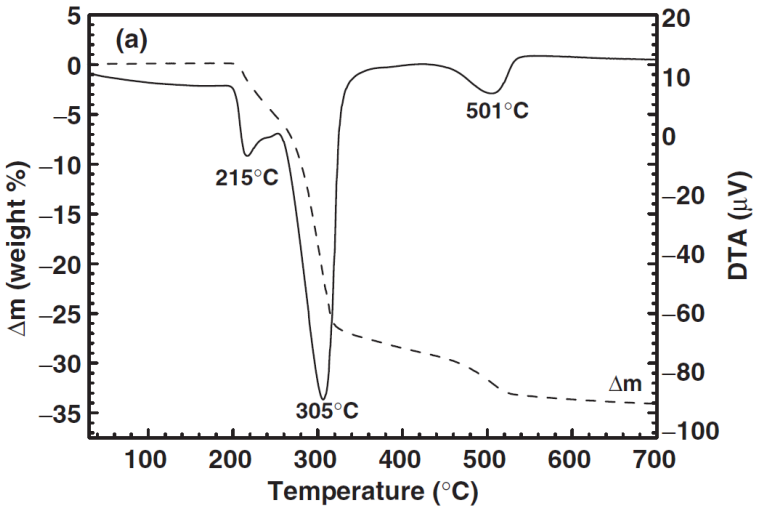

Figure 7: Aluminum hydroxide TGA and DTA curves (Mercury, Pena, De Aza, Sheptyakov, & Turrillas, 2006)

Magnesium hydroxide ($Mg(OH)_2$) behaves in a similar fashion to aluminum hydroxide without the potential of forming an intermediate phase. It decomposes at a higher temperature of 300°C but has a lower total mass loss of only 30% (L A Hollingbery, 2010). Mass loss is attributed to the release of water following equation 2-2(Morgan & Worku, 2015).

$$\mathbf{Mg(OH)_2 \rightarrow MgO + H_2O,\ \Delta H^o = +74{,}250J \text{ at } 430^oC} \qquad \text{Eq.2-2}$$

There is a single large endothermic peak evident at 430°C attributed to the decomposition in equation 2-2. The endothermic reaction releases an increasing amount of water until 445°C, the rate of water release then decreases as the reaction is completed. This material is an effective FRM because it has one endothermic decomposition that can absorb heat from an ignition surface. The resulting release of water can even dilute the fuel. Magnesium hydroxide is less favorable compared to aluminum hydroxide because of its lower total mass loss, but it may be more useful if a higher decomposition temperature than 300°C is required in the host material.

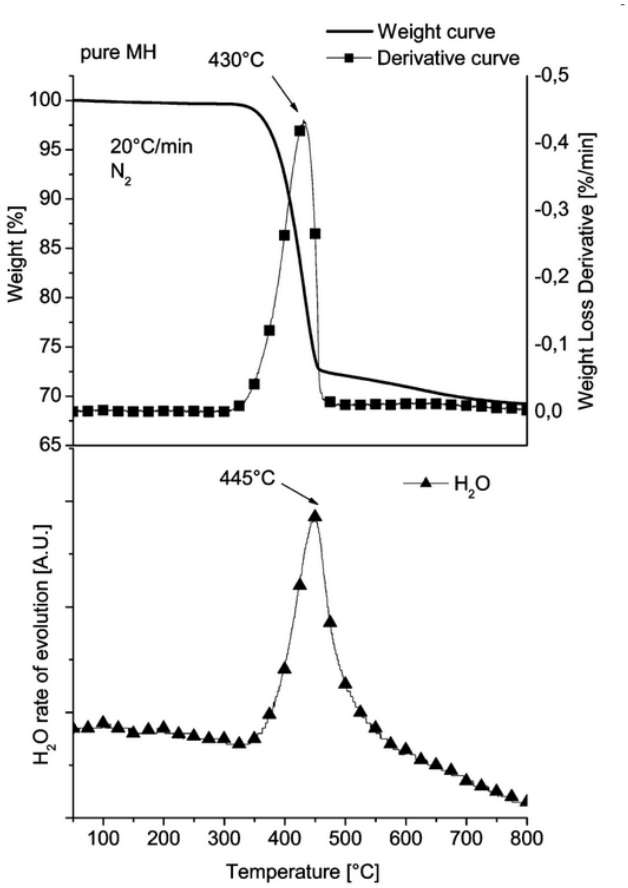

Figure 8:TGA (solid line)/DTA(■) data for $Mg(OH)_2$ top, and rate of water evolution curve(▲) bottom. Total mass loss of 30%(Bras, Bourbigot, Duquesne, Jama, & Wilkie, 2005)

The TGA/DTA data for huntite ($Mg_3Ca(CO_3)_4$) is presented in Figure 9 and it is evident that it decomposes through two major stages. The decomposition is attributed to large release of carbon dioxide and a total mass loss of 50%; stoichiometry of the decomposition reaction is given by equation 2-3 (L A Hollingbery, 2010).

$$\mathbf{Mg_3Ca(CO_3)_4 \rightarrow 3MgO + CaO + 4CO_2} \qquad \text{Eq. 2-3}$$

The first stage of huntite decomposition occurs at 450°C. The decomposition is associated with the endothermic peak at 570°C; products of the reaction are carbon dioxide magnesium oxide and magnesian calcite ($(Ca,Mg)CO_3$). In the second decomposition stage the magnesian calcite decomposes into magnesium oxide and calcium oxide and carbon dioxide. This endothermic reaction is associated with the endotherm at 714°C. Huntite's high decomposition temperature of 450°C makes it a poor choice for applications where immediate reaction to heat must be displayed to protect the host. This high thermal stability is desirable when combined with polymers which have a higher processing temperature; FRM remains effective even after processing. Total mass loss of 50% surpasses the effectiveness of both aluminum hydroxide and magnesium hydroxide. The release of carbon dioxide is capable of diluting the concentration of fuel and oxidizer at the site of the flame. Huntite is a good candidate for implementation in combination with other mineral FRM such as aluminum hydroxide. Aluminum hydroxide is able to decompose and protect at a lower temperature range of 200-450°C. As the heat increases, huntite takes over and protects the host at a higher temperature range of 450-700°C. Huntite has an added benefit of having a plate-like structure. This allows the shielding of a polymer host from releasing some volatile gasses when heated.

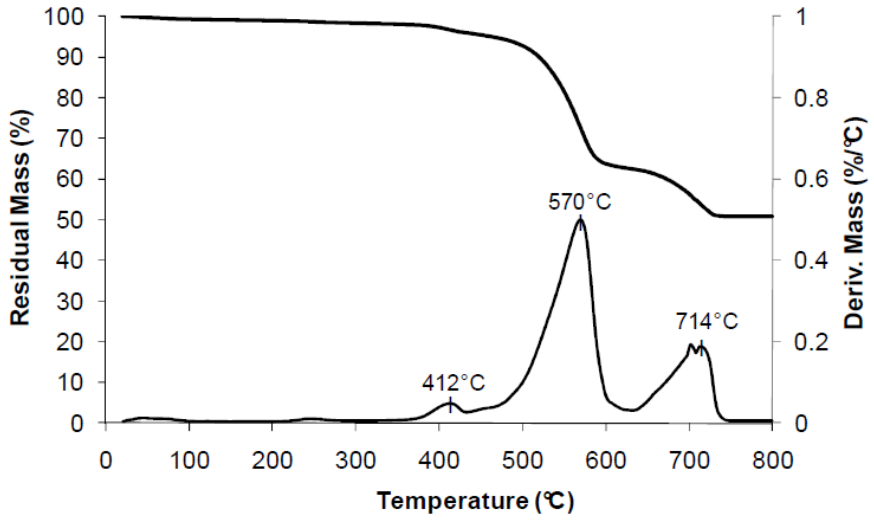

Figure 9: Huntite TGA/DTA data, with a total mass loss of 50% (L A Hollingbery, 2010)

The TGA/DTA data for hydromagnesite ($Mg_5(CO_3)_4(OH)_2 \cdot 4H_2O$) is presented in Figure 10. Decomposition of hydromagnesite starts at a temperature of 250°C. The mineral sheds adsorbed water, an endothermic peak is evident at 282°C for this decomposition. At 400°C decomposition of the hydroxide groups occurs, water is released and an endothermic peak is evident at 463°C. At 518°C the final decomposition step releases carbon dioxide and an endothermic peak is observed at 519°C to represent this reaction. Chemistry of the reaction is shown in equation 5-1 (L A Hollingbery, 2010). The entire decomposition of hydromagnesite results in a total mass loss of 55%. This material has a greater mass loss than both aluminum hydroxide and magnesium hydroxide; there is a large release of both water and carbon dioxide for dilution of fuel at the ignition surface.

$$Mg_4(CO_3)_3(OH)_2 \cdot 3H_2O \rightarrow 4MgO + 3CO_2 + 4H_2O \quad \text{Eq.2-4}$$

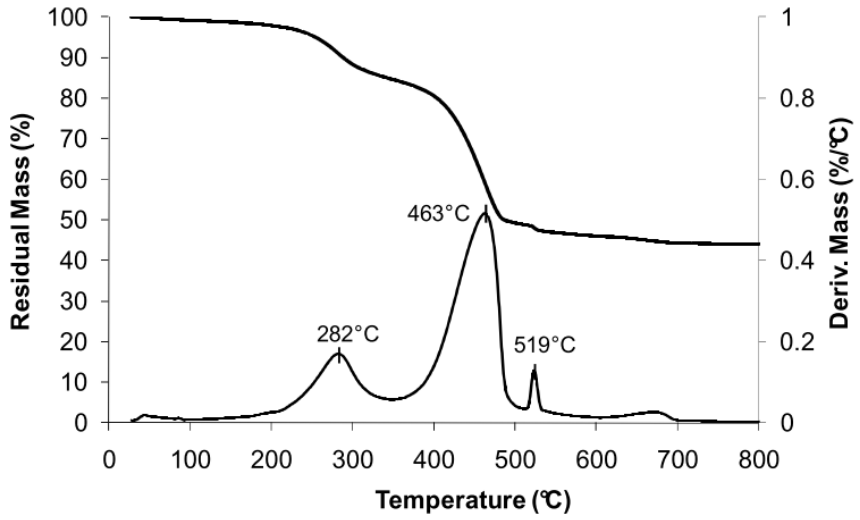

Figure 10: TGA/ DTA data for hydromagnesite, which shows a total mass loss of 55% (L A Hollingbery, 2010)

2.2 Electrophoretic Deposition

The electrophoretic deposition technique (EPD) has recently garnered a great deal of interest in academic research and potential for industrial applications. It's use has been found in creating hydroxyapatite coatings on metal substrates for biomedical

applications(Besra & Liu, 2007), (Sridhar & Mudali, 2003), nanosized zeolite membranes(Besra & Liu, 2007), luminescent materials(Yum, Seo, Lee, & Sung, 2003), glass and ceramic matrix composites(Boccaccini, Kaya, & Chawla, 2001), gas diffusion electrodes and sensors(Felix, Jao, Pasupathi, Linkov, & Pollet, 2014), oxide nanorods carbon nanotube films(Limmer & Cao, 2003), superconductors and layered ceramics(Besra & Liu, 2007), flame retardants(Wojtal, Luo, et al., 2015), etc. EPD is cheap and efficient to set up, allowing effective processing of advanced coatings and materials, in comparison to dip and slurry coating. EPD itself is a highly effective process where the morphology and thickness of the coating can be easily modified through changes in the deposition time or applied potential. There is a lack of restrictions on substrate shape; a uniform coating can be applied to objects of complex geometry. The formation time for a coating is low allowing quick depositions to be achieved easily, this trait is ideal for commercial applications. The tools needed to perform EPD are simple and do not require a large investment of capital. There is no need for binder burn out since green coatings feature insignificant volumes of organic matter. This reduces the pollution and complexity of coating application.

2.2.1 Major Factors Which Affect Electrophoretic Deposition

The characteristics of EPD are determined by physical parameters which include electrodes, deposition time, voltage, and current. Properties of the suspension are also a

major determinant of the behavior and quality of EPD. The process consists of charged particles, which are dispersed using a dispersing agent, in a fluid medium which, under the influence of a DC electric field, deposit onto a conductive medium carrying an opposite charge. There are two distinctive types of EPD; one is when the particles are negatively charged and deposit onto the anode. The other being when particles are positively charged and deposit onto the cathode. These processes are termed anodic and cathodic electrophoretic deposition, respectively. Current is carried by charged particles and free ions within the suspension; therefore the mass of deposited material is not strictly related to applied voltage alone. Hamakers law can be used to relate deposit yield (w), electric field (E), electrophoretic mobility (μ), surface area of electrode (A), and particle mass concentration found in the suspension(C)(Besra & Liu, 2007; Lefèvre & Jolivet, 2009)

$$w = \int_{t_1}^{t_2} \mu \cdot E \cdot A \cdot C \cdot \mathrm{d}t \qquad \text{Eq. 2-5}$$

Avgustinik's law can be applied to cylindrical electrodes where the extra terms are length(l), radius(a), radius of coaxial counter electrode(b), permittivity (ε), zeta potential(ξ), and viscosity of suspension(η)(Besra & Liu, 2007)

$$w = \frac{l \cdot E \cdot \varepsilon \cdot \xi \cdot \mathrm{t}}{3 \ln (a/b) \cdot \eta} \qquad \text{Eq. 2-6}$$

The effect of deposit time on deposition rate is that it will decrease over extended periods of time. This occurs because while the potential is maintained at a constant value, the electric field decreases due to an insulating layer forming onto the electrode. At low time intervals, the relationship between deposition rate and time is linear, as the electric field is still uninhibited(Y. C. Wang, Leu, & Hon, 2004). This behavior is displayed in Figure 11, where at a constant voltage of 100 V the thickness of ZnO increases linearly with time until 250 sec. After this time an insulating layer is formed and the rate of ZnO deposition begins to decrease.

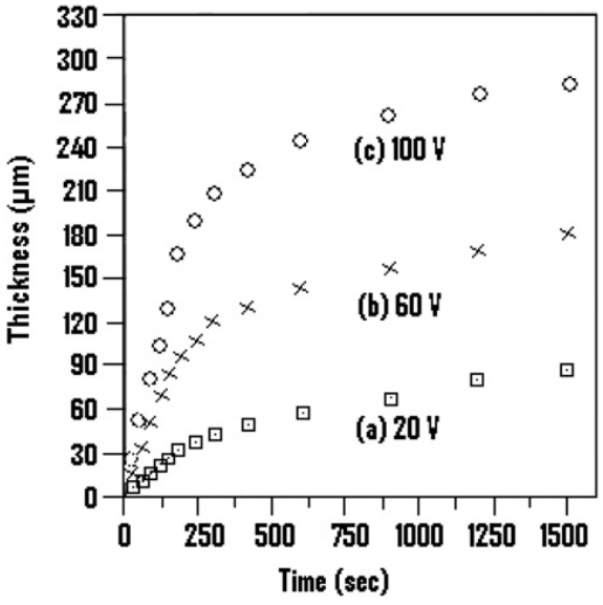

Figure 11: Thickness of ZnO coating deposition on copper electrode versus deposition time at constant voltage (a) 20 V (b) 60 V (c)1 00 V (Besra & Liu, 2007)

The deposition on green film weighs heavily on the conductivity and uniformity of the substrate electrode (Peng & Liu, 2001). Increasing the applied voltage will in turn increase the rate of deposition. The quality of the coating was found to be greater under medium applied fields of 25-100 V/cm (Basu, Randall, & Mayo, 2001). If the field is above 100 V/cm the quality diminishes due to the high rate of deposition, turbulence created in the vicinity of the deposit and packing of particles is disturbed. The high speed of particles may prevent them from finding their closest packed position (Zhitomirsky & Gal-Or, 1997). Figure 12 shows the deposition of hydroxyapatite on Ti_6Al_4V substrate. As the applied voltage is increased, the weight of the deposited material on the substrate increases as well.

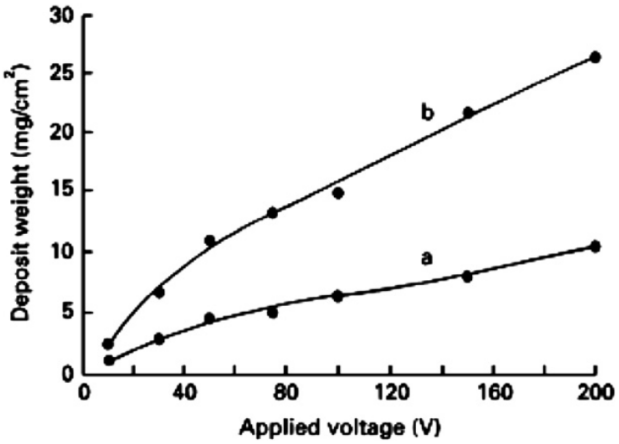

Figure 12: Weight of hydroxyapatite deposited on Ti_6Al_4V substrate versus applied voltage at constant time (a) 30s (b) 120 s (Besra & Liu, 2007)

2.2.2 Suspension for Electrophoretic Deposition

For the development of the EPD method, parameters of the suspension must also be considered. Particle size of the material for EPD is usually in the 1-20 μm range (Corni, Ryan, & Boccaccini, 2008). A small particle size will aid in allowing better dispersion, better deposit adhesion, less cracking upon drying, and particles will remain suspended longer with better mobility. Large particles will have a larger gravitational force imparted upon them, possibly leading to a gradient in thickness on the substrate if sedimentation begins to occur (if substrate is placed vertically). When the dielectric constant of a suspension liquid is low, deposition will be inhibited because of the poor dissociation of molecules in the suspension. A high dielectric constant on the other hand, means that a large ionic concentration is present in the medium. The large ionic concentration reduces the thickness of the double layer region and in turn, the electrophoretic mobility and particle stability. The conductivity of the suspension must be taken into consideration as well. A suspension that is too conductive will show particles with poor particle motion (Ferrari & Moreno, 1996). Conductivity may increase with higher temperature, or with the addition of specific dispersing agents.

Zeta potential is of very high importance in EPD. A large and uniform surface charged is desirable on the suspended particles and the zeta potential influences the stabilization of the suspension. Zeta potential influences the intensity of repulsion between particles, particle velocity, and green density of the deposit. The two mechanisms that play a large role in determining the interactions of particles in the

medium are van der Waals and electrostatic forces. These forces compete with each other, the stronger force determine if particles will coagulate or disperse. If attractive forces are too high and particle charge too low, the film will appear porous due to agglomeration of the particles. Modification of the zeta potential can be performed by introducing polyelectrolytes, acids or bases. The correct pH must be determined for a particle charging agent to produce a large charge on the particle and obtain the correct polarity with the desired deposition rate (Ata, Liu, & Zhitomirsky, 2014; Zhitomirsky, 2002).

The ability to create a stable suspension is of vital importance in EPD. Stable solutions will resist undergoing flocculation; the particles have a low settling time and the EPD coatings show improved adhesion. A suspension that is too stable, the repulsive forces experienced between particles cannot be overcome by the applied electric field, it is difficult to form a film. Particles must be stable in the bulk of suspensions, but able to experience a local instability around the electrodes due to the release of ions by electrolysis. Therefore, sought after properties of an EPD suspension is low viscosity and conductivity, high dielectric constant and zeta potential, and the ability to form a suspension with good stability (Ferrari & Moreno, 1996).

2.2.3 Colloidal Theory

Manipulation of the interparticular forces within the suspension will pave the road to good dispersion and stability for EPD of the desired particles. Within ceramic colloidal

systems the interparticular forces of interest are van der Walls attractive forces, double layer repulsive forces and steric forces (Besra & Liu, 2007). Van der Walls attractive forces must be resisted by counteracting repulsive forces to avoid flocculation and particle settling. An electrical charge can be gained by a particle when it is immersed within an aqueous solution. This occurs through surface group ionization, differential solubility of ions, lattice substitution, charged crystal surface fracturing, and adsorption of ions to the surface (Besra & Liu, 2007). The surface charge provided by the ions then determines the distribution of other ions within the solution. Ions of like charge to the particle surface, co-ions, are repelled while ions of opposite charge, counter ions, will be pulled towards the particle surface and surrounding area. Ions that determine the surface charge of the particle are usually composed of hydrogens or hydroxyl ions. The electrical double layer is arises as a result of this charge distribution next to the surface(Blees, 2002).

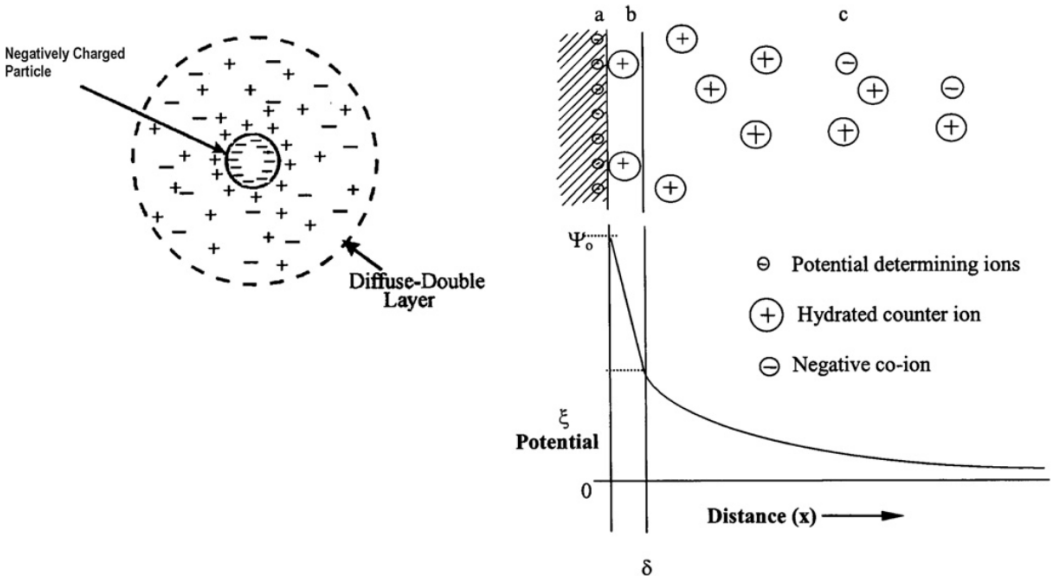

Figure 13: Electrical double layer with (a) surface charge (b) Stern layer, (c) diffuse layers of opposite charge ions (Besra & Liu, 2007)

The stern layer refers to the closest position that hydrated counter ion can hold in relation to the particle surface. In Figure 13 the representation of a lyosphere, stern layer and potential drop can be observed. To gauge the interaction between particles the interaction of the diffuse layers is taken into considerations.

$$\Psi = \Psi_{\delta} \exp(-\mathrm{K}x) \qquad \text{Eq. 2-7}$$

The Poisson-Boltzmann expression in equation 2-7 is used to determine the potential (Ψ) at position x away from the stern layer. The potential between the stern layer and diffuse

layer is represented by (Ψ_δ), as well as the Debye-Huckle parameter(κ) (Besra & Liu, 2007).

2.2.4 DLVO Theory

Understanding the stability and dispersion of the particles in a suspension can be gained by observing Verwey and Overbeek's (Verwey, 1947) DLVO theory. Dispersion can be manipulated by playing with interparticular forces as well as manipulating their interactions. To avoid agglomeration van der Walls forces must be counteracted with stronger electrostatic repulsive forces in the double layer. According to Hiemenz (Hiemenz & Rajagopalan, 1997) the effect of the forces is additive, equation 2-8, where van der Walls force of attraction (V_A) and electrostatic repulsion(V_R), the total energy is then predicted by V_T

$$V_T = V_A + V_R \qquad \text{Eq. 2-8}$$

In Figure 14 (Besra & Liu, 2007; Laskowski JS, 1992)(Stoll & Buffle, 1995), lines A represent particles pairs which have low ionic strength allowing the total energy to remain repulsive. System of line B is able to remain dispersed due to its high potential energy barrier and high primary minimum trough. This potential barrier is very useful as

even if particles would adhere at close distances they must first contain enough energy to overcome this barrier. This is evident in line C, where particles repel unless they have enough energy to overcome the potential energy barrier and in turn agglomerate due to the low primary minimum trough. The primary barrier is influenced by the zeta potential and Debye length. Barriers can also be increased by lowering the temperature (reducing thermal energy). Lines D and E show stronger ionic forces in particles leading to attractive forces among the particles leading to agglomeration.

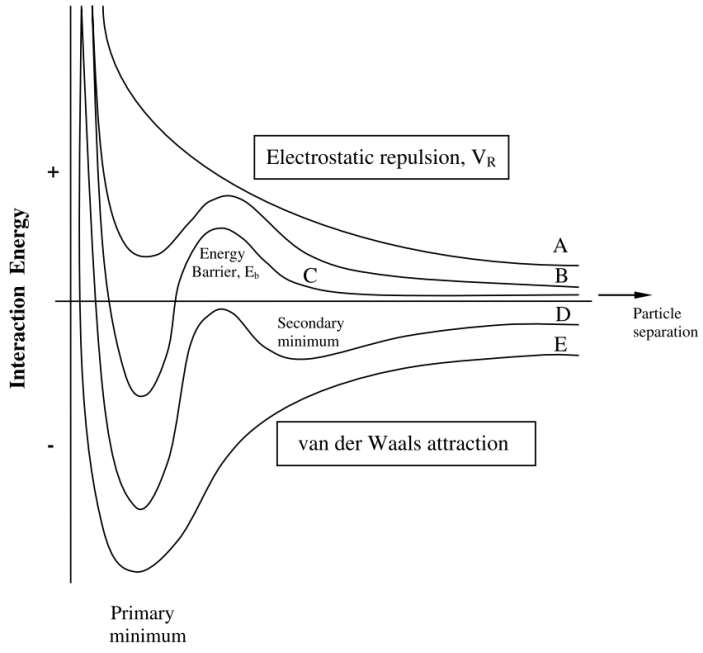

Figure 14: Interaction energy versus separation distance. (A) and (B) show repulsive systems,(C) mixed, D) and (E) which are attractive systems (Besra & Liu, 2007)

2.2.5 Surface Modification

The surface of particles may be modified in a variety of ways to help improve the stability of the suspension, impart a charge on a particle or completely change the charge originally found on the particle. Steric stabilization can be achieved by introducing macromolecules which attach to the particle surface. Hydrophobic tails will then surround the particles allowing them to now repel each other; system will now be behaving like the classical electrostatically stabilized particles(Besra & Liu, 2007). Charged dispersants can be used electrostatically stabilize inorganic colloid particles. Some forms of this phenomenon are the adsorption of ions from solutions of metal salts, iodine acetone reactions which release protons to charge particles, or introducing polyelectrolytes, surfactants, organic acids, and alkalis(Ata, Liu, et al., 2014). Charged dispersants function by way of binding onto the surface of a particle and imparting their charge, among other properties it may contain, onto their host. If a particle has no charge it cannot be used effectively for EPD, therefore charging agents ratify this inconvenience if one would like to deposit a particular particle. In order for charged dispersing agents to adhere strongly to particles, there must be functional groups present that will allow complexation of the ligands. Catechol ligand OH groups are able to form strong attachments to metal ions by deprotonation and adhesion of this group. There are multiple families of molecules with chelating properties which allow strong adsorption onto particle surfaces, namely salicylic acid, gallic acid, and chromotropic acid families(Ata, Liu, et al., 2014).

CHAPTER 3 RESEARCH OBJECTIVES

The purpose of this work was to find candidate materials suitable as replacements for current flame retardant materials. New materials must satisfy the primary objective of being safe for the environment and humans. Studies were then performed to see if candidate performance as a flame retardant material can rival industry standards or offer other potential benefits such as better mechanical properties or regeneration behavior. Advanced dispersant and charging agents where investigated to use with current and candidate flame retardant materials to explore the potential to use electrophoretic deposition to create flame retardant coatings. Coatings were also investigated for their secondary ability to make corrosion resistant barriers on steel. Successful candidates were characterized using electron microscopy, X-ray diffraction, thermogravimetric analysis, Fourier transform infrared spectroscopy, Uv-vis, potentiostat for measuring open circuit potential, quartz crystal microbalance, and transmission electron microscope.

CHAPTER 4 EXPERIMENTAL PROCEDURE

4.1 Experimental Materials

Sigma-Aldrich

- Zinc oxide(ZnO)
- Titanium oxide(TiO_2, anatase)
- Halloysite ($Al_2Si_2O_5(OH)_4 \cdot nH2O$)
- Hydromagnesite($Mg_5(CO_3)_4(OH)_2 \cdot 4H_2O$)
- Ludox colloidal silica(SiO_2)
- Magnesium carbonate hydroxide pentahydrate ($C_4Mg_4O_{12} \cdot H_2MgO_2 \cdot 5H_2O$)
- Magnesium sulfate heptahydrate ($MgSO_4 \cdot 7H_2O$)
- Hydrotalcite ($CH_{16}Al_2Mg_6O_{19} \cdot 4H_2O$)
- Magnesium phosphate hydrate ($Mg_3O_8P_2 \cdot xH_2O$)
- Magnesium chloride hexahydrate ($MgCl_2 \cdot 6H_2O$)
- Yttrium nitrate ($Y(NO_3)_3 \cdot 6H_2O$)
- Sodium metasilicate pentahydrate ($Na_2SiO_3 \cdot 5H_2O$)
- Chitosan (CHIT) (degree of deacetylation of 85%)
- Poly(4-vinylpyridine-co-butyl methacrylate (PVBM) (90% 4-vinylpyridine)
- Celestine blue dye (CBD)
- Aurintricarboxylic acid ammonium salt ($ATNH_4$)
- 3-Phosphonopropionic acid (3PHA)
- 16-Phosphonohexadecanoic acid (16PHA)

• Octadecylphosphonic acid (octaPHA) • Quaternized hydroxyethylcellulose ethoxylate (HCE) • 2, 2'-Biquinoline-4, 4'-Dicarboxylic Acid (BQCOOH) • 3-aluminum sulphate ($Al_2(SO_4)_3$) • Aluminum nitrate ($Al(NO_3)_3$) • Nitric acid (HNO_3) • Acetic acid (CH_3COOH) • Sodium hydroxide (NaOH)
MEL Chemicals
• Aluminum- magnesium- zirconium hydroxide (AMZH) • XZO 2022 (Mg_3Al)
Sibelco
• Huntite ($Mg_3Ca(CO_3)_4$)
Alfa Aesar
• Humic acid (HA)

4.2 Electrophoretic Deposition Methodology

Electrophoretic deposition was performed onto a substrate of 304 grade stainless steel. The substrate was polished and then cleaned with distilled water and ethanol. The size of the substrate and platinum (Pt) counter electrodes was 50 x 25 x 0.1 mm. Substrate and counter electrode were connected to an electrode holder which fits over a

300 ml beaker which allowed for an open air deposition. The holder allowed two platinum (Pt) counter electrodes to be mounted. The counter and substrate were situated 15 mm apart. The electrode holder was then connected to a constant voltage power source. Decision for positive and negative electrodes was made on a case by case basis and addressed within the results section. Electrodes were then submerged into suspensions which were agitated ultrasonically for at least 15 mins before deposition testing. Voltage for depositions ranged from 7-100V.

4.3 Nanobalance Studies

Quartz crystal microbalance (QCM922, Princeton AppliedResearch, USA) method was used for the in-situ investigation of the deposition yield. The mass, Δm, of deposited material was calculated using equation 4-1 (Deakin & Buttry, 1989).

$$-\Delta F = \frac{2{F_0}^2}{A\sqrt{\rho_q \mu_q}} \times \Delta m \qquad \text{Eq. 4-1}$$

ΔF is frequency decrease of the QCM, F_0 is the parent frequency of QCM (9 MHz), A is the area of gold electrode (0.2 cm^2), ρ_q is the density of the quartz and μ_q is the shear modulus of quartz. The EPD cell contained a gold coated quartz substrate and Pt counter electrode. The distance between the electrodes was 15 mm.

4.4 Characterization Testing Methods

Surface morphology of films was studied using a Scanning Electron Microscope (SEM) (JSM-7000F, JOEL, JAPAN). Samples were cut from substrate and attached to sample holder using copper tape. Copper tape had conductive adhesive on both sides for convenience of preparation. Finally, a 2 nm platinum film was applied over samples and dried for 24 hours at room temperature. Deposited material was removed from the stainless steel substrate. Material that was tested from suppliers was analyzed in as received condition. Composition of material was discovered using X-ray diffraction analysis (diffractometer Bruker D8, UK) with Cu-K_α radiation at a scanning rate of 5^o/min. Thermogravimetric (TGA) and differential thermal analysis (DTA) was performed using the thermoanalyzer NETZSCH STA-409, Canada. Testing was carried out on 10 mg of material inside an aluminum oxide crucible exposed to air. A heating rate of 5^oC/min from room temperature to 1000^oC was used. Fourier Transform Infrared (FTIR) Spectroscopy (FTS-40 Bio-Rad, Canada) and Ultra Visible (UV-Vis) spectroscopy (Agilent Technologies, spectrometer Cary-50)) performed to characterize the deposited materials. Electron microscopy studies were performed using a transmission electron microscope (JEOL JEM 1200 EX TEMSCAN).

4.5 Corrosion Studies

Tafel corrosion studies (potentiostat PARSTAT T2273, Princton Applied Research, USA) were performed in a 3% NaCl electrolyte to mimic sea water. PowerSuite electrochemical software package was utilized with a three electrode cell configuration. Working electrode surface area was 1 cm^2, with purified nitrogen gas being introduced into the electrolyte for degassing before measurements were taken. Standard calomel reference electrode (SCE) was used for the reference electrode and the counter electrode utilized platinum gauze. Potential change rate used was 1mV/s. The corrosion rate is calculated using equation 4-2 (D. A. Jones, 1996).

$$Corrosion\ Rate(mpy) = \frac{0.13\ I_{corr}(E.W.)}{d} \qquad \text{Eq. 4-2}$$

E.W. is the equivalent weight of the corroding species (g). Density of the corroding species (g/cm^2) is *d.* I_{corr} is the corrosion current density ($\mu A/cm^2$)

CHAPTER 5 RESULTS AND DISCUSSION

The search for safe and effective FRM that may be used as possible substitutes required testing and investigating a wide range of materials. Highly effective materials were discovered that did not always satisfy all parameters of an ideal FRM. One of the prime considerations for measuring the effectiveness of an FRM material is the mass loss percentage that is observed during TGA. The release of water and/or carbon dioxide provides dilution of fuel as well as strong endothermic reaction which may be observed in the DTA curves. Candidate materials are compared to aluminum and magnesium hydroxides, which are most widely used in applications. Material is then investigated for its EPD potential and ability to synthesize flame retardant coatings and/or composite polymer FRM coatings.

5.1 Search for Flame Retardant Material Candidates

5.1.1 Thermal Properties of Aluminum Magnesium Zirconium Hydroxide (AMZH)

Aluminum- magnesium- zirconium hydroxide (AMZH) has a Al:Mg:Zr atomic ratio of 0.78:3:0.14. As-received AMZH showed XRD peaks of hydrotalcite (Figure 15 (a)). The XRD patterns of AMZH after annealing at 500, 700, and 900^{o}C (Figure 15 (b)–(d)) showed peaks of individual oxides, indicating AMZH dehydration and decomposition. However, after decomposition at 500^{o}C and addition of water, the original hydrotalcite phase can be reconstructed (Figure 15 (e)). Therefore, in contrast to

magnesium and aluminum hydroxides, AMZH exhibits a memory effect, which offers new opportunities for advanced FRM applications. Figure 16 compares XRD, TGA and DTA data for as-received and reconstructed AMZH. The XRD pattern of as-received AMZH (Figure 16A) showed peaks for a hydrotalcite structure (JCPDS file 22-700), which disappeared after dehydration, at 500^{o}C for 2h, but appeared again in the X-ray diffraction pattern of the reconstructed material (Figure 16B). The TGA data (Figure 16C(a)) for the as received material showed several steps in mass loss below 200^{o}C and in the range of 350–400^{o}C, which are attributed to dehydration. The DTA curve in Figure 16C(b) showed corresponding endothermic behavior. The total mass loss at 1000^{o}C was 44.2 ± 0.1 mass%. The molar ratio Al:Mg:Zr:O:H_2O in AMZH was established as 0.78:3:0.14:4.45:7.83. The analysis of TGA and DTA data for the reconstructed material (Figure 16D(a) and(b)) showed a similar behavior with total mass loss of 44.3 ± 0.1 mass% at 1000^{o}C. The use of AMZH offers the advantage of a higher mass loss percentage of 44.2%, compared to aluminum and magnesium hydroxides. Moreover, in contrast to aluminum and magnesium hydroxides, AMZH exhibits a memory effect and can be reconstructed after dehydration at 500^{o}C.

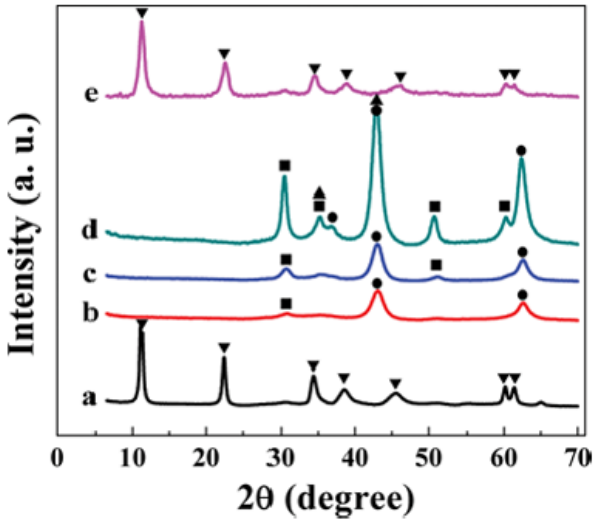

Figure 15: X-ray diffraction patterns of AMZH: (a) as-received and annealed at (b) 500, (c) 700, and (d) 900°C for 1 h, and (e) annealed at 500°C for 1 h and reconstructed (▼—hydrotalcite, JCPDS file 22-700, ●—MgO, JCPDS file 02-1207, ■—ZrO_2, JCPDS file 27-0997, ▲—Al_2O_3, JCPDS file 01-1243).

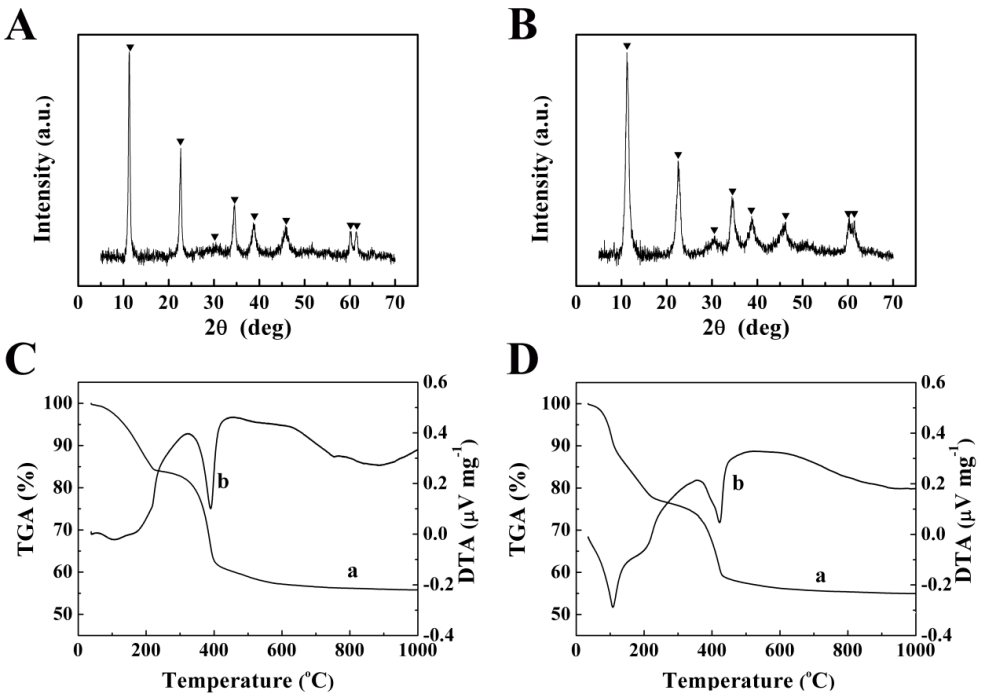

Figure 16: (A, B) X-ray diffraction patterns (▼-peaks of hydrotalcite), and (C(a), D(a)) TGA and (C(b), D(b)) DTA data for (A, C) as received and (B, D) reconstructed AMZH.

5.1.13 Thermal Properties of XZO 2022 (Mg_3Al)

XZO 2022 has low thermal stability and begins decomposition when exposed to heat at 50^{o}C. The material has a total mass loss of 45% and is completely decomposed by 500^{o}C (Figure 17). Observing the TGA data, decomposition steps occur at 50 and 200^{o}C. Endotherm at 400^{o}C represents the dehydration which occurs at 200^{o}C. Dehydrations which occur from 50-200^{o}C is represented by two smaller endotherms at 100 and 200^{o}C.

XZO 2022 is a similar material to AMZH with the absence of Zr atoms. The material consists of a hydrotalcite-like structure. Comparing the TGA/DTA data of AMZH (Figure 16) and XZO 2022 (Figure 17), it is evident that both materials undergo similar decompositions at the same temperatures with matching endotherms. Both materials have a total mass loss of 45%. AMZH surpasses the mass losses displayed by aluminum and magnesium hydroxides, it is able to release more moisture to dilute fuel and prevent combustion of host material. XZO 2022 does not have the benefit of being able to reconstruct itself after dehydration at 500^{o}C. This makes AMZH the superior choice but XZO 2022 is still an acceptable FRM candidate if compared to industry standard aluminum hydroxide.

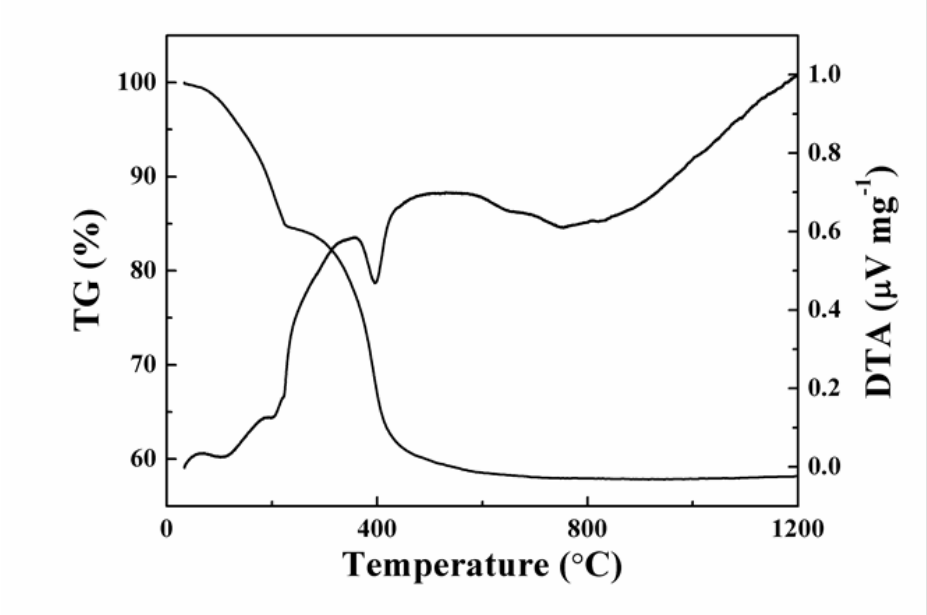

Figure 17: TGA/DTA data for as received XZO 2022, which shows a total mass loss of 45%

5.1.2 Thermal Properties of Halloysite ($Al_2Si_2O_5(OH)_4 \cdot nH_2O$)

Halloysite ($Al_2Si_2O_5(OH)_4 \cdot nH_2O$) nanotubes have an outer diameter of 60 nm and a length of 2 μm. Halloysite is a double layered aluminosilicate that has a hollow tube structure which can be observed in TEM images in Figure 18. A packing disorder in adjacent silica and alumina layers, along with their associated waters of hydration, force the structure to curve into a multilayer tube. The outer layer of the tube is chemically similar to silica while the inside of the tube relates with alumina. At a pH range of 6-7, the surface silica has a negative charge on the halloysite particle, while the inner surface alumina contributes a positive charge below pH of 8.5(Bordeepong, Bhongsuwan, Pungrassami, & Bhongsuwan, 2011).

TGA/DTA data for halloysite is displayed in Figure 19. The thermal decomposition begins at 471^{o}C and this decomposition is attributed to the loss of lattice water; a total mass loss of 18% is achieved by this material(Johnson, Guggenheim, & Groos, 1990). The total mass loss of halloysite is not as large as aluminum hydroxide and magnesium hydroxide, but its structure allows this material to perform as a dual purpose FRM. Halloysite tubular structure can be used to improve the mechanical properties when used as filler, while having the potential to release water and act as an FRM if temperatures rise to 471^{o}C. Potential application can be as an FRM in a black box; Halloysite reinforces the insulation layer during a crash, and then contributes to the fire suppression and insulation properties of the material if the box is exposed to a flame.

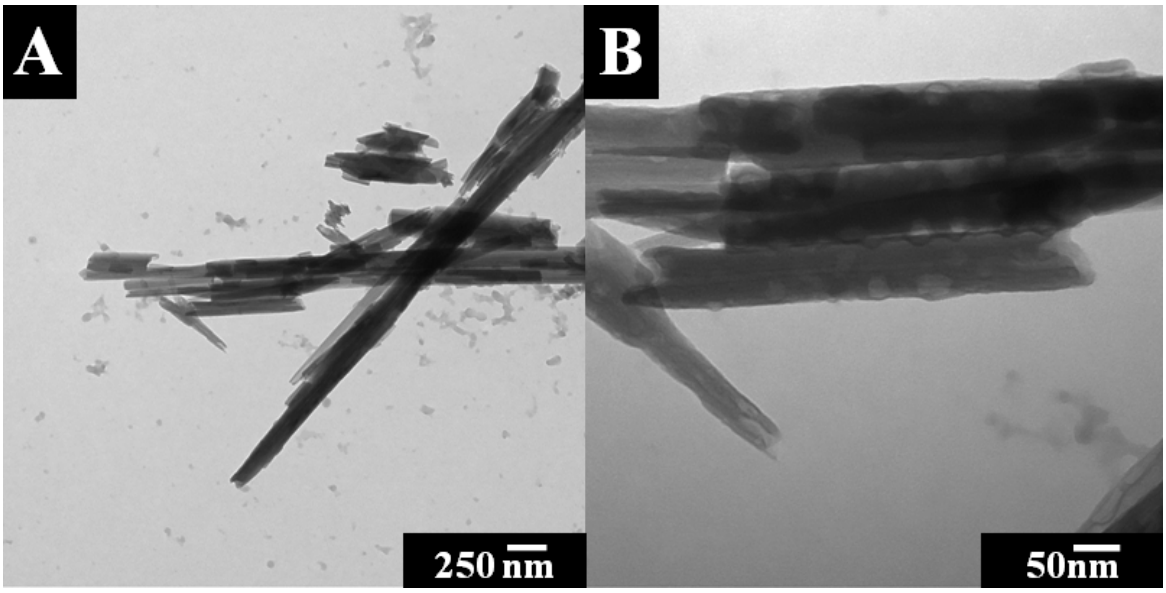

Figure 18: TEM of halloysite nanotube at two different magnifications

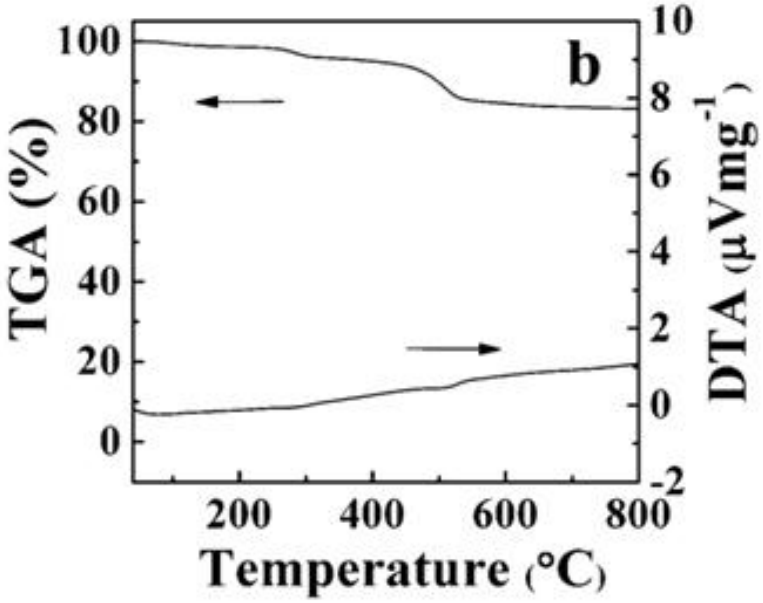

Figure 19: TGA/ DTA data for as received halloysite, which shows a total mass loss of 18%

5.1.3 Thermal Properties of Colloidal Silica (SiO_2)

Ludox colloidal silica (LCS) was tested for viability as an FRM. The as-received material was first treated at 20°C for 72 h, TGA/DTA data was then obtained and can be observed in Figure 20. An endotherm can be observed at 100°C attributed to the release of adsorbed surface water from the material. Decomposition reaction begins immediately upon heating and culminates to a total mass loss of 4.7%. Heat treating the as-received material at 80°C for 24 h results in a total mass loss of 4.5%. There is a reduction of 0.2% in total mass loss and a reduction in endotherm magnitude due to reduced release of moisture. There are no other significant changes in TGA/DTA results displayed in Figure 21 compared to material heat treated at 20°C for 24 h (Figure 20). This material has a

very low mass loss in comparison to aluminum hydroxide and magnesium hydroxide; colloidal silica will not be considered for further investigation.

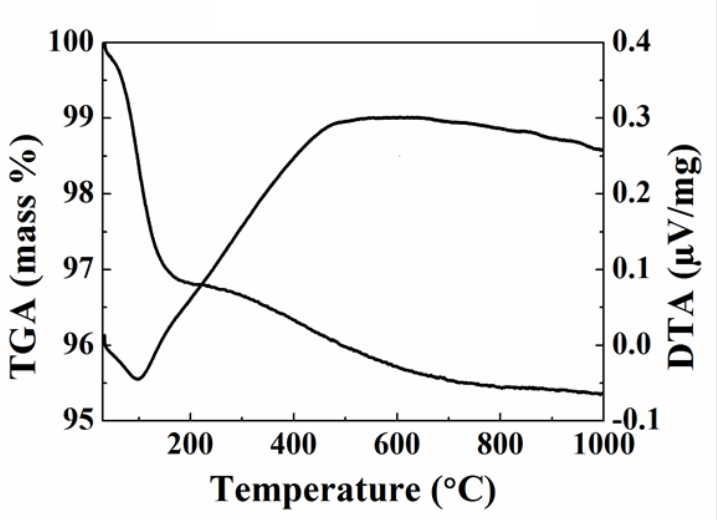

Figure 20: TGA/ DTA data for Ludox colloidal silica after being initially treatment at 20°C for 72h, which shows a total mass loss of 4.5%

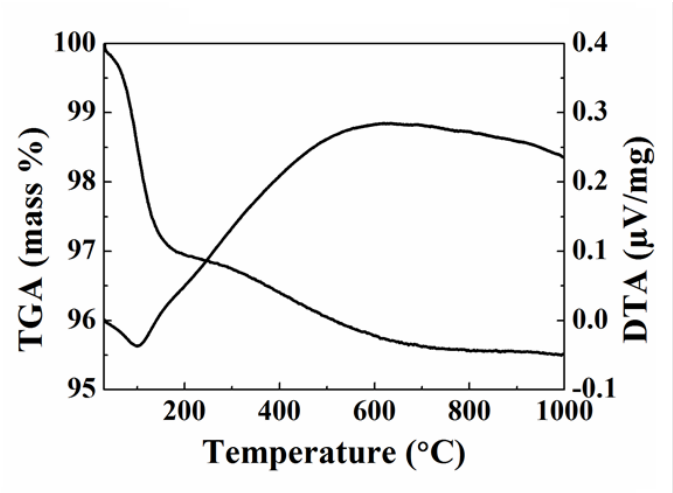

Figure 21: TGA, DTA data for Ludox colloidal silica which was initially treated at 80°C for 24h, which shows a total mass loss of 4.5%

5.1.4 Thermal Properties of Yttrium Hydroxide ($Y(OH)_3$)

Yttrium hydroxide ($Y(OH)_3$) was synthesized using yttrium nitrate ($Y(NO_3)_3 \cdot 6H_2O$) dissolved in de-ionized water. The solution was titrated with sodium hydroxide to a pH in the range of 12-14, which allowed yttrium hydroxide to precipitate. The precipitate was then filtered through a 0.45 μm Millipore filter, washed with distilled water, then washed three times with ethanol, then finally allowed to dry at room temperature for 24 h.

$Y(OH)_3$ begins decomposition at 100°C and achieves a total mass loss of 40% (Figure 22a). The decomposition is attributed to two dehydoxylations, there are two endotherms at 100°C and 500°C (Figure 22b) which coincide with the reactions. Yttrium hydroxide's endothermic reactions are necessary for absorbing energy from ignition surfaces; the large release of water helps this material dilute fuel at the ignition site. Yttrium hydroxide has a higher mass loss than both magnesium hydroxide and aluminum hydroxide. The decomposition temperature of 100°C is lower than that of both aluminum and magnesium hydroxide. This restricts the application of this candidate in materials that have a higher processing temperature. There is a constant release of water from decomposition over a wide range of 100-500°C. This is beneficial because a continuous release of water dilutes fuel allowing ignition to be inhibited over the temperature range. These properties allow this material to be an acceptable candidate for FRM applications.

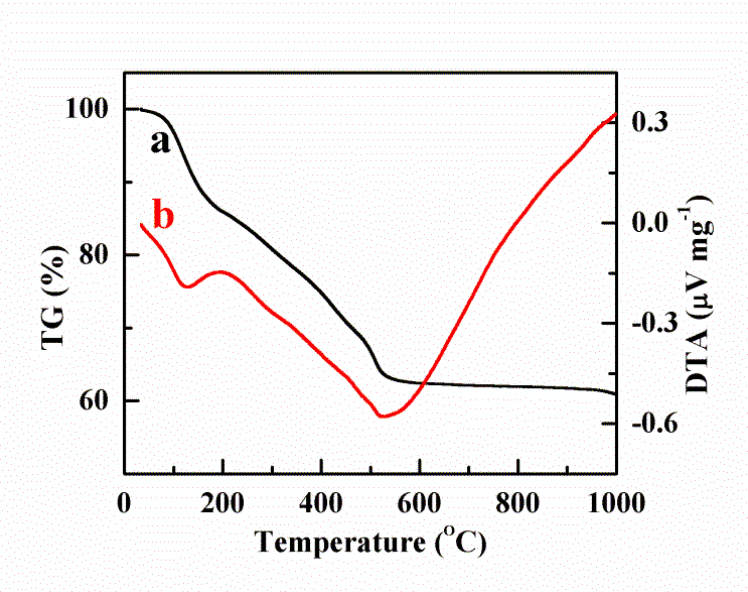

Figure 22: TGA/DTA data for $Y(OH)_3$, which show a total mass loss of 40% a) TGA, b) DTA

5.1.5 Thermal properties of YAG

Yttrium hydroxide and aluminum hydroxide composite (YAG) was synthesized by combining yttrium nitrate and aluminum sulphate into de-ionized water forming a solution which has an atomic ratio Y/AL=0.6. Titration of the solution with sodium hydroxide to a pH in the range of 7~11 allowed YAC precipitate. Precipitate is then filtered through 0.45 μm Millipore filter and washed with de-ionized water, then washed three times with ethanol and left to dry at room temperature for 24 h.

YAG is a mixture of aluminum and yttrium hydroxides which loses stability at 100°C and experiences three decompositions associated with dehydration; the total mass loss is 42%, as can be observed in Figure 23a. There are endotherms at 100, 200, and

500^{o}C which can be observed in Figure 23b. These peaks represent the three decomposition reactions which resulted in the release of water. An exothermic peak at 900^{o}C is observed and associated with the crystallization of a stable but disordered hydroxy garnet(George, Mishra, Nagar, & Jayadevan, 1996).

YAG being a composite of yttrium hydroxide and aluminum hydroxides shares many of the same properties as these materials when tested alone. The composite provides a higher mass loss, a greater amount of water loss over a larger temperature range, and a lower decomposition temperature of 100^{o}C. YAG experiences greater mass losses over a lower temperature range in comparison to yttrium hydroxide alone. At 300^{o}C the YAG has already lost 30% of its mass while yttrium hydroxide alone lost 20%. In contrast at higher temperatures between 300-600^{o}C YAG only loses 12% mass while yttrium hydroxide loses 20%. The benefits of one over the other depend on application of the host material. If the host material is sensitive to heat at low temperatures below 300^{o}C, YAG would offer better immediate protection. The exothermic crystallization peak at 900^{o}C for YAG is not desirable; yttrium hydroxide which does not display this sharp exothermic peak therefore supplying less energy into the flame front.

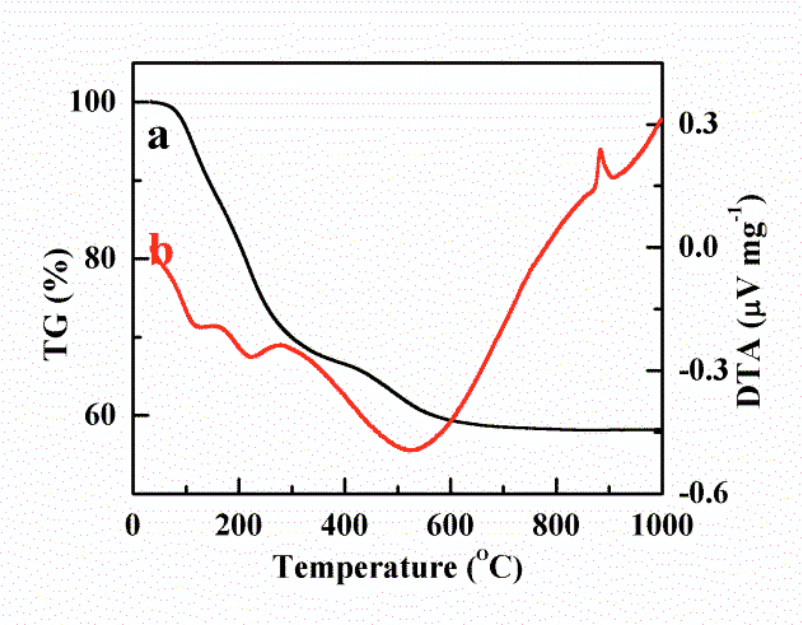

Figure 23: TGA/DTA data for YAG, which show a total mass loss of 42%. a) TGA, b) DTA

5.1.6 Thermal Properties of Alumino-Silicate (Al_2O_3-SiO_2)

Alumino-silicate material was synthesized using stock solutions of 0.1 M $Al(NO_3)_3$ and 0.1 M Na_2SiO_3, prepared using de-ionized water immediately before use. The pH values of the $Al(NO_3)_3$ and Na_2SiO_3 solutions were 3 and 8, respectively. The precipitate reaction was carried out by adding a certain volume of 0.1 M Na_2SiO_3 solution slowly into a beaker containing 100 mL 0.1 M $Al(NO_3)_3$ under gentle stirring condition. 50, and 100 mL of 0.1 M Na_2SiO_3 solution were added to 100 mL 0.1 M $Al(NO_3)_3$, resulting in precipitate samples Al:Si=2:1, and Al:Si=1:1, respectively. After the addition of Na_2SiO_3 solution, nitric acid and sodium hydroxide were used to adjust the solution pH to 7~8, followed by 3 h stirring and standing overnight. The solutions

containing alumino-silicate precipitates were passed through 0.45 μm Millipore filters and then washed thoroughly with de-ionized water. The obtained alumino-silicate precipitates were dried in air for 24 h and then under vacuum for another 24 h.

The alumino-silicate material (Al:Si=1:1, AS1) was dried overnight before obtaining TGA/DTA data in Figure 24.Thermal decomposition of alumino-silicate occurs in a single step and begins at 75^{o}C. The corresponding endotherm is located at 125^{o}C and is attributed to the loss of lattice water. The total mass loss observed is 42.8%. Exothermic peak located at 975^{o}C is associated with the crystallization of cristoballite(Xavier, Banda, & Chama, 2013).

The second alumino-silicate material (Al:Si=2:1,AS2) was dried overnight before obtaining TGA/DTA data in Figure 25. The result of AS2 mirrors that of AS1. Decomposition begins at 75^{o}C, endotherm location remains at 125^{o}C, exothermic peak is still located at 975^{o}C. Total mass loss is increased to 47.9% and a corresponding enlargement of the endotherm is observed to account for the increased release of water molecules.

The third alumino-silicate material (Al:Si=2:1, AS3) was dried overnight then followed by a heat treatment at 80^{o}C before obtaining TGA/DTA data in Figure 26. The additional heat treatment at increases the decomposition temperature to about 100^{o}C; AS3 is now more thermally stable than AS1 and AS2. The total mass loss of the material is reduced to 22.6%; a corresponding reduction in magnitude of the endotherm is attributed to less water being released. The secondary heat treatment was responsible for

removing 25% of adsorbed surface water and lattice water making it unavailable for the TGA/DTA test. The exotherm location remains the same in location and magnitude as AS2.

All three alumino-silicate candidates were associated with the release of water when heated. This satisfies the requirement of providing a mechanism to dilute the concentration of fuel near the ignition surface of a host material. AS1 and AS2 have display a larger mass loss than aluminum hydroxide and magnesium hydroxide while AS3 does not, therefore terminating its candidacy. The low decomposition temperature of AS1 and AS2 makes these materials good candidates when flame protection is desired at low temperatures. The exothermic crystallization which occurs within all three materials at 975^{o}C is not ideal and reduces the effectiveness of alumino-silicates as an FRM.

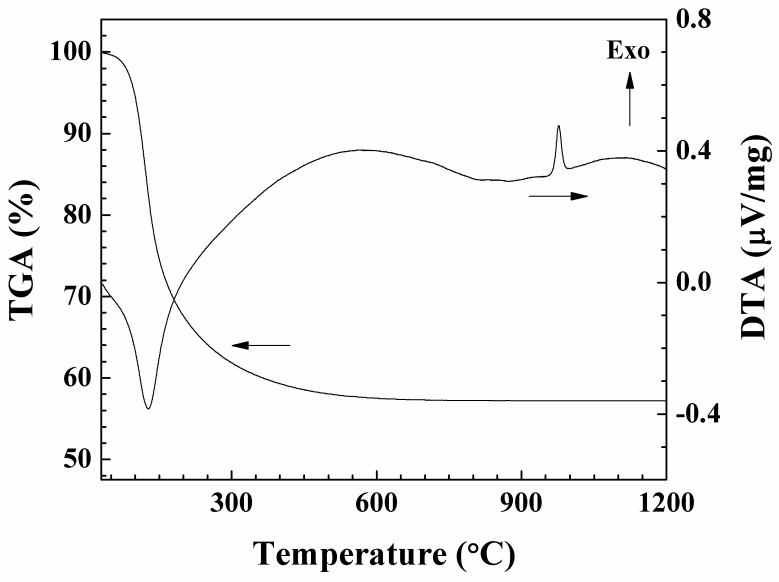

Figure 24: TGA/DTA data obtained for Al_2O_3-SiO_2 (Al:Si=1:1) that was first treated at 20^{o}C for 24h, which shows total mass loss of 42.8%

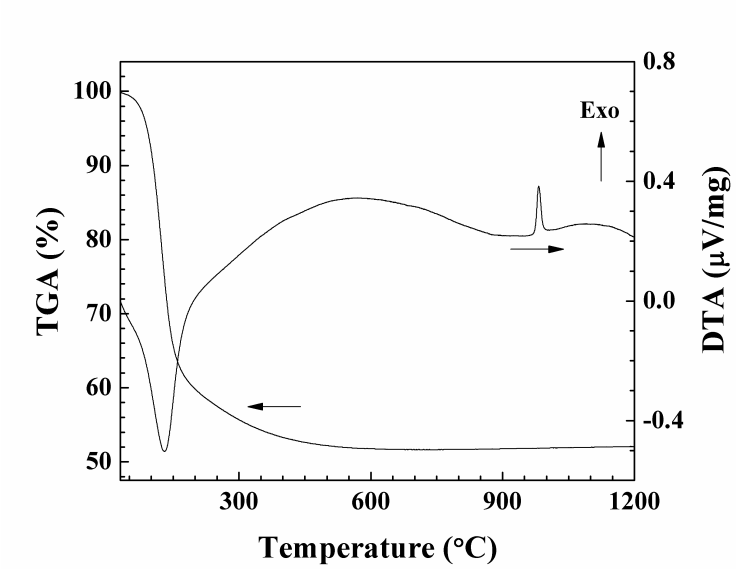

Figure 25: TGA/DTA data obtained for Al_2O_3-SiO_2 (Al:Si=2:1) that was first treated at 20°C for 24h, which shows total mass loss of 47.9%

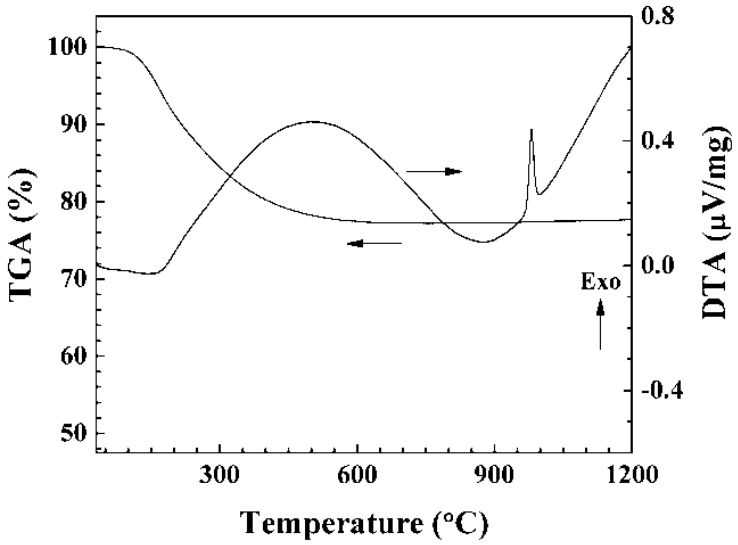

Figure 26: TGA/DTA data obtained for Al_2O_3-SiO_2 (Al:Si=2:1) that was first treated at 20°C for 24h, followed by 80°C for 24h, which shows total mass loss of 22.6%

5.1.7 Thermal Properties of Sodium Metasilicate Pentahydrate ($Na_2SiO_3 \cdot 5H_2O$)

As received sodium metasilicate pentahydrate (SMP) was heat treated at 80^{o}C for 24 h. TGA/DTA was then performed (Figure 27). Decomposition of SMP starts at a low temperature of 50^{o}C and it occurs in a single step resulting in a total mass loss of 37.5%.The large decomposition releases adsorbed surface water and lattice water molecules; Decomposition is associated with a sharp endothermic trough at 150^{o}C.

SMP has a larger mass loss than aluminum hydroxide and magnesium hydroxide, making it a viable FRM candidate. A large release of water satisfies the requirement of inhibiting the flame-fuel interaction with non-toxic molecules. The majority of the decomposition of SMP occurs in a very low and narrow temperature range (50-175^{o}C), this prevent SMP from being an FRM candidate in hosts that require processing at temperatures higher than 50^{o}C, or where the application of the material will expose SMP to 50^{o}C through regular use, such as exposure to sunlight on hot days. Large broad exothermic peak at 780^{o}C is not desirable and reduces the effectiveness of SMP to remove heat from the flame front if used as an FRM.

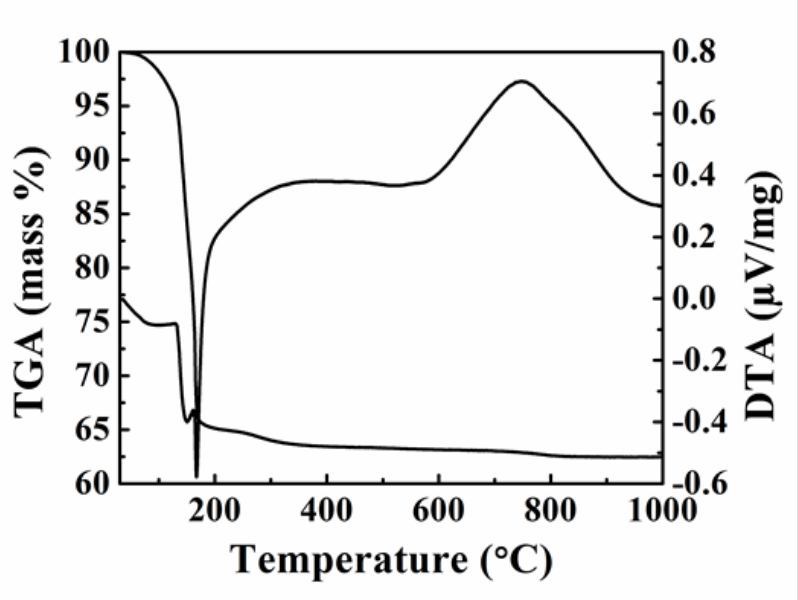

Figure 27: TGA/DTA data for as received sodium metasilicate pentahydrate, which show a total mass loss of 37.5%

5.1.8 Thermal Properties of Magnesium Carbonate Hydroxide Pentahydrate ($4MgCO_3 \cdot Mg(OH)_2 \cdot 5H_2O$)

Inspecting the TGA/DTA data for as-received magnesium carbonate hydroxide pentahydrate (MCHP), the material undergoes four major decompositions. At 80°C the decomposition is attributed to the loss of adsorbed surface water, the endotherm corresponding to this reaction is seen at 80°C. Decomposition at 200°C is attributed to the loss of lattice water, the endotherm at 275°C represent the energy absorption from this reaction. Decompositions at 375 and 500°C have corresponding endotherms at 400 and 500°C, respectively. These decompositions are related to the release of carbon dioxide and water. The total mass loss for the thermal decomposition of MCHP is 57.2% (Figure 28).

This mass loss is much greater than aluminum hydroxide and magnesium hydroxide. The material has good thermal stability up to 200^{o}C losing only 2% of total mass from surface water. If as-received MCHP is heat treated at 80^{o}C for 24 h before performing TGA/DTA, the mass loss is reduced to 55% because the adsorbed surface water is removed (Figure 29). This thermal stability is now equivalent to that of aluminum hydroxide, but lower than that of magnesium hydroxide. The temperature range of decomposition (200-550^{o}C) in magnesium carbonate hydroxide pentahydrate is wider than that of magnesium hydroxide and aluminum hydroxide, this gives the benefit of having a constant release of water and carbon dioxide molecules to dilute the fuel as a flame progresses. There is a large exothermic reaction that occurs at 500^{o}C, this is undesirable in the material which is to be used as an FRM because a sudden influx of energy will aid the host material in achieving its ignition temperature.

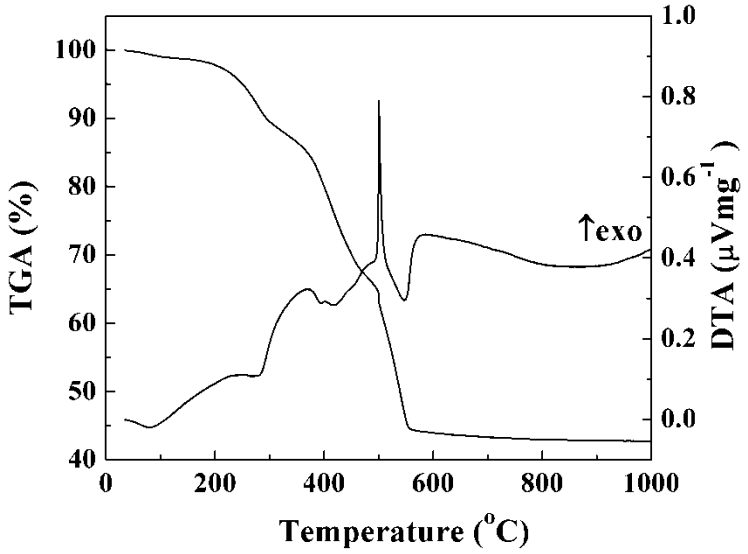

Figure 28: TGA/ DTA data obtained for as received magnesium carbonate hydroxide pentahydrate, which shows a total mass loss of 57.2%

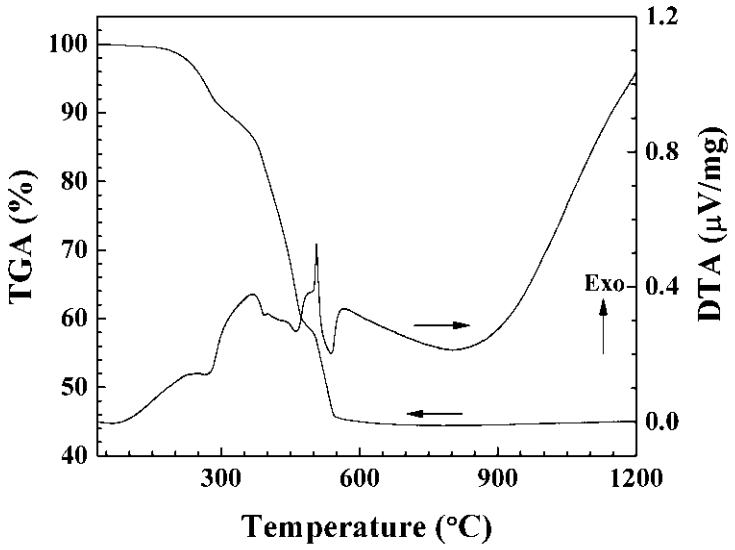

Figure 29: TGA/DTA data obtained after magnesium carbonate hydroxide pentahydrate treated at 80°C for 24 h, which shows a total mass loss of 55%

5.1.9 Thermal Properties of Magnesium Sulfate Heptahydrate ($MgSO_4 \cdot 7H_2O$)

Magnesium sulfate heptahydrate has a total mass loss of 46% by releasing water molecules (Figure 30). The decomposition consists of four dehydration reactions which start at 100, 125, 175, and 300^{o}C. The corresponding endotherms can be observed at 175, 200, 250, and 325^{o}C, respectively.

The material is a great FRM candidate as it has a larger mass loss compared to aluminum and magnesium hydroxides. The release of water molecules and corresponding absorption of heat allows the candidate to dilute fuel and reduce the temperature at the surface exposed to the flame front. There are no large exothermic peaks to hinder FRM capabilities, as were observed in MCHP. The material begins decomposing at a low temperature of 100^{o}C making it inapplicable for thermosets or thermoplastic which require better thermal stability to withstand higher processing temperature. The material is fully decomposed by 325^{o}C making it a good candidate for applications requiring an immediate fire suppressive in a lower temperature range. Magnesium sulfate heptahydrate can be combined into a composite FRM with a partner that decomposes above 325^{o}C, such as huntite. This composite will be able to offer protection over a wide temperature range of 100-700^{o}C, because as Magnesium sulfate heptahydrate becomes fully dehydrated the temperature increases to the decomposition temperature of huntite allowing it to start releasing carbon dioxide and continue protecting the host material.

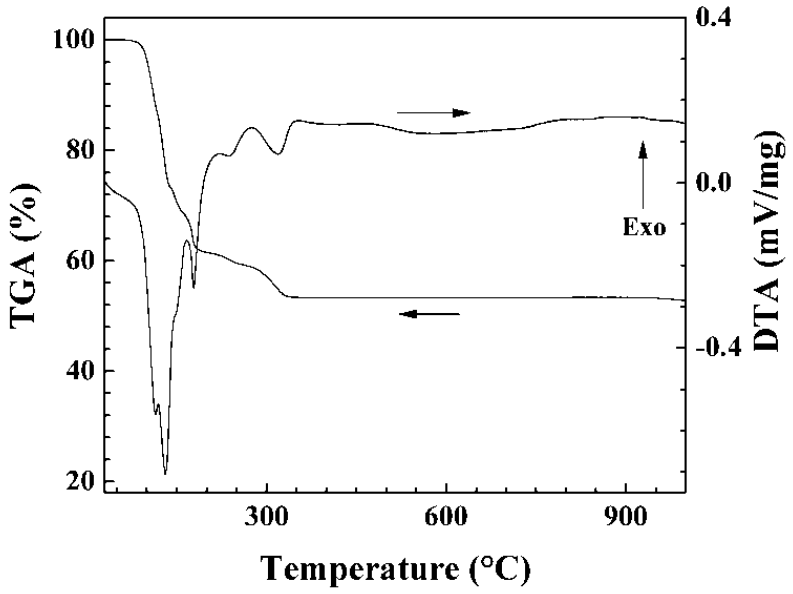

Figure 30: TGA/DTA data for as received magnesium sulfate heptahydrate, which show a total mass loss of 46%

5.1.10 Thermal Properties of Magnesium Phosphate Hydrate ($Mg_3(PO_4)_2 \cdot xH_2O$)

The thermal decomposition of magnesium phosphate hydrate has a total mass loss of 22% (Figure 31). The decomposition is attributed to dehydration, where lattice and adsorbed water are released. Endotherms at 100 and 275^{o}C are associated with this decomposition. At 675^{o}C an exothermic peak is evident, attributed to the crystallization of the $Mg_2P_2O_7$ lattice (Roy, Middleswarth, & Hummel, 1948).

Mass loss of magnesium phosphate hydrate is less than that of aluminum hydroxide by 12% and 8% lower than magnesium hydroxide. The reduced mass loss will decrease the effectiveness of magnesium phosphate hydrate as an FRM because a lower

amount of water molecules are released to dilute the fuel at the flame front and absorb heat from the host material. The decomposition temperature range for this material is similar to aluminum hydroxide offering no advantage for magnesium phosphate hydrate. In addition the exothermic event which occurs at 675°C in magnesium phosphate hydrate reduces the effectiveness of using the material as an FRM. There are no benefits offered by magnesium phosphate hydrate over aluminum hydroxide which will make it a poor candidate for FRM applications.

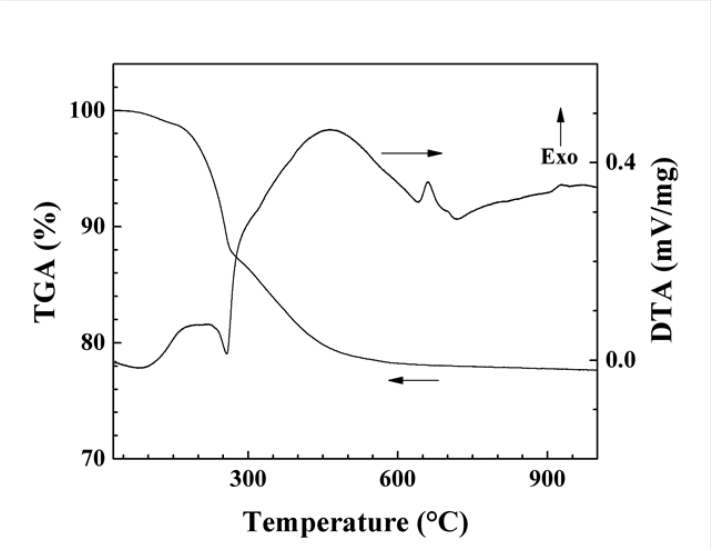

Figure 31: TGA/DTA data for as received magnesium phosphate hydrate, which show a total mass loss of 22%

5.1.11 Thermal Properties of Magnesium Chloride Hexahydrate ($MgCl_2 \cdot 6H_2O$)

Magnesium chloride hexahydrate experiences many thermal decompositions in the temperature range of 100-900°C (Figure 32). A substantial total mass loss of 80% is achieved through dehydrations at 100, 200, 275, 450 and 900°C. There are many

endotherms evident in the DTA data. This suggests that a combination of smaller reactions, losing one water molecule at a time, contribute to the five visible decompositions in the TGA data. Literature (Wu et al., 2014) suggests that at 167^{o}C Magnesium chloride hexahydrate releases Cl^{-} free radicals; free radicals can inhibit a combustion chain reaction. The release of Cl^{-} free radicals and water will dilute the fuel and inhibit gas phase reactions in a flame front.

Magnesium chloride hexahydrate has a low thermal stability in relation to magnesium and aluminum hydroxides, limiting its addition into materials that require a higher than 100^{o}C processing temperature. Magnesium chloride hexahydrate release of Cl^{-} allows it to make use of multiple flame retarding techniques. Magnesium chloride hexahydrate releases almost 45% more water than aluminum hydroxide. Magnesium chloride hexahydrate is theoretically a superior FRM to aluminum and magnesium hydroxides, but the presence of chlorine free radicals may have negative effects such as chemical attack of host material, decrease of local pH may disturb the order of intumescent char formation if Magnesium chloride hexahydrate is used synergistically with intumescent FRM. Additional acid source will extend char formation time, when the second step of blowing agent activation occurs within the intumescent material, char expansion will be impeded. Although Magnesium chloride hexahydrate is an effective FRM, the potential hazards and unfavorable effects on its surroundings, Magnesium chloride hexahydrate is not a strong candidate in the search for environmentally safe non-toxic FRM.

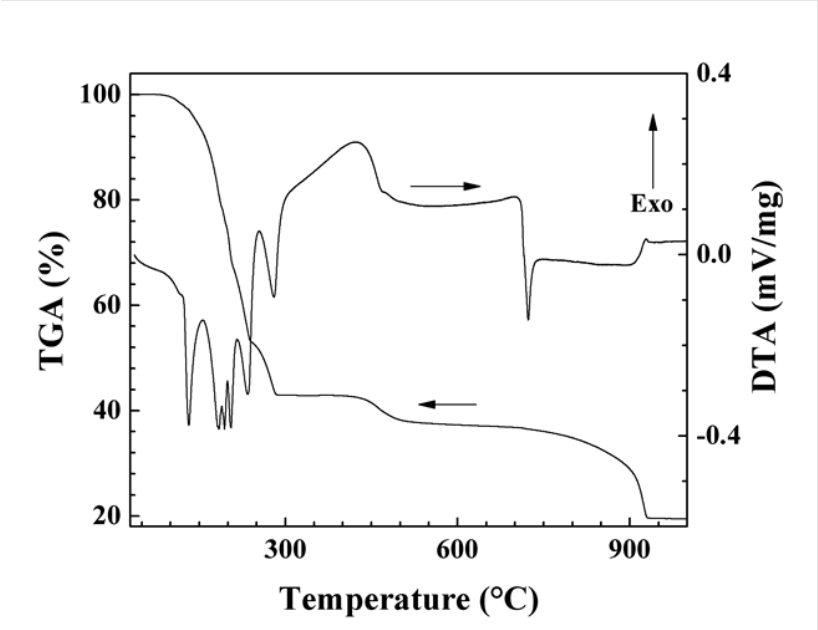

Figure 32: TGA/DTA data for as received magnesium chloride hexahydrate, which show a total mass loss of 80%

5.1.12 Thermal Properties of Hydrotalcite ($Mg_6Al_2CO_3OH_{16}\cdot 4H_2O$)

The thermal decomposition of Hydrotalcite has a total mass loss of 45% (Figure 33). The decompositions at 200, 250, and 400^{o}C are attributed to dehydration through moisture and surface hydroxyl removal. Endotherms associated with these decompositions are located at 250, 375 and 425^{o}C, respectively.

Hydrotalcite displays a mass loss 11% greater than aluminum hydroxide and 15% greater than magnesium hydroxide. Thermal stability of up to 200^{o}C and a decomposition range of 200-500^{o}C makes hydrotalcite equivalent to aluminum hydroxide, but unfortunately there are two exothermic reactions that occur at 350 and 400^{o}C which are

not desirable in an FRM candidate. Hydromagnesite is very effective at diluting fuel at the ignition surface inhibiting combustion with a large release of water molecules. Hydrotalcite would make a good FRM candidate for coatings with further research into dispersing and charging agents to complement.

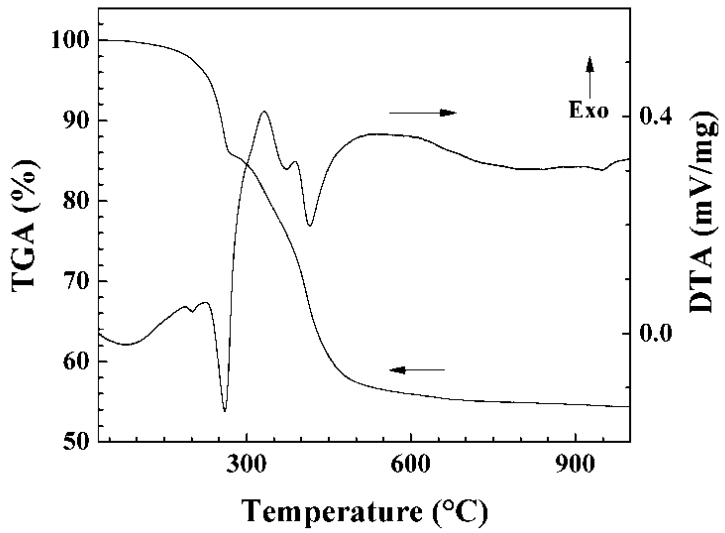

Figure 33: TGA/DTA data for as received hydrotalcite, which show a total mass loss of 45%

Twelve materials were investigated as potential candidates as FRM materials. Materials had performed better than industry standard aluminum hydroxide FRM and are considered promising candidates for further investigation. Of the materials tested, LCS and magnesium phosphate hydrate were eliminated due to having a low mass loss of only 4.5 and 22%, respectively. Halloysite had a mass loss of only 18%, but is considered a promising candidate due to its tube like structure allowing it to improve mechanical properties as well as act as an FRM. Magnesium chloride hexahydrate despite its large

mass loss of 80% was eliminated due to the potential difficulties which may result from the release of chlorine free radicals. AMZH and XZO 2022 were similar materials in which AMZH was superior due to it memory behavior; therefore XZO 2022 will not be investigated further. Among the similar candidates AS1 and AS2 , AS2 displayed the largest mass loss and will be the chosen candidate from the group. Magnesium sulfate heptahydrate, magnesium sulphate pentahydrate, AS2, YAG, ($Y(OH)_3$) AMZH, and hydrotalcite are all acceptable candidates. These most promising materials, along with huntite and aluminum hydroxide were then investigated for EPD of FRM coatings.

5.2 Fabrication of Advanced Flame Retardant Coating

5.2.1 Electrophoretic Deposition of a Memory-Type Flame Retardant Material

EPD of aluminum- magnesium- zirconium hydroxide (AMZH) was performed using aurintricarboxylic acid ammonium salt ($ATNH_4$) as a dispersing, charging, binding, and film-forming agent. EPD was performed from 10 g/L AMZH suspensions in water, containing 0–1.5 g/L $ATNH_4$ at a deposition voltage of 7 V. The coatings were dried in air for 48 h.

Previous investigations showed that aurintricarboxylic acid (ATH) films can be deposited from aqueous $ATNH_4$ solutions (Y. Sun, Ata, & Zhitomirsky, 2012). The deposition mechanism was based on a pH decrease at the anode surface due to the electrochemical decomposition of water as in equation 5-1, protonation of COO^- groups and formation of insoluble aurintricarboxylic acid (ATH) films.

$$2H_2O \rightarrow O_2 + 4H^+ + 4e^- \quad \text{Eq. 5-1}$$

Previous studies (Y. Sun et al., 2012) showed a possibility of EPD of titanium dioxide using $ATNH_4$. As an extension of the previous investigations we found that hydroxide materials, such as AMZH, can be deposited from aqueous suspensions, containing $ATNH_4$. Due to the limitations of using zeta-potential for analyzing the electrokinetic behavior of particles, containing large adsorbed organic molecules, the deposition process was analyzed using the deposition yield data. Figure 34A indicates that the deposition rate increased with increasing $ATNH_4$ concentration, in the range of 0.4–1.5 g/L, within the suspensions. The increase in the deposition time resulted in increasing coating mass, indicating continuous coating growth. Therefore, the amount of the deposited material can be controlled by the variation of $ATNH_4$ concentration and deposition time. It is suggested that anionic AT^- adsorbed on the surface of AMZH and imparted a charge for EPD. Previous investigations showed that AT^- adsorbed on titanium oxide surface via an inner sphere bonding mechanism, involving complexation of Ti atoms on the particle surface(Y. Sun et al., 2012). It was found (Jankovic, Saponic, & Comor, 2009) that under coordinated defect sites on the surface of titanium dioxide are the source of enhanced and selective reactivity of the nanoparticles toward bidentate ligand bonding of phenolic molecules. For hydroxide materials, such as AMZH, we suggest outer sphere bonding mechanism (Ata, Liu, et al., 2014), involving OH groups (Figure 34C). The deposition mechanism involved the electrophoretic motion of AMZH, containing adsorbed anionic

AT^- species, toward the anode. The pH decrease at the anode surface resulted (equation 5-1) in the protonation of AT^- and charge neutralization (Figure 34C). The formation of electrically neutral and insoluble ATH, with excellent film forming and binding properties (Y. Sun et al., 2012), promoted the formation of AMZH coatings. Figure 35 displays typical SEM images of AMZH coatings, which adhered well to the substrates and exhibited relatively low porosity, mainly attributed to packing of the AMZH particles. The porosity can also be attributed to gas evolution at the electrode during EPD associated to the oxygen gas release following equation 5-1.

The AMZH coatings were scraped from the substrates and tested by UV–vis and FTIR methods (Figure 36). The UV–vis spectrum of the deposited material showed broad absorptions at 300– 320 nm and around 530 nm, attributed to ATH (Mallah, Maragheh, Badiei, & Sbo, 2010). The FTIR spectrum showed broad absorptions centered at 1628 and 1488cm^{-1}, attributed to C─C/C═C vibrations of aromatic rings. There is also a broad adsorption centered at 1352cm^{-1},this is related to bending vibrations of C─OH groups and C─O vibrations of ATH (Jankovic et al., 2009; Y. Sun et al., 2012). Small peaks at 1133 and 1039 cm^{-1} were related to bending C─H vibrations (Jankovic et al., 2009; Y. Sun et al., 2012). Therefore, the UV–vis and FTIR data confirmed that deposited AMZH coatings contained adsorbed ATH in agreement with the proposed EPD mechanism. The AMZH material and EPD deposition method are promising for the fabrication of advanced FRM coatings. It is important to note that many traditional coating deposition techniques involve high temperature processing and cannot be used for the deposition of hydroxides. Films of metal hydroxides are usually prepared by electrolytic deposition

(Zhitomirsky, 2002). However the electrolytic deposition can be used for deposition of very thin films at relatively low deposition rates. Moreover, difficulties are attributed to deposition of complex hydroxides, such as AMZH, and control of deposit composition (Zhitomirsky, 2002). In contrast, EPD allows the deposition of stoichiometric compounds at relatively high deposition rate (Zhitomirsky, 2002). It is important to note that irreversible thermal dehydration of aluminum and magnesium hydroxides limits their application for fabrication of composites by techniques which involve thermal processing of matrix materials. This limitation can be avoided by using memory-type FRM, such as AMZH.

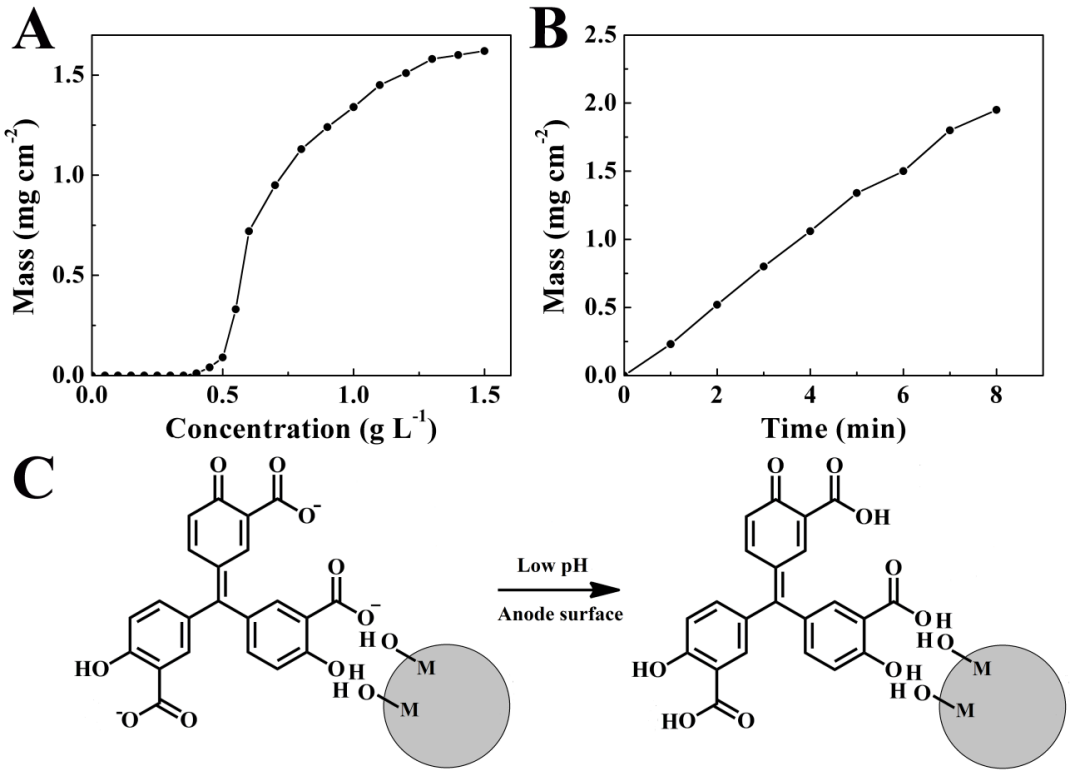

Figure 34: Deposit mass versus (A) $ATNH_4$ concentration at a deposition time of 5 min and (B) deposition time at $ATNH_4$ concentration of 1g/L and (C) schematic of particle deposition using $ATNH_4$

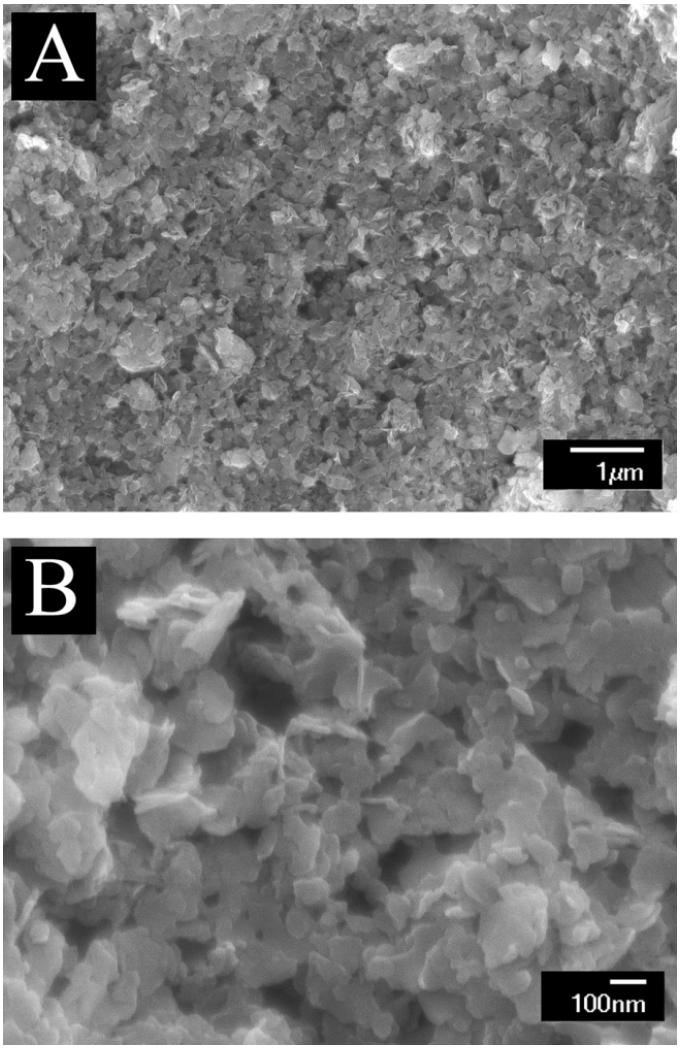

Figure 35: SEM images of AMZH coating at different magnifications.

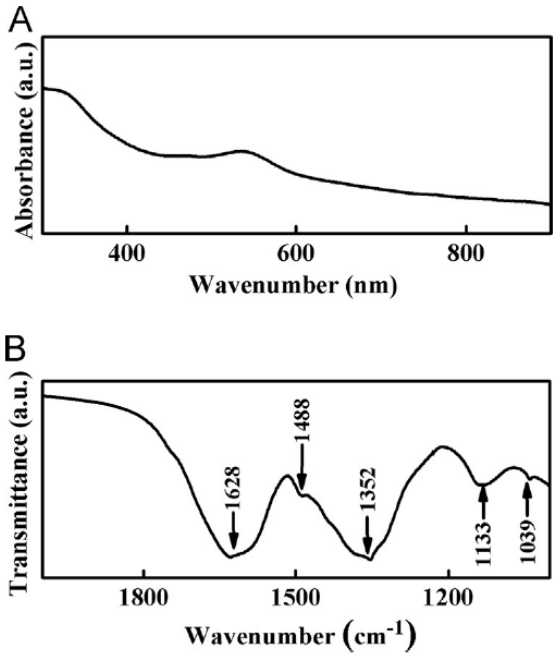

Figure 36: (A) UV–vis and (B) FTIR data for deposited AMZH.

5.2.2 Composite Polymer-Metal Hydroxide Coatings with Flame Retardant Properties

The reconstructed AMZH was prepared by annealing of as-received AMZH at 500^{o}C for 2 h, addition of water with a AMZH=water mass ratio of 1:1, and drying for 24 h in air. The protonation and dissolution of PVBM(L. Yang, Pang, Fox-Rabinovich, Veldhuis, & Zhitomirsky, 2012) and CHIT(Deen, Pang, & Zhitomirsky, 2012) was performed in acetic acid solutions. AMZH was dispersed in ethanol using CBD. Then PVBM and CHIT solutions were prepared in water-mixed ethanol (20% water) solvent, containing AMZH particles and CBD dispersant. The deposition voltage was 50V.

The addition of CBD to AMZH suspensions resulted in improved suspension stability, and allowed the formation of AMZH deposits on the stainless steel substrates. The formation of cathodic deposits indicated that cationic CBD molecules adsorbed on AMZH and imparted a positive charge. The mass of deposited AMZH increased with an increase in CBD concentration at fixed deposition time, and also with increased deposition time at a fixed CBD concentration (Figure 37). Therefore, the formation of AMZH films by EPD can be performed at a controlled deposition rate.

The AMZH deposits were removed from the substrates and studied by UV–Vis and FTIR methods. The UV–Vis spectrum (Figure 38(a)) of AMZH deposit showed a broad absorption in the range of 500–620 nm, related to CBD(Saroj & Chhagan, 2013), adsorbed on the AMZH particles. The absorptions at 1634, 1576, and 1439 cm^{-1} in the FTIR spectrum were related to C–C aromatic (Figure 39) stretching vibrations (Liu et al., 2014) of adsorbed CBD. The stretching vibrations of CBD carboxyl group (Ata, Zhua, Botton, & Zhitomirsky, 2014) contributed to absorption at 1384 cm^{-1}. The absorption peaks at 1276 and 1232 cm^{-1} can result from stretching C–O vibrations of CBD (Dobson & McQuillan, 2000). The peaks in the range of 1043–1181 cm^{-1} were related to bending C–H vibrations of CBD (Dobson & McQuillan, 2000).

Figure 39 shows the adsorption mechanism of CBD, which belongs to the catechol family of materials. It is known (Ata, Liu, et al., 2014; Ata, Zhua, et al., 2014) that catechol-type molecules exhibit strong adsorption on oxide particles, by mechanism involving OH groups of the catechol ligand. CBD adsorbed on oxide surface via an inner sphere bonding mechanism, based on the complexation of surface metal atoms of the

particles (Ata, Liu, et al., 2014; Ata, Zhua, et al., 2014). The important properties of CBD as a dispersant are related to strong adsorption of CBD on the particle surface and electric charge, which allowed efficient electrosteric stabilization. We suggest that in the case of hydroxide materials, the adsorption is achieved via the outer sphere adsorption mechanism (Y. Wang & Zhitomirsky, 2012), involving surface OH groups of the AMZH particles and OH groups of the catechol ligand of CBD. The results presented in Figure 36 and Figure 37 showed that adsorbed CBD imparted a positive charge to AMZH particles for cathodic EPD. However, the AMZH films showed poor adhesion to the stainless steel substrates. The positively charged particles of AMZH were combined with cationic polymers, such as PVBM and CHIT, for the fabrication of adherent films. The mechanisms of deposition of PVBM (L. Yang et al., 2012) and CHIT (Deen et al., 2012) involved electrophoresis of protonated polymers, cathodic pH increase due to electrochemical reduction of water as seen in equation 5-1, neutralization of the electric charge of the polymers, and formation of insoluble films. The polymers were co-deposited with AMZH particles and formed composite films. XRD studies of the composite films showed peaks of the AMZH hydrotalcite phase (Figure 40). The composite films were also examined by SEM. The electron microscopy images show AMZH particles in the polymer matrices (Figure 41). The size of the individual particles is about 0.1 mm; however some particles formed larger agglomerates, containing 3–5 individual particles. The method allowed the fabrication of relatively dense films with thickness in the range of 0.5–20 mm. However, small voids with size below 0.1 mm were observed between individual particles in the agglomerates. The TGA data for the AMZH,

tested in the range of 20–600^{o}C, showed mass loss of 44.2%. The composite deposits showed additional mass loss, resulting from burning out of the polymers (Figure 42). The DTA data showed endothermic peaks, related to thermal dehydration of AMZH. TGA/DTA data also confirmed the adsorption of CHIT and PVBM due to the additional mass loss associated to decomposition of dispersants.

AMZH is a promising FRM material, due to higher mass loss of 44.2%, compared to aluminum hydroxide and magnesium hydroxide. EPD method for AMZH deposition offers processing advantages, such as possibility of uniform deposition on substrates of complex shape and high surface area. EPD allows rigid control of deposition rate, deposit composition, and stoichiometry. Many traditional coating manufacturing techniques require processing at elevated temperatures and cannot be used for the deposition of hydroxides. Thin films of individual hydroxides can be prepared by cathodic electrosynthesis at relatively low deposition rates (Zhitomirsky, 2002). However, the deposition of complex hydroxides, such as AMZH, presents difficulties attributed to the control of deposition rate of individual components and control of the deposit stoichiometry. EPD allows deposition of complex compounds of desired composition at significantly higher deposition rates and thick films can be obtained. Moreover, the EPD method allows co-deposition of inorganic materials and polymers. The composite coatings exhibit additional functional properties, such as corrosion protection, as it is illustrated in Figure 43. The comparison of the Tafel plots for coated and uncoated stainless steels substrates indicated that coated samples showed increased corrosion potential and reduced anodic current, which indicated corrosion protection. The corrosion

rates were found to be 0.0264, 0.0130, and 0.0218mm per year for uncoated stainless steel, PVBM– AMZH coated stainless steel, and CHIT– AMZH coated stainless steel, respectively.

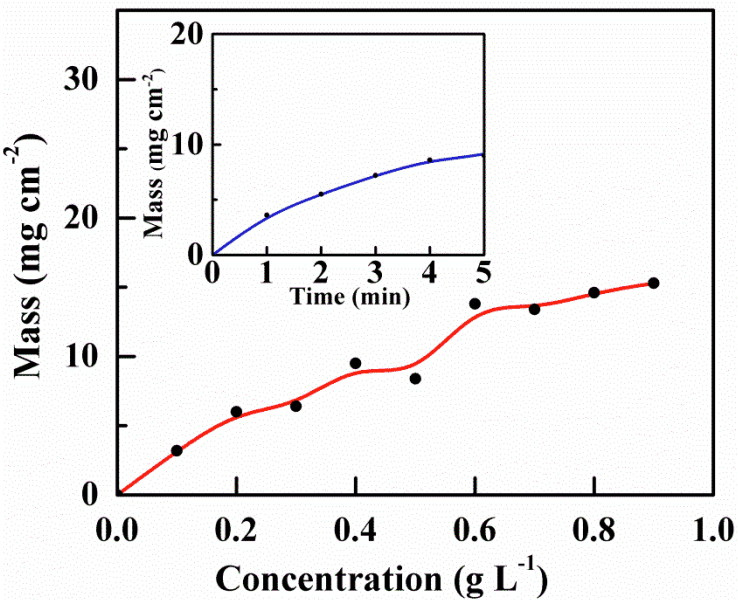

Figure 37: Deposit mass of AMZH versus CBD concentration in 10 g/L AMZH suspension in ethanol at a deposition voltage of 50V and deposition time of 5 min. Inset shows deposit mass versus time dependence at CBD concentration of 0.5 g/ L.

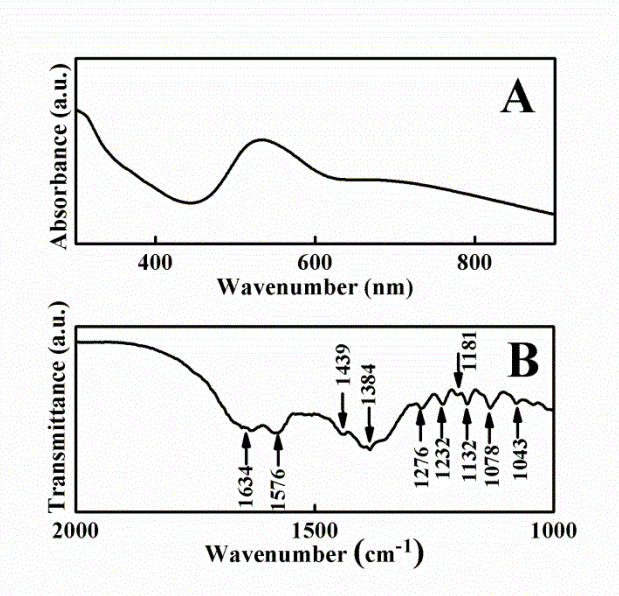

Figure 38: (a) UV–Vis and (b) FTIR spectra of MAZ deposit, prepared by EPD from 10 g/L AMZH suspension in ethanol, containing 0.5 g/L CBD.

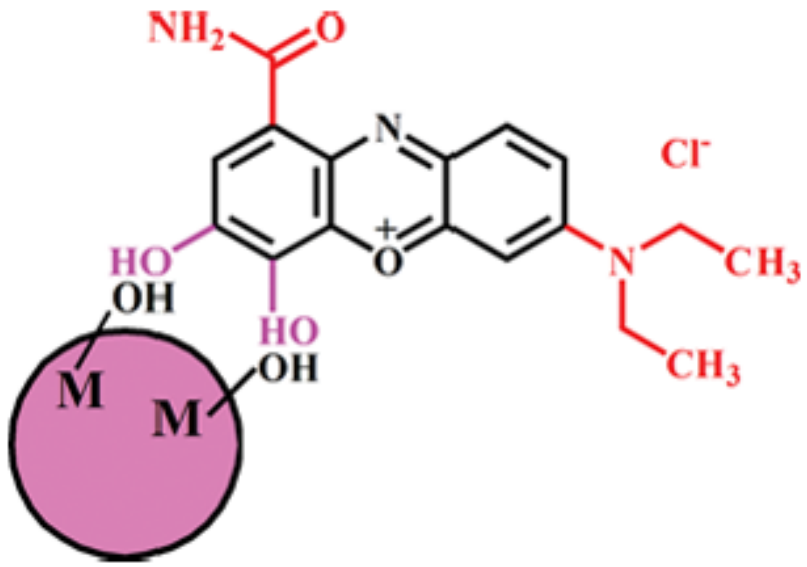

Figure 39: Adsorption of polyaromatic CBD on AMZH surface (M–Al, Mg or Zr atoms of AMZH).

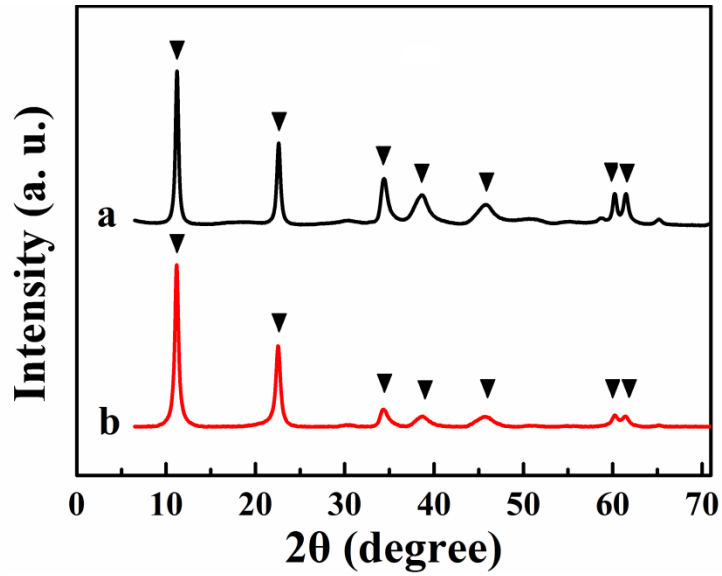

Figure 40: XRD diffraction patterns of the deposits, prepared from (a)0.5 g/L PVBM solution, and (b) 0.5 g/L CHIT solution, containing 0.5 g/L CBD and 4 g/L AMZH (▼-peaks of hydrotalcite, JCPDS file 22-700).

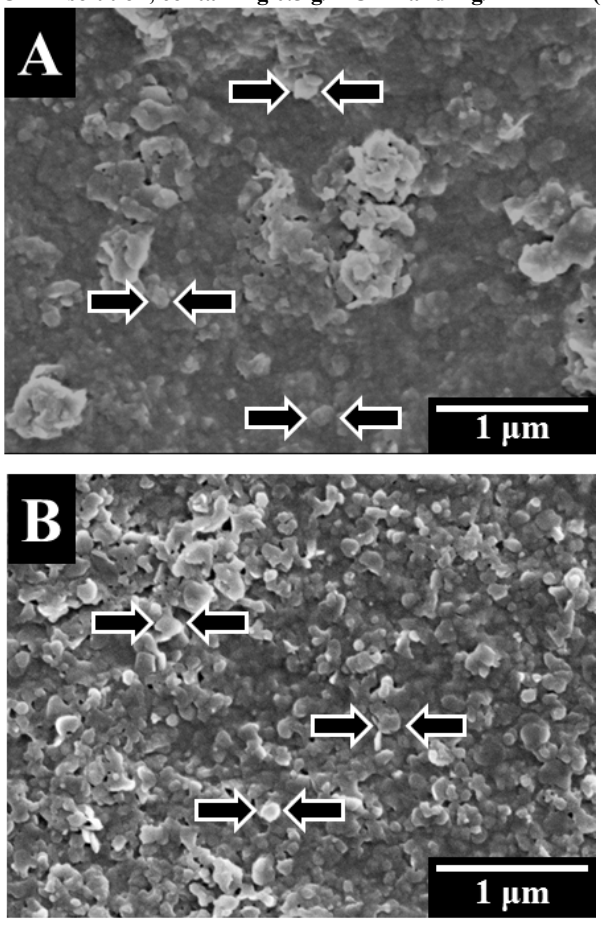

Figure 41: SEM images of coatings prepared by EPD from (a) 0.5 g/L PVBM solution (b) 0.5 g/L CHIT solutions, containing 0.5 g/L CBD and 4 g/L AMZH. Arrows show AMZH.

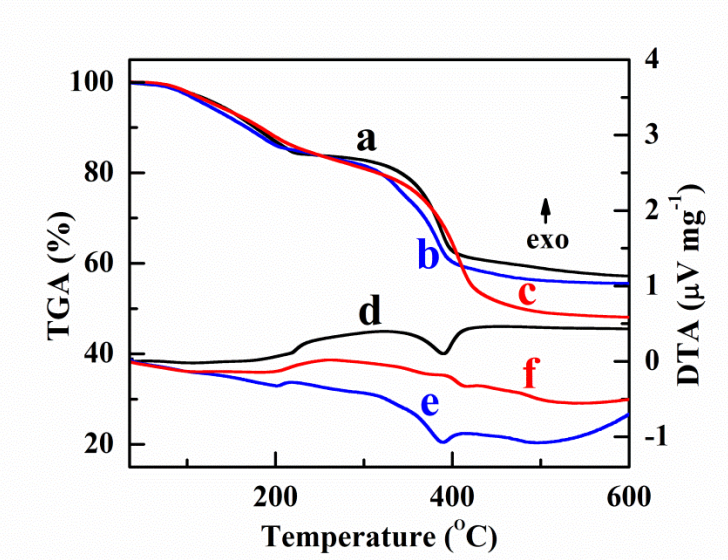

Figure 42: (a, b, c) TGA and (d, e, f) DTA data for (a, d) as-received AMZH, (b, e) deposit, obtained from 0.5 g/L PVBM solution (c, f) deposit, obtained from 0.5 g/L CHIT solution, containing 0.5 g/L CBD and 4 g/L AMZH.

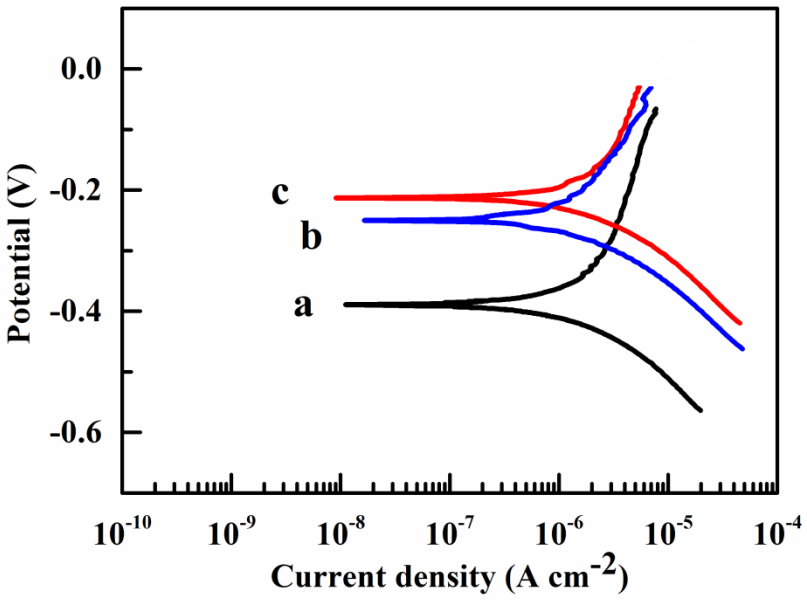

Figure 43: Tafel plots for (a) uncoated stainless steel, and coated with a composite coating prepared from (b) 0.5 g/L PVBM solution and (c) prepared from 0.5 g/L CHIT solution, containing 0.5 g/L CBD and 4 g/L AMZH. The electrode potential was measured versus saturated calomel electrode.

5.2.3 Electrophoretic Deposition of materials Using Humic Acid as a Dispersant and Film Forming Agent

Humic acid (HA) is one of the most abundant organic macro-molecules on the Earth (M. N. Jones & Bryan, 1998). It exhibits a unique set of properties, such as strong adsorption on various organic and inorganic materials, chelating and redox active properties (M. N. Jones & Bryan, 1998). Of particular interest is the ability of HA to bind virtually all transition metals and a high binding capacity (M. N. Jones & Bryan, 1998). Metal chelation is a salient feature of HA, which allows for HA adsorption on surfaces of various inorganic materials. HA showed strong adsorption on different minerals, such as palygorskite (M. Wang, Liao, Zhang, & Li, 2012), kaolinite and hematite(Shaker, Komy, Heggy, & El-Sayed, 2012; Vermeer, Van Riemsdijk, & Koopal, 1998) and different oxides such as Al_2O_3(Janot, Reiller, Zheng, Croué, & Benedetti, 2012) and SiO2(Pitois, Abrahamsen, Ivanov, & Bryan, 2008). HA, adsorbed on mineral particles, promoted the sorption of organic molecules as well as cations of metals(Arias, Barral, & Mejuto, 2002; Ellyn M. Murphy, Zachara, & Smith, 1990). Hybrid double hydroxides-HA materials have been developed, which allowed good adsorption of heavy metals (González, Pavlovic, Rojas-Delgadob, & Barriga, 2014).

The adsorption of metal ions on alumina nanoparticles was enhanced in the presence of HA due to the formation of ternary complexes (Stietiya & Wang, 2014). Moreover, HA efficiently adsorbed on hydroxides(Gasser, Mohsen, & Aly, 2008), and polymers(Wan Ngah & Musa, 1998). HA showed strong interactions with various polyaromatic molecules. The interactions involved different chemical mechanisms, such

as ion exchange reactions, ion bridging, hydrogen bonds, charge transfer, covalent bond formation and hydrophobic interactions (Karthikeyan & Chorover, 2002). Of particular importance are investigations of HA interactions with herbicides and pesticides used in agriculture(M. N. Jones & Bryan, 1998). Figure 44 shows a schematic of the chemical structure of HA, which includes aromatic rings, hydrocarbon chains and anionic functional groups, such as carboxyl and phenol groups. The structural properties of HA facilitate chemical interactions with a variety of organic and inorganic materials via multiple reaction pathways. A discrete fragment model has been developed for the analysis of contributions of different ligands to the chelating properties of HA (Sasaki, Kobayashi, Takagi, & Moriyama, 2008). Of particular interest are catechol and salicylate ligands (Figure 44), which showed strong complexation with metal atoms (Ata, Liu, et al., 2014).

Many investigations were focused on the analysis of adsorption mechanisms (Gasser et al., 2008; Darren Delai Sun & Lee, 2012) and kinetics (Eita, 2011). It was found that HA adsorption on oxides exhibited a complex behavior. It was initiated by electrostatic interactions and followed by the ligand exchange and surface complexation, involving carboxylic groups of HA. The adsorption was governed by different factors (Janot et al., 2012), including solution pH and ionic strength. The adsorption mechanism was based on the complexation of metal atoms on the material surface with HA ligands (Tombácz et al., 2013) and electrostatic attraction (Stietiya & Wang, 2014). It was found that adsorption of HA on reduced graphene oxide involved π-π interactions (S. Yang et al., 2014).The strong adsorption properties of HA are of particular interest for surface

modification of materials and colloidal technologies. The literature data on the adsorption of HA on inorganic and organic materials and dispersion of different materials indicate that HA is a promising dispersant for application in EPD technology. The goal of this investigation was the application of HA as a charging and dispersing agent for EPD. An important finding was the possibility of the deposition of HA films by anodic EPD. The film forming properties of HA offered additional benefits for the EPD of various materials. HA was used as an anionic dispersant and film forming agent for the EPD of materials such as halloysite and huntite. The films, prepared by EPD are promising for various applications, based on the catalytic, flame retardant and other properties of the deposited materials.

EPD of pure HA films was performed from HA solutions in water or water-ethanol solvent (50% water). The HA concentration in the solutions was in the range of 0.1–1.0 g/L. The use of water–ethanol solvent offered the advantages of reduced gas evolution at the electrodes. Huntite and halloysite were dispersed in the HA solutions in a mixed ethanol-water solvent using ultrasonication during 30 min. The obtained suspensions were used for EPD with a deposition DC voltage of 100 V. QCM deposition DC voltage was 3–5 V.

EPD from HA solutions allowed the fabrication of anodic films. Figure 45 shows deposition yield data, obtained by the QCM method, at different conditions. EPD was performed from HA solutions in water or mixed water–ethanol solvent. The deposit mass increased with increasing deposition time, indicating continuous film growth. The

deposition rate decreased with increasing deposition time due to the increase in the voltage drop in the growing insulating film and corresponding decrease in the voltage drop in the solution (D.D. Sun & Lee, 2012).The deposition yield in the aqueous solutions slightly decreased at deposition times above 200s at a deposition voltage of 3V. Such reduction can result from enhanced gas evolution in aqueous solutions and low adhesion of the deposits at low deposition voltages. It is known that a certain value of electric field is necessary in order to allow the deposited material to bond to the substrate(Zhitomirsky & Gal-Or, 1997). The deposition yield increased with increasing voltage (Figure 45).

Figure 46 shows deposit mass versus HA concentration in the suspension at a constant deposition time. The slope of the curve increased with increasing HA concentration in the range of 0–0.4 g/L. The deviation from the linear Hamaker equation (Biest & Vandeperre, 1999), describing the deposition yield in the EPD process, was also observed in other investigations (Biesheuvel & Verweij, 1999; Pang, Casagrande, & Zhitomirsky, 2009). The non-linear increase in the deposition yield was attributed to the shifting of the deposit-suspension interface during the film growth (Pang et al., 2009). At HA concentrations above 0.5 g/L the slope of the dependence decreased due to the increase in deposit thickness and voltage drop in the deposited material and corresponding decrease in voltage drop in the HA solution.

The mechanism of HA deposition was suggested using literature data on the pH dependence of HA solubility. It was found (H. Kipton, J. Powell, 1992) that HA

solubility decreases with decreasing pH and HA precipitation was observed at pH < 3. The electric charge of HA in the neutral solutions is related to the deprotonated carboxylic groups. The protonation of the carboxylic groups at low pH resulted in the HA precipitation. It is suggested that electrophoresis of the anionic HA molecules resulted in their accumulation at the anode surface. The electrochemical decomposition of the water molecules at the anode as seen previously in equation 5-1 resulted in a local pH decrease. The protonation of the carboxylic groups at the anode surface and charge neutralization promoted precipitation of insoluble HA according to equation 5-2.

$$-COO^- + H^+ \rightarrow -COOH \qquad \text{Eq. 5-2}$$

It is suggested that π-π interactions of the HA molecules, depletion forces and other interactions at the electrode surface (Zhitomirsky, 2002) promoted deposit formation. The deposition yield data, presented in Figure 45 and Figure 46, confirmed that the deposition mechanism and kinetics are based on the electrophoretic transport, as indicated by the increase in the deposition yield with time and concentration of the anionic HA species in the solutions.

Figure 47 shows a typical SEM image of a HA film prepared by EPD. The EPD method allowed for the formation of continuous, crack free and adherent films with thickness of 1–2 μm. The films adhered well to the substrates and showed low porosity.

The film forming properties of HA, coupled with strong adsorption on different materials and electric charge make HA a very promising additive for the EPD of different materials. It was found that HA adsorption on different materials such as TiO_2 and MnO_2 oxides, halloysite and huntite minerals, Ni and Pd metals, SiC and MWCNT allowed for the fabrication of stable suspensions. The adsorption of HA on the oxides, minerals, metals and SiC was attributed to chelation of metal atoms of the particle surface with catecholate, salicylate or other ligands of HA. The relatively large size and anionic properties of HA allowed for electrosteric stabilization. The adsorbed HA imparted a negative charge to the particles and allowed for their electrophoretic motion toward the electrode surface and deposition. The charged particles were dispersed and deposited on the anode surface by EPD. The formation of anodic deposits provided additional evidence of HA adsorption on particles.

It is important to note that EPD requires the use of a binder, which allows for the fabrication of adherent and crack free films. The bath formulations for EPD usually include dispersants and binders (Zhitomirsky & Petric, 2000, 2004). The charged particles, containing an adsorbed charged dispersant and a binder provide electrophoretic transport of the binder macromolecules to the electrode surface. Difficulties are related to the competitive adsorption of the binder and dispersant on the particle surface (Zhitomirsky & Petric, 2000, 2004). Such difficulties can be avoided using HA as a binder and charged dispersant for EPD. The SEM images of halloysite films (Figure 48) showed relatively dense microstructure with low porosity. The films contained hollow halloysite nanotubes. The SEM images of huntite films (Figure 48) showed a relatively

dense continuous microstructure, containing huntite platelets. The size of the pores in the halloysite and huntite films was on the nanometric scale and can mainly be attributed to the particle packing.

Huntite and halloysite are advanced flame retardant additives for polymer coatings and polymer based composites (L.A. Hollingbery & Hull, 2010; Li et al., 2015). Of special interest are applications of hollow halloysite nanotubes for controlled drug delivery and corrosion protection of metals (Abdullayeva & Lvov, 2010; Hui Lia, Zhua, Zhoub, & Zhong, 2015). Therefore, the films prepared by EPD using HA can be used for other applications, based on the functional properties of the deposited materials.

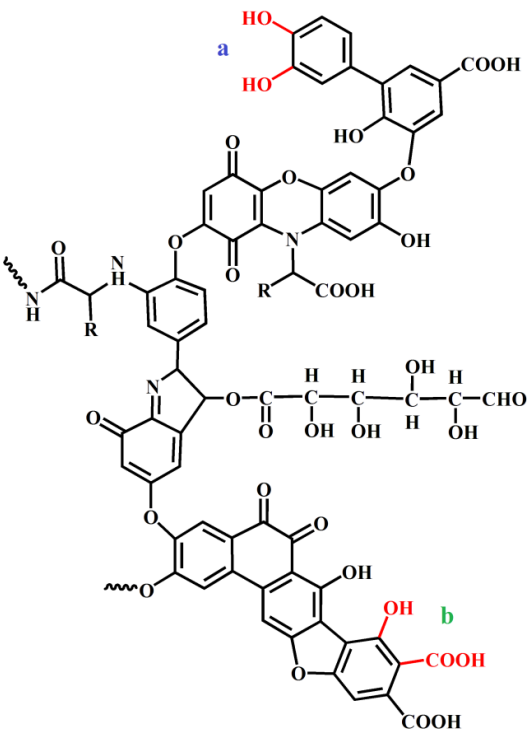

Figure 44: Schematic of chemical structure of HA (a—catechol ligand, b—salicylate ligand).

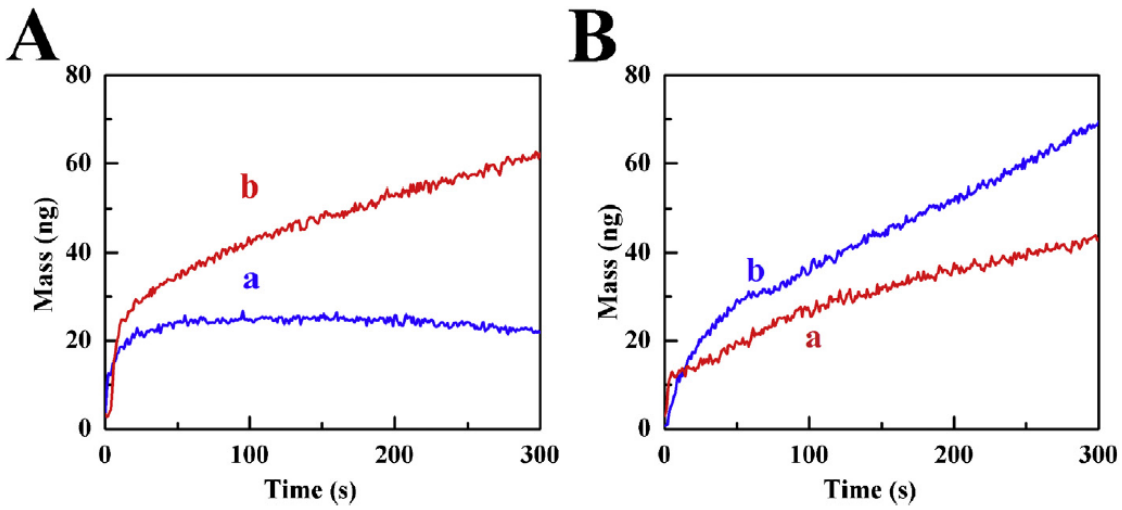

Figure 45: Deposit mass versus time obtained using QCM from 0.1 g/L HA solutions in (A) water and (B) mixed ethanol–water (50% water) solvent at deposition voltages of (a)3 V and (b) 5 V.

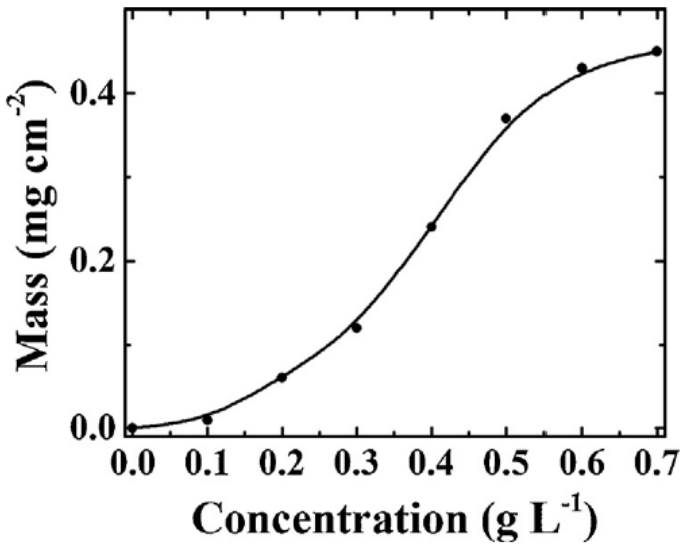

Figure 46: Deposit mass versus HA concentration in a mixed water-ethanol solvent (50%water) at a deposition voltage of 100 V and deposition time of 5 min.

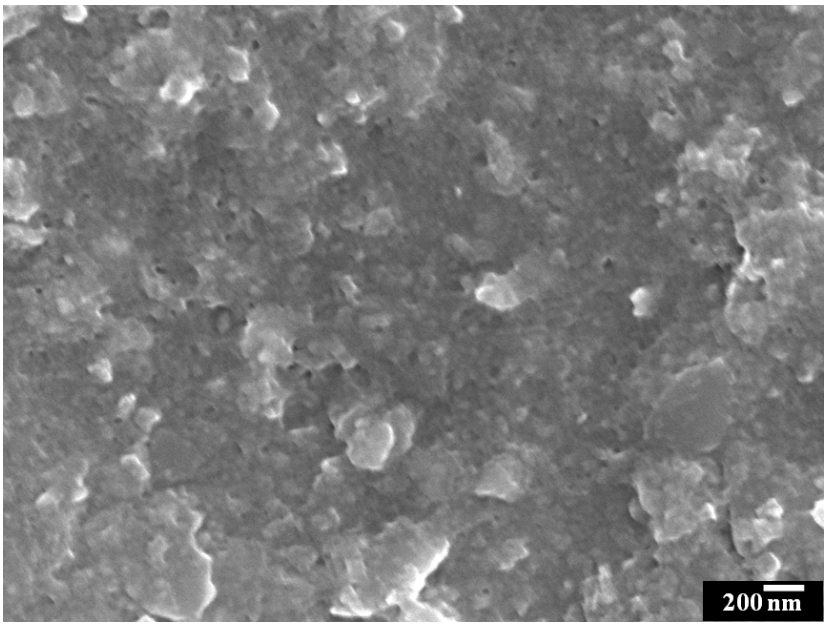

Figure 47: SEM image of HA film prepared from 1 g/L HA solution in a mixed water–ethanol solvent (50% water).

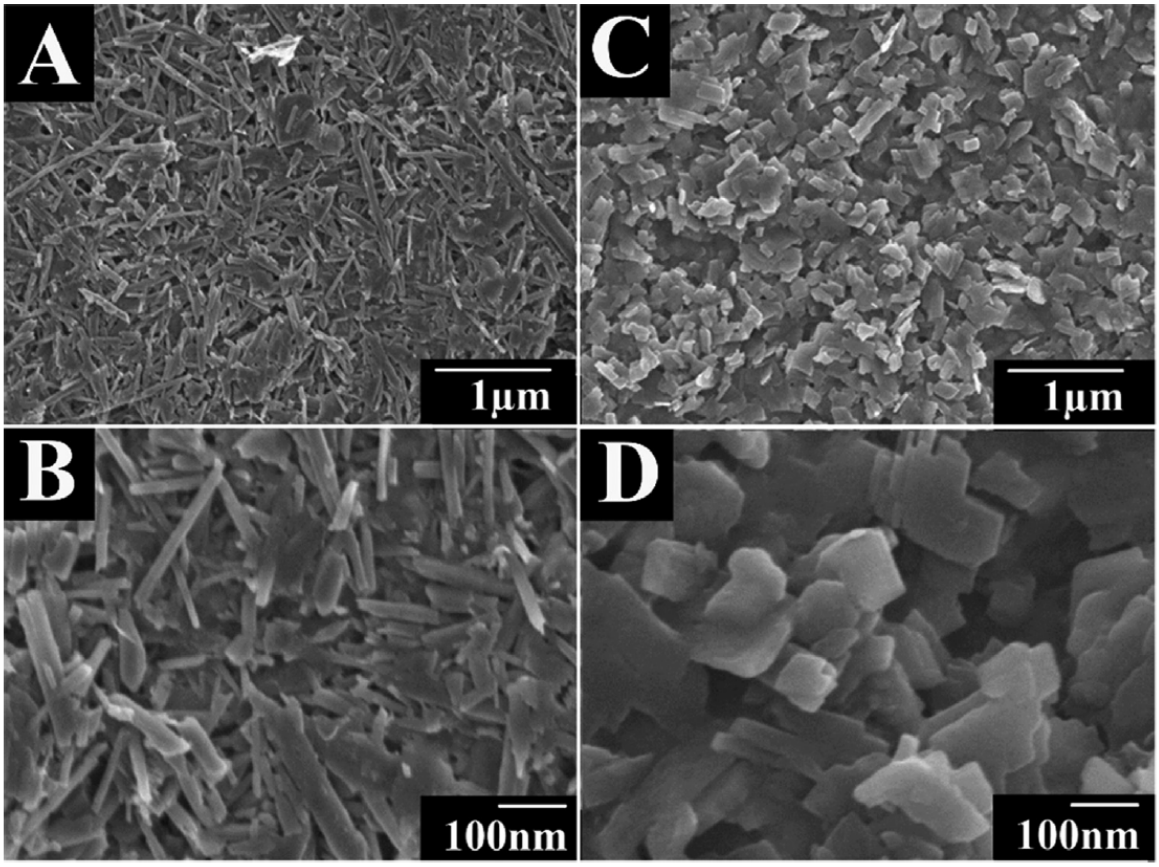

Figure 48: SEM images at different magnifications of deposits, prepared from 0.5 g/L HA solutions in a mixed water–ethanol solvent (50% water), containing 4 g/L (A, B) halloysite nanotubes and (C, D) huntite platelets.

5.2.4 Electrophoretic Deposition of Huntite Using New Dispersants from the Phosphonate Family

Figure 49(A-C) shows chemical structures of phosphonate molecules used in this investigation. The structures of 3-phosphonopropionic acid (3PHA) (Figure 49A), 16-phosphonohexadecanoic acid (16PHA) (Figure 49B), and octadecylphosphonic acid (octaPHA) (Figure 49C) contain phosphonate groups bonded to the hydrocarbon chains. 3PHA has a smaller hydrocarbon chain, consisting of 3 carbon atoms, while 16PHA

contains a much longer 16 carbon atom chain. Both of these materials contain a carboxylic group at the end of the chain. It was suggested that the comparison of the data for 3PHA and 16PHA molecules will provide an insight into the influence of the molecular size on huntite particle dispersion and their EPD. The chemical structure of octaPHA contains 19 carbon atoms; however it doesn't include a carboxylic group. By comparing 16PHA and octaPHA, an investigation was conducted for the effect that the presence of a carboxylic group will have for the deposition of huntite particles. It is known (Pujari, Scheres, Marcelis, & Zuilhof, 2014) that phosphonate groups can interact with metal atoms on the particle surface and form chelating, bidentate or three dentate bonding (Figure 49D). Such bonding can result in adsorption of the molecules on the particle surface. On the other hand, carboxylic groups of 3PHA and 16PHA can also be involved in the adsorption on particle surface (Ata, Liu, et al., 2014). Different adsorption mechanisms of carboxylate adsorption were discussed in the literature. The anionic charge of the molecules can be attributed to dissociated sulfonate or carboxylic groups. However, the dissociation of the molecules results in the release of H^+. Therefore, a competitive adsorption of the anionic molecules and H^+ on the particle surface can be expected.

It was found that huntite particles in the solution of 0-0.5 g/L 3PHA, 16 PHA and octaPHA were positively charged due to preferred adsorption of H^+. As a result, cathodic deposits were obtained from the suspensions. The 4 g/L huntite suspensions in ethanol, containing different amounts of the phosphonates in the range of 0-0.5 g/L were

ultrasonically agitated for 10 min and then EPD was performed at a deposition voltage of 20V for 1-8 min.

The mass of deposited material increased with longer deposition times with 3PHA, 16PHA, and octaPHA, results may be observed in Figure 50. Comparing short chain length Figure 50a and long chain length Figure 50b it is evident that the smaller molecule stimulates larger deposition mass. It is suggested that larger dispersant molecules have some steric repulsion effect, preventing coagulation of the particles at the electrode surface and film formation. There is no significant impact on deposition mass from the presence of a carboxylic end group as shown in the comparison of Figure 50b and Figure 50c. Figure 51 displays the SEM images of films that were obtained. Plate like structure of huntite can be clearly discerned from these images fortifying the success of creating a huntite coating facilitated by 3PHA, 16PHA, and octaPHA molecules.

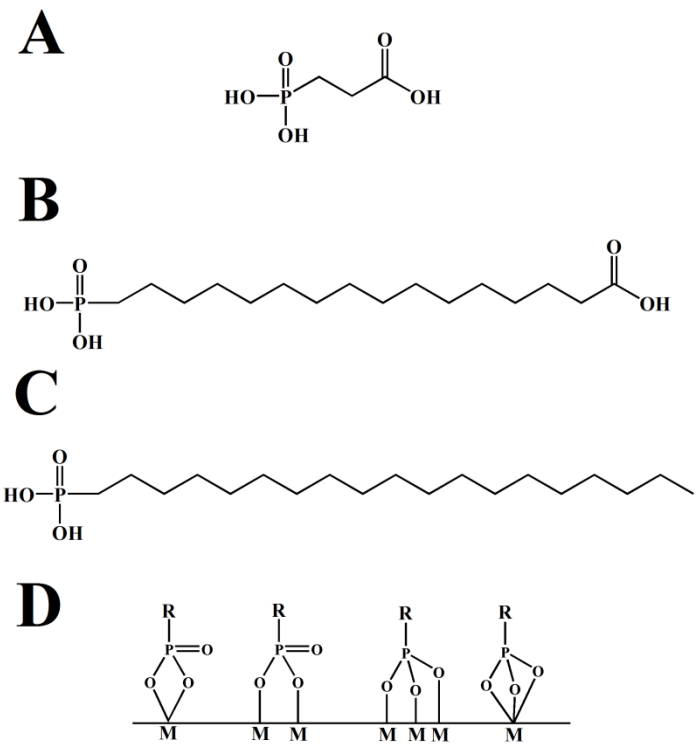

Figure 49: Structure of (A) 3pha, (B)16pha, (C)octapha, (D) representation of one type of adhesion mechanisms

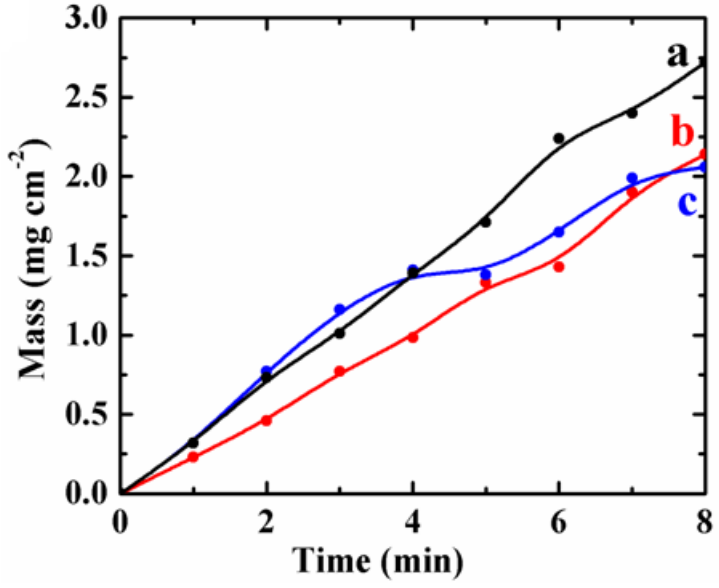

Figure 50: Deposition of huntite with PHA at 20V, mass versus time with concentration of 0.5g/L where (a)3PHA (b)16PHA and (c)octaPHA

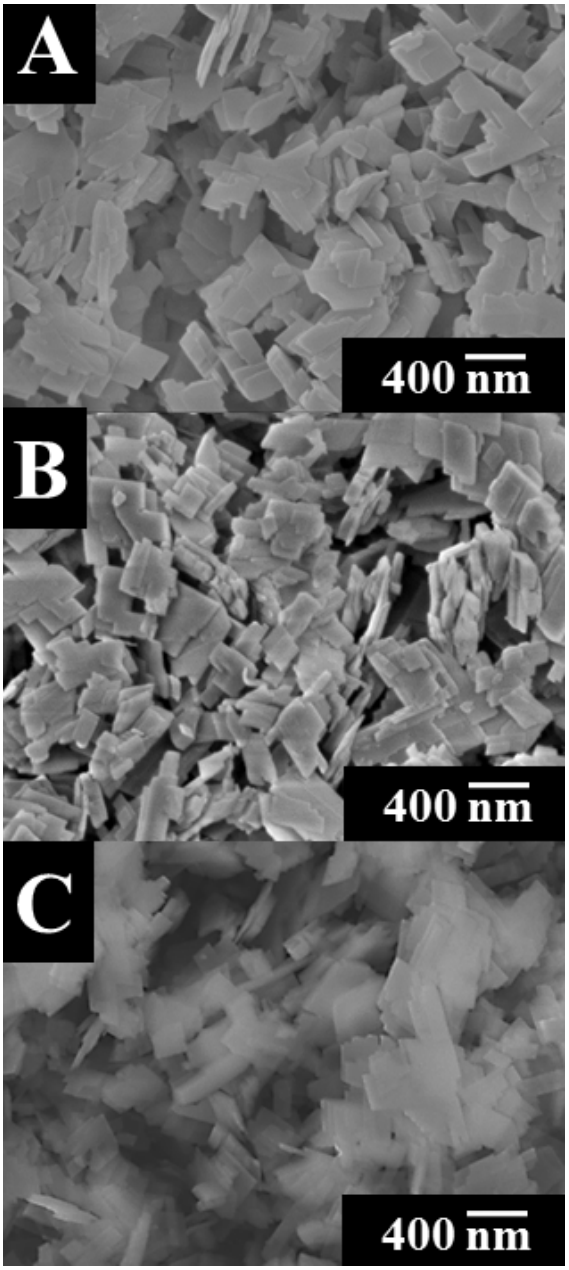

Figure 51: SEM for Huntite with (a)3PHA (b)16PHA (c)octaPHA

5.2.5 Electrophoretic Deposition of Composites, Based on Quaternized Hydroxyethylcellulose Ethoxylate Polymer

Figure 52A shows the chemical structure of quaternized hydroxyethylcellulose ethoxylate (HCE) polymer. HCE is a promising cationic polyelectrolyte for the fabrication of films by cathodic EPD. Thin films of HCE were obtained from 1-5 g/L HCE solutions in a mixed water-ethanol solvent (70% ethanol). The use of a mixed ethanol-water solvent offers advantages of reduced cathodic H_2 evolution and lower currents, compared to pure water solvent. Moreover, HCE showed good adsorption on various materials, such as aluminum hydroxide, AMZH, huntite, and ZnO. The adsorbed HCE provided electrosteric stabilization of the materials and imparted a charge for cathodic EPD.

As a result, cathodic deposits were obtained from the suspensions. The suspensions of aluminum hydroxide, AMZH, huntite, and ZnO with solid contents of 4 g/L were prepared using a mixed solvent, containing 70% ethanol, 30% de-ionized water and 2 g/L HCE. The suspensions were ultrasonically agitated for 10 min. EPD was performed at a deposition voltage of 30V for 1-5 min.

Figure 53 shows typical deposit mass-deposition time dependencies, which indicate continuous increase in the deposit mass with increasing deposition time at a constant voltage. Figure 54 displays the SEM images of the films that were obtained by EPD. The plate like structures are clearly evident in deposits containing AMZH (Figure 54A), and huntite (Figure 54B), proving that coatings contained these FRM materials.

The SEM image of the HCE-$Al(OH)_3$ deposits showed that some ceramic particles formed agglomerates. The films, containing ZnO showed porous structure, the porosity can result from packing of the particles. The results indicated that EPD allows the formation of HCE composites, containing FRM and other functional materials.

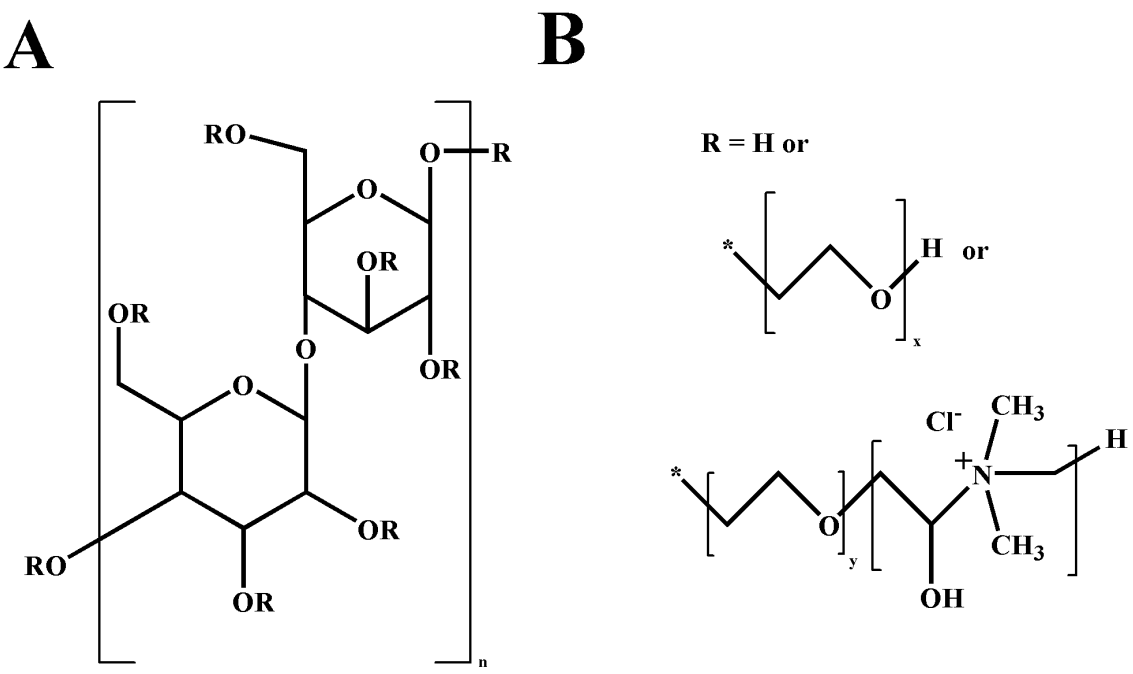

Figure 52: Chemical structure of HCE

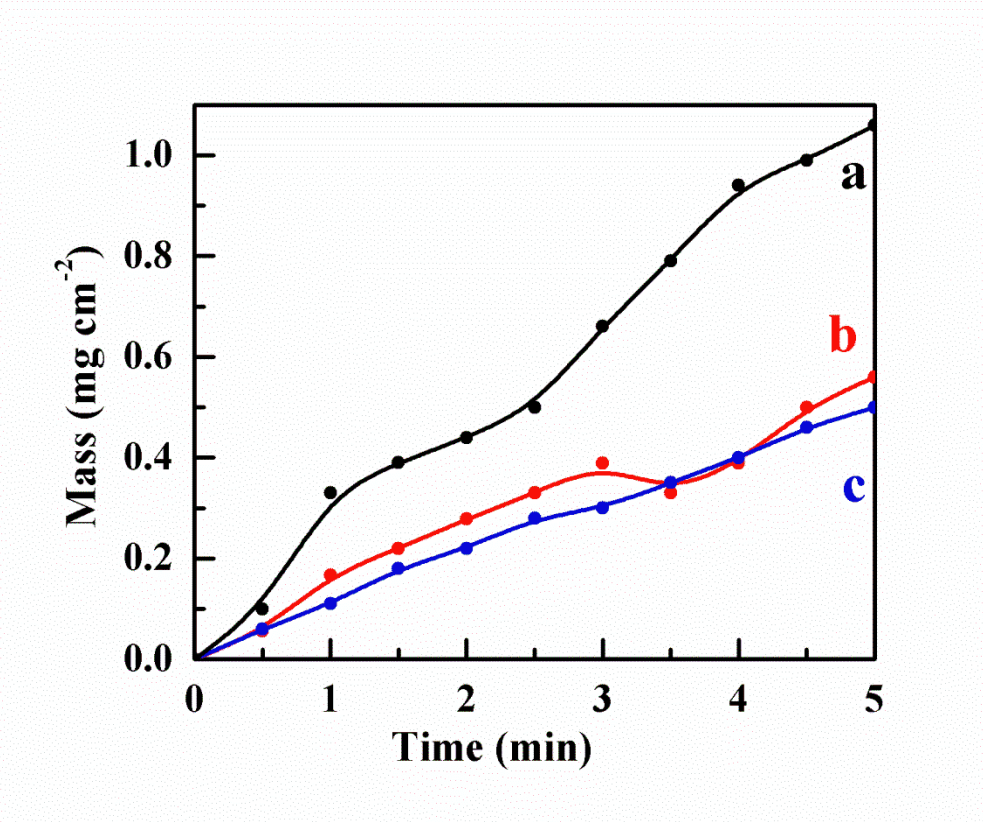

Figure 53: Deposit mass versus deposition time for 0.5g/L HCE solutions at a deposition voltage of 30 V, containing 4g/L of (a)AMZH, (b)huntite (c)$Al(OH)_3$.

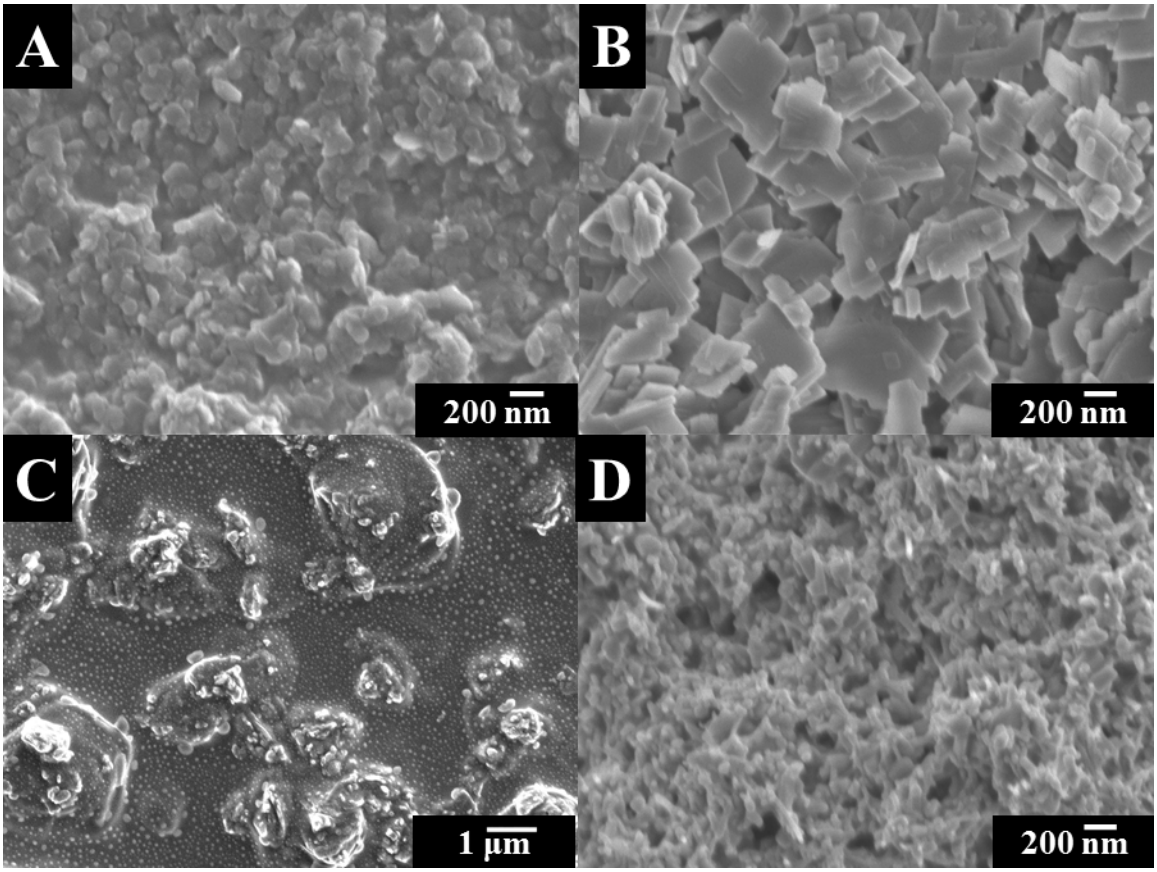

Figure 54: (A-D) SEM images of films, prepared from 0.5g/L HCE solutions, containing 4g/L of (A)AMZH, (B)huntite (C)$Al(OH)_3$ and (D)ZnO at a deposition voltage of 30 V

5.2.6 Surface Modification and Electrophoretic Deposition of Materials Using 2, 2'-Biquinoline-4, 4'-Dicarboxylic Acid

One of the challenges in EPD technology is the development of strategies for the deposition of small functional organic molecules. 2, 2'-Biquinoline-4, 4'-Dicarboxylic Acid (BQCOOH) and its derivatives are important organic molecules for various devices owing to their strong photoluminescence and electroluminescence properties (Liang et al., 2003). The molecules from the BQCOOH family are being investigated for

applications in photosynthesis, light emitting devices and electro-optical displays (Baudin et al., 2002; Yurdakal & Yurdakul, 2007), as well as medicine and corrosion inhibition (Yurdakal & Yurdakul, 2007). The expanding applications of BQCOOH provide motivation to develop new film deposition techniques. The goal of this investigation was the EPD of BQCOOH films and application of BQCOOH for surface modification and EPD of inorganic particles, such as huntite, ZnO and TiO_2. We demonstrated that BQCOOH films can be deposited by anodic EPD from BQCOOH solutions and proposed a deposition mechanism. In another strategy we utilized chelating and film forming properties of BQCOOH for EPD of different materials. The results indicated that EPD is a promising method for the deposition of films, utilizing functional properties of BQCOOH and inorganic materials.

EPD of BQCOOH was performed from 0.1 to 1g/L BQCOOH solutions in ethanol, containing 0.2 – 1 mM NaOH. In order to obtain stable suspensions for EPD, 4g/L ZnO, TiO_2 and huntite were added to the BQCOOH solutions and ultrasonically The EPD voltage was 25V for pure BQCOOH solutions and 45V for ZnO, TiO_2 and huntite suspensions.

The results of our investigation showed a feasibility of controlled EPD of BQCOOH films. Figure 55A indicates that BQCOOH is a polyaromatic molecule, containing two COOH groups. The deprotonation of the COOH ligands in the presence of NaOH resulted in the BQCOOH dissolution. In the EPD process, an electric field provided electrophoretic transport of the deprotonated anionic $BQCOO^-$ toward the

anode surface, where local pH decrease resulted in the charge neutralization and deposition of insoluble BQCOOH as seen in equation 5-3.

$$\mathbf{BQCOO^- + H^+ \rightarrow BQCOOH} \qquad \text{Eq. 5-3}$$

Figure 55 (B-D) shows a microstructure of the BQCOOH films at different magnifications. The SEM images show a flower-like microstructure (Figure 55B). The formation of such microstructure was governed by the kinetics of the nucleation and growth processes. It is suggested that nucleation occurs slowly, whereas the fast deposit growth spreads outwards from the nucleating sites, resulting in the long particles (Figure 55C). The particle assembly can be governed by π-π interactions and hydrogen bonding of the polyaromatic (Figure 55A) BQCOOH molecules. The analysis of the particle microstructure at higher magnification (Figure 55D) indicated that the long particles had nearly polygonal cross sections with a typical aspect ratio of 5-10. The deposition yield increased with increasing deposition time at a constant voltage, indicating a continuous film growth (Figure 56A). Therefore, EPD method can be used for the fabrication of BQCOOH films. It is expected that a similar approach can be used for EPD other molecules from the BQCOOH family. In another strategy, we utilized chelating and film forming properties of BQCOOH for the EPD of different inorganic materials, such as ZnO, TiO_2 and huntite. We explored a new chelating mechanism for the particle-dispersant interactions and adsorption for application in EPD. The dispersant adsorption is of critical importance for EPD, because non-adsorbed ionic dispersant reduces the thickness of the electrical double layer around the colloidal particles and promotes

particle agglomeration. Moreover, non-adsorbed ionic dispersant increases the electrical conductivity of the suspensions, which is detrimental for EPD. It was found that inorganic particles of different materials, such as ZnO, TiO_2 and huntite can be efficiently dispersed and deposited using BQCOOH as a dispersant. The deposition yield increased with increasing deposition time, indicating a continuous film growth (Figure 56B). The SEM images of the deposits (Figure 57A-C) showed plate- like particles of huntite and nanoparticles of ZnO and TiO_2. It is suggested that BQCOOH was adsorbed on the inorganic particles in the suspensions, improved their dispersion and imparted an electric charge for EPD. It is known that BQCOOH and related molecules (Allan, Carson, & Levey, 1995; Baudin et al., 2002; Chowdhury, Ghosh, & Misra, 2000; Leung, Zhong, Yang, Cheng, & Chan, 2012; Poonam, Khatkar, Kumar, Khatkar, & Taxak, 2015; Wills et al., 2013) form chelates with different ions, involving two N atoms of the molecules. A similar chelation mechanism (Figure 57D) can be suggested for the chelation of the metal atoms on the particle surface, which allowed for the BQCOOH adsorption on particles. The deprotonated COO^- ligands imparted a negative charge for the electrosteric stabilization in the bulk of the suspensions and electrophoresis. The pH dependent charge and solubility of the adsorbed $BQCOO^-$ species coupled with film forming properties of BQCOOH were beneficial for the deposition of inorganic particles at the electrode surface. The SEM images presented in Figure 57A-C showed that the deposited films contained inorganic particles. However, the results of FTIR and UV–vis studies indicated that the particles contained adsorbed BQCOOH molecules. Figure 58 compares the FTIR spectra of BQCOOH and inorganic materials, deposited by EPD. The FTIR spectrum of

the BQCOOH contains absorption peaks, which are in agreement with the data provided by the manufacturer and literature data(Yurdakal & Yurdakul, 2007). The FTIR spectra of the inorganic materials showed similar peaks, indicating the incorporation of BQCOOH into the deposit in agreement with the proposed deposition mechanism. The BQCOOH (Baudin et al., 2002; Yurdakal & Yurdakul, 2007) molecules are currently under investigation for optical applications, based on their absorption properties. The UV–vis spectrum of BQCOOH shows absorptions at 208, 260, and 332 nm (Figure 59a). The UV–vis spectra of the deposited inorganic materials (Figure 59b-d) showed similar absorptions and confirmed the incorporation of BQCOOH into the films. The films, prepared by EPD are promising for applications based on functional properties of BQCOOH and co-deposited inorganic materials. BQCOOH represents a new type of charging dispersants with chelating properties for EPD in addition to previously developed chelating dispersants from catechol, salicylic acid and chromotropic acid families (Ata, Liu, et al., 2014). BQCOOH can be used for deposition of FRM materials, such as huntite and other materials and offers advantages related to its film forming and functional properties.

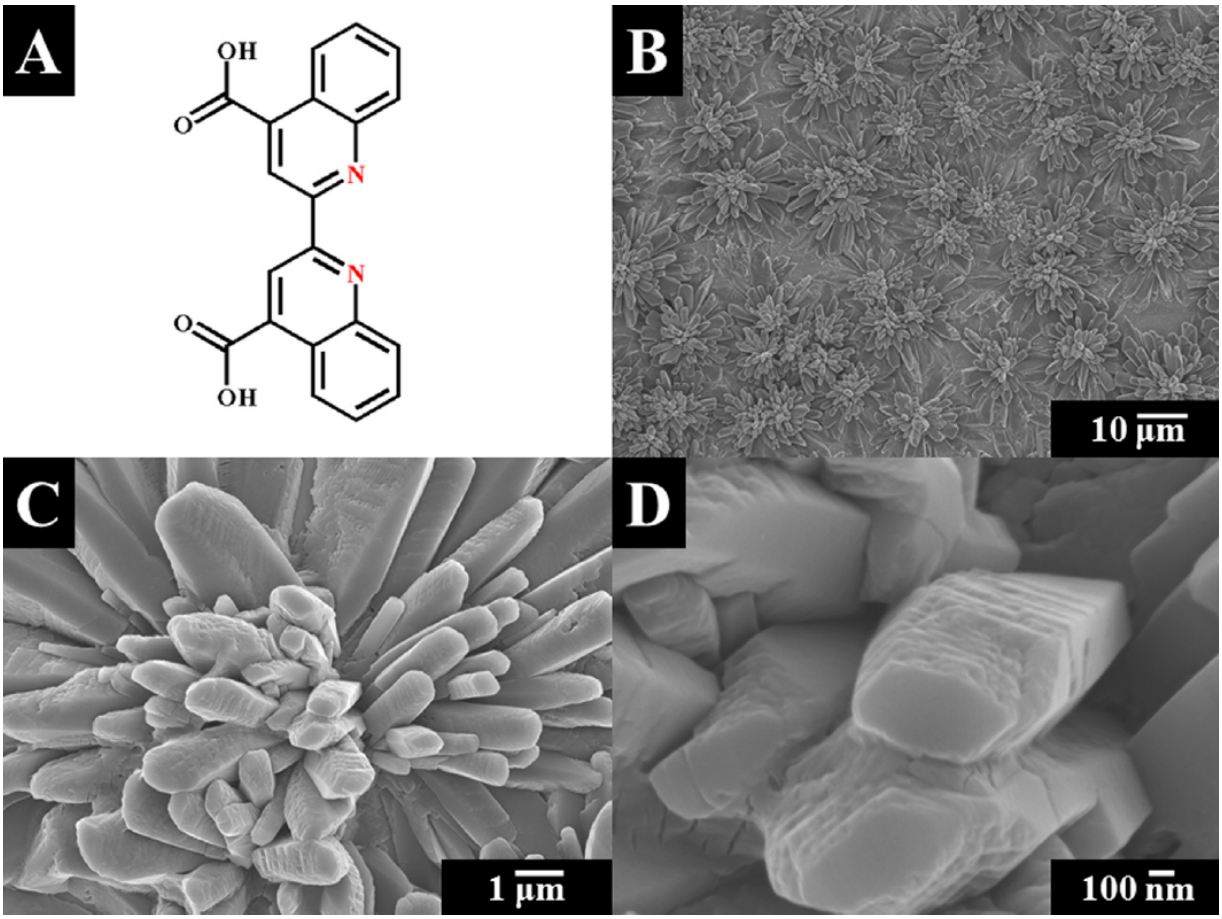

Figure 55: (A) Chemical Structure of BQCOOH and (B-D) SEM images of BQCOOH films, prepared from 0.5 g/L BQCOOH solutions at a deposition voltage of 25 V

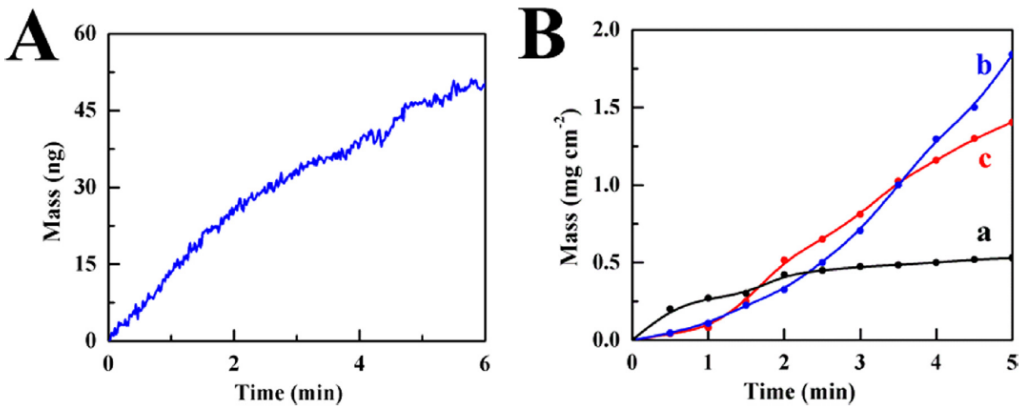

Figure 56: Deposit mass versus deposition time for (A) 0.1g/L BQCOOH solutions at a deposition voltage of 25V, measured by QCM and (B) 0.5g/L BQCOOH solutions, containing 4g/L of (a)ZnO, (b)TiO_2 and (c)huntite at a deposition voltage of 45V.

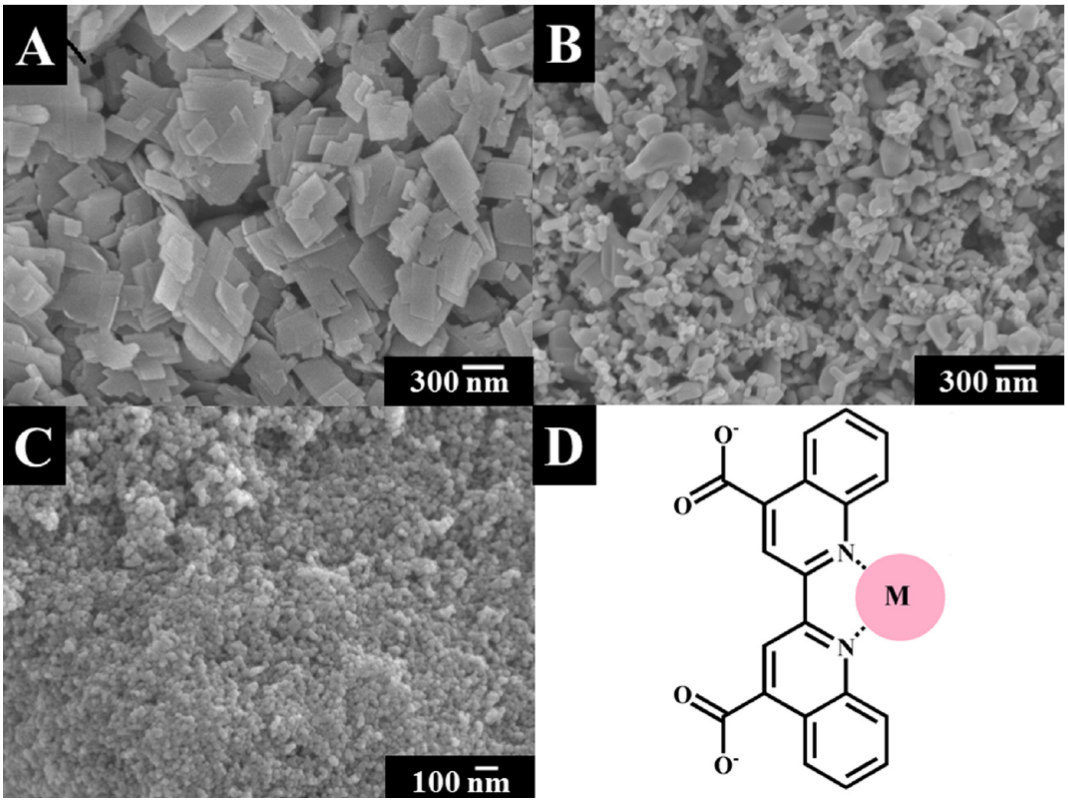

Figure 57: (A-C) SEM images of films, prepared from 0.5g/L BQCOOH solutions, containing 4g/L of (A)huntite, (B)ZnO (C)TiO_2 at a deposition voltage of 45V and (D) complexation of metal atoms on particle surface by BQCOOH.

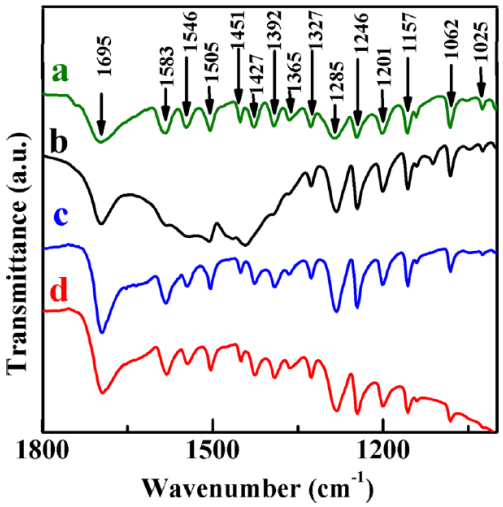

Figure 58: FTIR spectra of the deposits prepared from (a)1 g/L BQCOOH solution at a deposition voltage of 25V and (b-d) 0.5g/L BQCOOH solutions, containing 4 g/L of (b)huntite, (c)ZnO, and (d)TiO_2 at a deposition voltage of 45V.

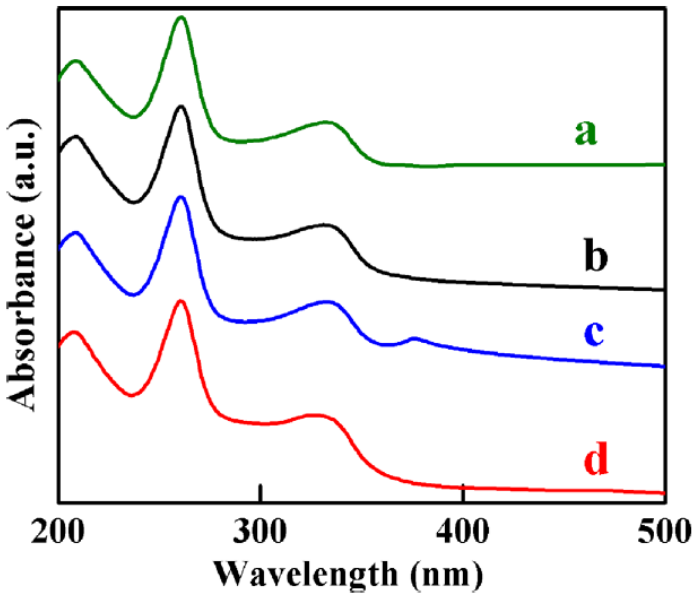

Figure 59: UV–vis spectra of the deposits prepared from (a) 1g/L BQCOOH solution at a deposition voltage of 25V and (b-d) 0.5g/L BQCOOH solutions, containing 4 g L of (b)huntite, (c)ZnO, and (d)TiO_2 at a deposition voltage of 45V.

CHAPTER 6 CONCLUSIONS

A large amount of candidate inorganic materials where investigated for potential applications as FRM. Magnesium sulphate heptahydrate, magnesium carbonate hydroxide pentahydrate, sodium metasilicate pentahydrate, alumino silicates yttrium aluminum hydroxide composite, $Y(OH)_3$, aluminum zirconium magnesium hydroxide, huntite, aluminum hydroxide, hydromagnesite, and hydrotalcite were identified as promising materials. Through TGA/DTA investigations materials had at least a 34% mass loss related to the release of carbon dioxide, water, or both. This allowed the materials to dilute the fuel available at the surface of the host materials, preventing the critical combustion concentration from being reached. The reactions involving dehydration and release of carbon dioxide resulted in strong endothermic reactions; materials were able to absorb heat from their surrounding when heated. Chosen FRM candidates were investigated for EPD using different dispersing and charging agents. Successful candidates for which effective dispersing agents were identified and formed coatings using EPD technique were aluminum hydroxide, huntite, halloysite, and Aluminum zirconium magnesium hydroxide.

Aluminum zirconium magnesium hydroxide offers advantages for FRM applications due to a higher mass loss of 44.2%, compared to aluminum and magnesium hydroxides. The memory properties of aluminum zirconium magnesium hydroxide pave the way for novel applications in composites, fabricated by techniques, involving thermal processing. The results of XRD, TGA and DTA investigations showed that the structure

and composition of aluminum zirconium magnesium hydroxide can be reconstructed after dehydration at 500^{o}C. EPD method has been utilized for the fabrication of aluminum zirconium magnesium hydroxide coatings at controlled deposition rate. The results of the deposition yield measurements, coupled with the UV–vis and FTIR data, confirmed the deposition mechanism, based on the use of $ATNH_4$ as a dispersing, charging, binding and film forming agent.

EPD method succeeded in manufacturing of composite PVBM– aluminum zirconium magnesium hydroxide and chitosan– aluminum zirconium magnesium hydroxide coatings. The charging mechanism of aluminum zirconium magnesium hydroxide is based on Celestine blue dye adsorption, which involved catecholate-type outer sphere bonding. The mechanism of composite coating formation involved electrophoresis of protonated polymers and charged aluminum zirconium magnesium hydroxide, pH increase at the cathode surface, related to electrochemical decomposition of water, deprotonation, and discharge of polymers the at high pH conditions at the electrode. The composite coatings were formed, containing aluminum zirconium magnesium hydroxide in PVBM or chitosan matrix, which showed flame-retardant and protective properties.

Thin films of humic acid were deposited by anodic EPD from aqueous or water–ethanol solutions. The deposition rate can be varied by variation of deposition voltage or humic acid concentration in the solutions. The deposition mechanism is based on the electrophoresis of anionic humic acid species, local pH decrease at the anode surface and charge neutralization, followed by the precipitation of insoluble humic acid molecules

and film formation. humic acid was used as a dispersing, charging and film forming agent for the EPD of materials of different types, such as mineral particles of halloysite nanotubes and huntite platelets. Good dispersion properties of humic acid are related to remarkable humic acid adsorption on various materials, which involved different adsorption mechanisms. The obtained films can be used for various applications based on the functional properties of the deposited materials, such as catalytic, or flame retardant.

Phosphonate molecules 3PHA, 16PHA, and octaPHA were used for successful dispersion and EPD of huntite particles. Charge of huntite particles was positive due to preferred adsorption of H^+ provided by dissociation of sulfonate and carboxylic groups in phosphonate molecules. Shorter chain length of 3PHA resulted in greater deposition mass due to a steric repulsion effect of longer chained 16PHA and octaPHA. The presence of carboxylic end groups had no effect on deposition mass. SEM images show acceptable films of plate like huntite particles confirming successful synthesis of FRM coating.

Cathodic EPD was successful for synthesis of composite HCE films containing one of: aluminum hydroxide, huntite, aluminum zirconium magnesium hydroxide, or ZnO. HCE solution was prepared in water ethanol solvent to reduce cathodic H_2 evolution and lower currents in comparison to pure water solvent. HCE adsorbed onto particles, imparted a cathodic charge and provided electrosteric stabilization allowing successful EPD. The film thickness can be controlled by varying the deposition time. SEM images show successful deposition of inorganic ceramic particles with adsorbed HCE molecules confirming successful formation of FRM coatings.

Successful deposition was achieved by the EPD of BQCOOH films from BQCOOH solutions. The flower-like film microstructure is governed by the electrode reactions, nucleation and growth rates and interactions of the BQCOOH molecules. BQCOOH can be used as an efficient film-forming dispersant for the EPD of inorganic materials, such as huntite, ZnO and TiO_2. The use of BQCOOH as a dispersant offers advantages of strong adsorption on inorganic particles, attributed to chelating properties of BQCOOH ligands. The results of this investigation pave the way to the development of advanced chelating dispersants from the BQCOOH family of molecules and can be used for the EPD of films, combining functional properties of BQCOOH and inorganic materials.

REFERENCES

Abdullayeva, E., & Lvov, Y. (2010). Clay nanotubes for corrosion inhibitor encapsulation: release control with end stoppers. *Journal of Materials Chemistry*, *20*(32), 6681–6687. http://doi.org/10.1039/C0JM00810A

Allan, J. R., Carson, B. R., & Levey, S. (1995). A study of the performance of some first row transition metal complexes of 2,2′-biquinoline as colourants for poly(vinyl chloride) and polyethylene. *European Polymer Journal*, *31*(5), 445–448. http://doi.org/10.1016/0014-3057(94)00199-5

Arias, M., Barral, M. T., & Mejuto, J. C. (2002). Enhancement of copper and cadmium adsorption on kaolin by the presence of humic acids. *Chemosphere*, *48*(10), 1081–1088. http://doi.org/10.1016/S0045-6535(02)00169-8

Ata, M. S., Liu, Y., & Zhitomirsky, I. (2014). A review of new methods of surface chemical modification, dispersion and electrophoretic deposition of metal oxide particles. *RSC Advances*, *4*(43), 22716. http://doi.org/10.1039/c4ra02218a

Ata, M. S., Zhua, G.-Z., Botton, G. A., & Zhitomirsky, I. (2014). Electrophoretic deposition of manganese dioxide films using new dispersing agents. *Advances in Applied Ceramics: Structural, Functional and Bioceramics*, *113*(1), 22–27. http://doi.org/10.1179/1743676113Y.0000000106

Basu, R. N., Randall, C. A., & Mayo, M. J. (2001). Fabrication of Dense Zirconia Electrolyte Films for Tubular Solid Oxide Fuel Cells by Electrophoretic Deposition. *Journal of the American Ceramic Society*, *84*(1), 33–40. http://doi.org/10.1111/j.1151-2916.2001.tb00604.x

Baudin, H. B., Davidsson, J., Serroni, S., Juris, A., Balzani, V., Campagna, S., & Hammarström, L. (2002). Ultrafast Energy Transfer in Binuclear Ruthenium−Osmium Complexes as Models for Light-harvesting Antennas. *J. Phys. Chem. A*, *106*(17), 4312–4319. http://doi.org/10.1021/jp012770i

Besra, L., & Liu, M. (2007). A review on fundamentals and applications of electrophoretic deposition (EPD). *Progress in Materials Science*, *52*(1), 1–61. http://doi.org/10.1016/j.pmatsci.2006.07.001

Biesheuvel, P. M., & Verweij, H. (1999). Theory of cast formation in electrophoretic deposition. *Journal of the American Ceramic Society*, *82*(6), 1451–1455.

Biest, O. O. Van der, & Vandeperre, L. J. (1999). ELECTROPHORETIC DEPOSITION OF MATERIALS. *Materials Research*, *29*(1), 327–352. http://doi.org/10.1146/annurev.matsci.29.1.327

Blees, M. H. (2002). Foundations of Colloid Science. *Colloids and Surfaces A: Physicochemical and Engineering Aspects*, *210*(1), 125. http://doi.org/10.1016/S0927-7757(02)00170-X

Boccaccini, A. R., Kaya, C., & Chawla, K. K. (2001). Use of electrophoretic deposition in the processing of fibre reinforced ceramic and glass matrix composites: A review. *Composites - Part A: Applied Science and Manufacturing*, *32*(8), 997–1006. http://doi.org/10.1016/S1359-835X(00)00168-8

Bordeepong, S., Bhongsuwan, D., Pungrassami, T., & Bhongsuwan, T. (2011). Characterization of halloysite from thung yai district, Nakhon Si Thammarat Province, in Southern Thailand. *Songklanakarin Journal of Science and Technology*, *33*(5), 599–607.

Bras, M. Le, Bourbigot, S., Duquesne, S., Jama, C., & Wilkie, C. (2005). *Fire Retardancy of Polymers : New Applications of Mineral Fillers* (1st ed.). Royal Society of Chemistry. http://doi.org/10.1039/9781847552396

Camino, C., & Costa, L. (1988). Performance and mechanism of fire retardants in polymers. *Polymer Degradation and Stability*, *20*(3-4), 271–294.

Chen, L., & Wang, Y. Z. (2010). A review on flame retardant technology in China. Part I: Development of flame retardants. *Polymers for Advanced Technologies*, *21*(1), 1–26. http://doi.org/10.1002/pat.1550

Chowdhury, J., Ghosh, M., & Misra, T. N. (2000). Surface enhanced Raman scattering of 2,2′ biquinoline adsorbed on colloidal silver particles. *Spectrochimica Acta Part A: Molecular and Biomolecular Spectroscopy*, *56*(11), 2107–2115. http://doi.org/10.1016/S1386-1425(00)00263-8

Corni, I., Ryan, M. P., & Boccaccini, A. R. (2008). Electrophoretic deposition: From traditional ceramics to nanotechnology. *Journal of the European Ceramic Society*, *28*(7), 1353–1367. http://doi.org/10.1016/j.jeurceramsoc.2007.12.011

Darnerud, P. (2003). Toxic effects of brominated flame retardants in man and in wildlife. *Environment Internaional*, *29*(6), 841–853. http://doi.org/doi:10.1016/S0160-4120(03)00107-7

Deakin, M. R., & Buttry, D. A. (1989). Electrochemical applications of the quartz crystal microbalance. *Analytical Chemistry*, *61*(20), 1147A–1154A. http://doi.org/10.1021/ac00195a001

Deen, I., Pang, X., & Zhitomirsky, I. (2012). Electrophoretic Deposition of Composite Chitosan-Halloysite Nanotube-Hydroxyapatite Films. *Colloids and Surfaces A: Physicochemical and Engineering Aspects*, *410*, 38–44. http://doi.org/10.1016/j.colsurfa.2012.06.011

DiGangi, J. (2012). Public Interest Guide to Toxic Flame Retardant Chemicals. Retrieved January 1, 2016, from ipen.org/pdfs/ipen_flame_retardants_2012_06.pdf

DiNenno, P. J. (2008). *SFPE Handbook of Fire Protection Engineering* (4th Editio). Quincy, MA: National Fire Protection Association.

Dobson, K. D., & McQuillan, A. J. (2000). In situ infrared spectroscopic analysis of the adsorption of aromatic carboxylic acids to TiO2, ZrO2, Al2 O3, and Ta2O5 from aqueous solutions. *Spectrochimica Acta Part A: Molecular and Biomolecular Spectroscopy*, *56*(3), 557–565. http://doi.org/10.1016/S1386-1425(99)00154-7

Eita, M. (2011). In situ study of the adsorption of humic acid on the surface of aluminium oxide by QCM-D reveals novel features. *Soft Matter*, *7*(2), 709–715. http://doi.org/10.1039/C0SM00648C

Ellyn M. Murphy, Zachara, J. M., & Smith, S. C. (1990). Influence of mineral-bound humic substances on the sorption of hydrophobic organic compounds. *Environ. Sci. Technol*, *24*(10), 1507–1516. http://doi.org/10.1021/es00080a009

Felix, C., Jao, T.-C., Pasupathi, S., Linkov, V. M., & Pollet, B. G. (2014). Fabrication of gas diffusion electrodes via electrophoretic deposition for high temperature polymer

electrolyte membrane fuel cells. *Journal of Power Sources*, *258*, 238–245. http://doi.org/10.1016/j.jpowsour.2014.02.050

Ferrari, B., & Moreno, R. (1996). The conductivity of aqueous Al2O3 slips for electrophoretic deposition. *Materials Letters*, *28*(4-6), 353–355. http://doi.org/10.1016/0167-577X(96)00075-4

Gasser, M. S., Mohsen, H. T., & Aly, H. F. (2008). Humic acid adsorption onto Mg/Fe layered double hydroxide. *Colloids and Surfaces A: Physicochemical and Engineering Aspects*, *331*(3), 195–201. http://doi.org/10.1016/j.colsurfa.2008.08.002

George, A. M., Mishra, N. C., Nagar, M. S., & Jayadevan, N. C. (1996). Formation of Yag From Coprecipitated Yttrium Aluminuim Hydroxides. *Journal of Thermal Analysis*, *47*, 1701–1708.

González, M. A., Pavlovic, I., Rojas-Delgadob, R., & Barriga, C. (2014). Removal of Cu2+, Pb2+ and Cd2+ by layered double hydroxide–humate hybrid. Sorbate and sorbent comparative studies. *Chemical Engineering Journal*, *254*(1), 605–611. http://doi.org/10.1016/j.cej.2014.05.132

Green, J. (1996). Mechanisms for Flame Retardancy and Smoke suppression -A Review. *Journal of Fire Sciences*, *14*(6), 426–442. http://doi.org/10.1177/073490419601400602

H. Kipton, J. Powell, R. M. T. (1992). Solubility and fractionation of humic acid; effect of pH and ionic medium. *Analytica Chimica Acta*, *267*(1), 47–54. http://doi.org/10.1016/0003-2670(92)85005-Q

Haynes, H. (2015). *Fire loss in the United States during 2014*.

Hiemenz, P. C., & Rajagopalan, R. (1997). *Principles of colloid and surface chemistry*. *Marcel Dekker*. http://doi.org/10.1016/0021-9797(79)90045-6

Hollingbery, L. A. (2010). The Thermal Decomposition of Huntite and Hydromagnesite - A Review, *509*, 1–11. http://doi.org/doi:10.1016/j.tca.2010.06.012

Hollingbery, L. A., & Hull, T. R. (2010). The fire retardant behaviour of huntite and hydromagnesite – A review. *Polymer Degradation and Stability*, *95*(12), 2213–2225. http://doi.org/10.1016/j.polymdegradstab.2010.08.019

Horrocks, a. R., Kandola, B. K., Davies, P. J., Zhang, S., & Padbury, S. a. (2005). Developments in flame retardant textiles - A review. *Polymer Degradation and Stability*, *88*(1), 3–12. http://doi.org/10.1016/j.polymdegradstab.2003.10.024

Hui Lia, Zhua, X., Zhoub, H., & Zhong, S. (2015). Functionalization of halloysite nanotubes by enlargement and hydrophobicity for sustained release of analgesic. *Colloids and Surfaces A: Physicochemical and Engineering Aspects*, *487*(1), 154–

161. http://doi.org/10.1016/j.colsurfa.2015.09.062

Jankovic, I. ., Saponic, Z. V., & Comor, M. I. (2009). Surface Modification of Colloidal TiO2 Nanoparticles with Bidentate Benzene Derivatives. *The Journal of Physical Chemistry C*, *113*(29), 12645–12652. http://doi.org/10.1021/jp9013338

Janot, N., Reiller, P. E., Zheng, X., Croué, J.-P., & Benedetti, M. F. (2012). Characterization of humic acid reactivity modifications due to adsorption onto α-Al2O3. *Water Research*, *46*(3), 731–740. http://doi.org/10.1016/j.watres.2011.11.042

Johnson, S. L., Guggenheim, S., & Groos, A. F. K. V. A. N. (1990). Thermal stability of Halloysite by High Pressure Differntial Thermal Analysis. *Clays and Clay Minerals*, *38*(5), 477–484.

Jones, D. A. (1996). *Principles and Prevention of Corrosion*. (B. Stenquist, Ed.) (2nd ed.). New Jersey: Prentice-Hall,Inc.

Jones, M. N., & Bryan, N. D. (1998). Colloidal properties of humic substances. *Advances in Colloid and Interface Science*, *78*(1), 1–48. http://doi.org/10.1016/S0001-8686(98)00058-X

Karthikeyan, K. ., & Chorover, J. (2002). Humic acid complexation of basic and neutral polycyclic aromatic compounds. *Chemosphere*, *48*(9), 955–964. http://doi.org/10.1016/S0045-6535(02)00186-8

Laskowski JS, P. R. (1992). Dispersions Stability and Dispersing Agents. *Colloid Chemistry in Mineral Processing*, *12*, 115–171. http://doi.org/doi:10.1016/B978-0-444-88284-4.50009-3

Lefèvre, G., & Jolivet, A. (2009). Calculation of Hamaker constants applied to the deposition of metallic oxide particles at high temperature. In H. Muller-Steinhagen, M. . Malayeri, & A. P. Watkinson (Eds.), *Proceedings of International Conference on Heat Exchanger Fouling an Cleaning VIII* (pp. 120–124). Schladming, Austria.

Leung, C.-H., Zhong, H.-J., Yang, H., Cheng, Z., & Chan, D. S.-H. (2012). A Metal-Based Inhibitor of Tumor Necrosis Factor-α. *Angewandte Chemie International Edition*, *51*(36), 9010–9014. http://doi.org/10.1002/anie.201202937

Levan, S. (1984). *Chemistry of Fire Retardancy*. *Chemistry of Solid Wood* (R.M.Rowell). Washington,DC: American Chemical Society. http://doi.org/10.1021/ba-1984-0207.ch014

Li, L., Wu, Z., Jiang, S., Zhang, S., Lu, S., Chen, W., … Zhu, M. (2015). Effect of halloysite nanotubes on thermal and flame retardant properties of polyamide 6/melamine cyanurate composites. *Polymer Composites*, *36*(5), 892–896. http://doi.org/10.1002/pc.23008

Liang, F., Chen, J., Cheng, Y., Wang, L., Ma, D., Jing, X., & Wang, F. (2003). Synthesis, characterization, photoluminescent and electroluminescent properties of new conjugated 2,2′-(arylenedivinylene)bis-8-substituted quinolines. *J. Mater. Chem*, *13*(6), 1392–1399. http://doi.org/10.1039/B210408C

Limmer, S. j., & Cao, G. (2003). Sol–gel electrophoretic deposition for the growth of oxide nanorods. *Advanced Materials*, *15*(5), 427–431. http://doi.org/10.1002/adma.200390099

Liu, Y., Ata, M. S., Shi, K., Zhu, G. -z., Botton, G. A., & Zhitomirsky, I. (2014). Surface modification and cathodic electrophoretic deposition of ceramic materials and composites using celestine blue dye. *RSC Advances*, *4*(56), 29652–29659. http://doi.org/10.1039/C4RA03938F

Lu, S. Y., & Hamerton, I. (2002). Recent developments in the chemistry of halogen-free flame retardant polymers. *Progress in Polymer Science (Oxford)*, *27*(8), 1661–1712. http://doi.org/10.1016/S0079-6700(02)00018-7

Mallah, M. H., Maragheh, M. G., Badiei, A., & Sbo, R. H. (2010). Novel functionalized mesopore of SBA-15 as prospective sorbent for praseodymium and lutetium. *Journal of Radioanalytical and Nuclear Chemistry*, *283*(3), 597–601. http://doi.org/10.1007/s10967-010-0452-5

Mercury, J. M. R., Pena, P., De Aza, A. H., Sheptyakov, D., & Turrillas, X. (2006). On the decomposition of synthetic gibbsite studied by neutron thermodiffractometry. *Journal of the American Ceramic Society*, *89*(12), 3728–3733. http://doi.org/10.1111/j.1551-2916.2006.01191.x

Morgan, A. B., & Wilkie, C. A. (2007). *Flame Retardant Polymer Nanocomposites*. Hoboken, NJ: John Wiley & Sons,Inc.

Morgan, A. B., & Wilkie, C. A. (2014). *Non-Halogenated Flame Retardant Handbook*. Hoboken, NJ: Scrivener Publishing LLC.

Morgan, A. B., & Worku, A. Z. (2015). Flame Retardants: Overview. *Kirk-Othmer Encyclopedia of Chemical Technology*, 1–28. http://doi.org/10.1002/0471238961.1522051807011414.a01.pub3

Pang, X., Casagrande, T., & Zhitomirsky, I. (2009). Electrophoretic deposition of hydroxyapatite–CaSiO3–chitosan composite coatings. *Journal of Colloid and Interface Science*, *330*(2), 323–329. http://doi.org/10.1016/j.jcis.2008.10.070

Peng, Z., & Liu, M. (2001). Preparation of dense platinum-yttria stabilized zirconia and yttria stabilized zirconia films on porous La0.9 Sr0.1 MnO3 (LSM) substrates. *Journal of the American Ceramic Society*, *88*(2), 283–288. http://doi.org/10.1111/j.1151-2916.2001.tb00651.x

Pitois, A., Abrahamsen, L. G., Ivanov, P. I., & Bryan, N. D. (2008). Humic acid sorption onto a quartz sand surface: A kinetic study and insight into fractionation. *Journal of Colloid and Interface Science*, *325*(1), 93–100. http://doi.org/10.1016/j.jcis.2008.05.031

Poonam, Khatkar, P. S., Kumar, R., Khatkar, A., & Taxak, V. B. (2015). Synthesis, characterization, enhanced photoluminescence and biological activity of Eu(III) complexes with organic ligands. *Ournal of Materials Science: Materials in Electronics*, *26*(9), 7086–7095. http://doi.org/10.1007/s10854-015-3330-7

Porter, D., Metcalfe, E., & Thomas, M. J. K. (2000). Nanocomposite fire retardants - a review. *Fire and Materials*, *24*(1), 45–52. http://doi.org/10.1002/(SICI)1099-1018(200001/02)24:1<45::AID-FAM719>3.0.CO;2-S

Pujari, S. P., Scheres, L., Marcelis, A. T. M., & Zuilhof, H. (2014). Covalent surface modification of oxide surfaces. *Angewandte Chemie - International Edition*, *53*(25), 6322–6356. http://doi.org/10.1002/anie.201306709

Roy, R., Middleswarth, E. T., & Hummel, A. F. (1948). Mineralogy and Thermal Behavior of Phosphates; 1. Magnesium Pyrophosphate. *American Mineralogist*, *33*(7-8), 458–471.

Salamova, A., Hermanson, M. ., & Hites, R. A. (2014). Organophosphate and halogenated flame retardants in atmospheric particles from a European Arctic site. *Environ Sci Technol*, *48*(11), 6133–6140. http://doi.org/10.1021/es500911d

Saroj, Y., & Chhagan, L. (2013). Optimization of performance characteristics of a mixed dye based photogalvanic cell for efficient solar energy conversion and storage. *Energy Conversion and Management*, *66*, 271–276. http://doi.org/10.1016/j.enconman.2012.09.011

Sasaki, T., Kobayashi, T., Takagi, I., & Moriyama, H. (2008). Discrete Fragment Model for Complex Formation of Europium(III) with Humic Acid. *Journal of Nuclear Science and Technology*, *45*(8), 718–724. http://doi.org/10.1080/18811248.2008.9711472

Shaker, A. M., Komy, Z. R., Heggy, S. E. M., & El-Sayed, M. E. A. (2012). Kinetic Study for Adsorption Humic Acid on Soil Minerals. *J. Phys. Chem. A*, *116*(45), 10889–10896. http://doi.org/10.1021/jp3078826

Sridhar, T. M., & Mudali, U. K. (2003). Development of bioactive hydroxyapatite coatings on type 316L stainless steel by electrophoretic deposition for orthopaedic applications. *Transactions of the Indian Institute of Metals*, *56*(3), 221–230.

Stietiya, M. H., & Wang, J. J. (2014). Zinc and Cadmium Adsorption to Aluminum Oxide Nanoparticles Affected by Naturally Occurring Ligands. *Journal of Environmental Quality*, *43*(2), 498–506. http://doi.org/10.2134/jeq2013.07.0263

Stoll, S., & Buffle, J. (1995). Computer simulation of colloids and macromolecules aggregate formation. *Chimia Internation Journal for Chemistry*, *49*(8), 300–307.

Strekopytov, S., & Exley, C. (2006). Thermal analyses of aluminium hydroxide and hydroxyaluminosilicates, *25*(September 2005), 1707–1713. http://doi.org/10.1016/j.poly.2005.11.011

Sun, D. D., & Lee, P. F. (2012). TiO2 microsphere for the removal of humic acid from water: Complex surface adsorption mechanisms. *Separation and Purification Technology*, *91*(1), 30–37. http://doi.org/10.1016/j.seppur.2011.08.035

Sun, D. D., & Lee, P. F. (2012). TiO2 microsphere for the removal of humic acid from water: Complex surface adsorption mechanisms. *Separation and Purification Technology*, *91*(1), 30–37. http://doi.org/10.1016/j.seppur.2011.08.035

Sun, Y., Ata, M. S., & Zhitomirsky, I. (2012). Electrophoretic Deposition of TiO2 Nanoparticles Using Organic Dyes. *Journal of Colloid Interface Science*, *369*(1), 395–401. http://doi.org/10.1016/j.jcis.2011.12.010

The Geneva Association Staff, I. (2014). Fire and Climate Risk. Retrieved January 1, 2016, from https://www.genevaassociation.org/media/874729/ga2014-wfs29.pdf

Tombácz, E., Tóth, I. Y., Nesztor, D., Illés, E., Hajdú, A., Szekeres, M., & Vékás, L. (2013). Adsorption of organic acids on magnetite nanoparticles, pH-dependent colloidal stability and salt tolerance. *Colloids and Surfaces A: Physicochemical and Engineering Aspects*, *435*(1), 91–96. http://doi.org/10.1016/j.colsurfa.2013.01.023

Troitzsch, J. H. (1997). Overview of Flame Retardants. *Chimica Oggi*, *16*(1), 18–24. Retrieved from www.aerofiltri.it/DC_pdf/AS_A_OoFR.pdf

Vermeer, A. W. P., Van Riemsdijk, W. H., & Koopal, L. K. (1998). Adsorption of Humic Acid to Mineral Particles. 1. Specific and Electrostatic Interactions. *Langmuir*, *14*(10), 2810–2819. http://doi.org/10.1021/la970624r

VERWEY, E. J. W. (1947). Theory of the stability of lyophobic colloids. *The Journal of Physical and Colloid Chemistry*. http://doi.org/10.1038/162315b0

Wan Ngah, W. S., & Musa, A. (1998). Adsorption of humic acid onto chitin and chitosan. *Journal of Applied Polymer Science*, *69*(12), 2305–2310. http://doi.org/10.1002/(SICI)1097-4628(19980919)69:12<2305::AID-APP1>3.0.CO;2-C

Wang, M., Liao, L., Zhang, X., & Li, Z. (2012). Adsorption of low concentration humic acid from water by palygorskite. *Applied Clay Science*, *67-68*(1), 164–168. http://doi.org/10.1016/j.clay.2011.09.012

Wang, Y. C., Leu, I. C., & Hon, M. H. (2004). Kinetics of Electrophoretic Deposition for

Nanocrystalline Zinc Oxide Coatings. *Journal of the American Ceramic Society*, *87*(1), 84–88. http://doi.org/10.1111/j.1551-2916.2004.00084.x

Wang, Y., & Zhitomirsky, I. (2012). Bio-inspired catechol chemistry for electrophoretic nanotechnology of oxide films. *Journal of Colloid and Interface Science*, *380*(1), 8–15. http://doi.org/10.1016/j.jcis.2012.04.077

Weil, E. D. (2011). Fire-Protective and Flame-Retardant Coatings - A State-of-the-Art Review. *Journal of Fire Sciences*, *29*(3), 259–296. http://doi.org/10.1177/0734904110395469

Weil, E. D., & Levchik, S. V. (2009). *Flame Retardants for Plastics and Textiles: Practical Applications*. Cincinnati,OH: Hanser Publishers.

Wilkie, C. A., & Morgan, A. B. (2010). *Fire Retardancy of Polymeric Materials* (2nd ed.). Boca Raton, FL: Taylor and Francis.

Wills, K. A., Mandujano-Ramírez, H. J., Merino, G., Mattia, D., Hewat, T., Robertson, N., … Cameron, P. J. (2013). Investigation of a copper(I) biquinoline complex for application in dye-sensitized solar cells. *RSC Advances*, *3*(45), 23361–23369. http://doi.org/10.1039/C3RA44936J

Wojtal, P., Chen, S., Shi, K., Mathews, R., & Zhitomirsky, I. (2015). Electrophoretic deposition of a memory-type flame retardant material. *Materials Letters*, *153*, 106–109. http://doi.org/10.1016/j.matlet.2015.04.037

Wojtal, P., Luo, D., Chen, S., & Zhitomirsky, I. (2015). Composite Polymer-Metal Hydroxide Coatings with Flame Retardant Properties. *Materials and Manufacturing Processes*, null–null. http://doi.org/10.1080/10426914.2015.1037909

Wu, Y., Yao, C., Hu, Y., Zhu, X., Qing, Y., & Wu, Q. (2014). Comparative performance of three magnesium compounds on thermal degradation behavior of red gum wood. *Materials*, *7*(2), 637–652. http://doi.org/10.3390/ma7020637

Xavier, M. G., Banda, S. F., & Chama, C. C. (2013). Characterisation of Kapiri Mposhi Aluminosilicate Minerals. *Oriental Journal of Chemistry*, *29*(4), 1695–1701. http://doi.org/dx.doi.org/10.13005/ojc/29046

Yang, L., Pang, X., Fox-Rabinovich, G., Veldhuis, S., & Zhitomirsky, I. (2012). Electrophoretic Deposition of Polymer and Composite Films. *Surface Engineering*, *28*(8), 585–589. http://doi.org/10.1179/1743294412Y.0000000040

Yang, S., Li, L., Pei, Z., Li, C., Shan, X., Wen, B., … Huang, R. (2014). Effects of humic acid on copper adsorption onto few-layer reduced graphene oxide and few-layer graphene oxide. *Carbon*, *75*(1), 227–235. http://doi.org/10.1016/j.carbon.2014.03.057

Yum, J., Seo, S.-Y., Lee, S., & Sung, Y.-E. (2003). Y[sub 3]Al[sub 5]O[sub 12]:Ce[sub 0.05] Phosphor Coatings on Gallium Nitride for White Light Emitting Diodes. *Journal of The Electrochemical Society*, *150*(2), H47. http://doi.org/10.1149/1.1535207

Yurdakal, S., & Yurdakul, M. (2007). Vibrational frequencies and structural determination of 2,2'-biquinoline. *Journal of Molecular Structure*, *834-836*(1), 555–560. http://doi.org/10.1016/j.molstruc.2006.11.070

Zhang, H. (2009). Textile flame retardant review. *Modern Applied Science*, *3*(2), 129–133.

Zhitomirsky, I. (2002). Cathodic electrodeposition of ceramic and organoceramic materials. Fundamental aspects. *Advances in Colloid and Interface Science*, *97*(1-3), 279–317. http://doi.org/10.1016/S0001-8686(01)00068-9

Zhitomirsky, I., & Gal-Or, L. (1997). Electrophoretic deposition of hydroxyapatite. *Journal of Materials Science. Materials in Medicine*, *8*(4), 213–219. http://doi.org/10.1023/A:1018587623231

Zhitomirsky, I., & Petric, A. (2000). Electrophoretic deposition of ceramic materials for fuel cell applications. *Journal of the European Ceramic Society*, *20*(12), 2055–2061. http://doi.org/10.1016/S0955-2219(00)00098-4

Zhitomirsky, I., & Petric, A. (2004). Electrophoretic deposition of electrolyte materials for solid oxide fuel cells. *Journal of Materials Science*, *39*(3), 825–831. http://doi.org/10.1023/B:JMSC.0000012910.70526.61